Subject Specific Models of the Hindfoot Reveal a Relationship between Morphology and Passive Mechanical Properties

A Thesis

Submitted to the Faculty

of

Drexel University

by

Jason Robert Toy

in partial fulfillment of the

requirements for the degree

of

Doctor of Philosophy

December 2009

Dedications

To my wife, Melissa, your steady support and encouragement made this dream of ours come true. To my daughters, Jocelyn and Faith, may my love of education be yours one day.

Acknowledgments

I would like to thank my parents, Herb and Carolyn, for helping me find my passion. I had no idea where to begin with higher education but I knew I wanted to be a draftsman. I thought I learned enough to get me started in high school, but you would not let me end my education there. I finally gave into your insisting. When I first started my college career at Gloucester County College, I had no clue how to begin. As embarrassing as this is to say, I am thankful that you, mom, went with me to register for my first semester. Once I was into my college career, it was working at the barrel yard rebuilding steel drum reconditioning machinery and fabricating decks and supports that sparked my interest in how all the things I was learning to draw worked. It was that day you, dad, dropped me off at Richmond Machine Company to hang out with the old school engineers and draftsmen. That was the day I knew I wanted to be a mechanical engineer. I can not thank you both enough for the encouragement and opportunities you have given me. Three degrees later, I think it is safe to say I know what I want to do when I grow up.

Ted and Stella Szymanski, my wife's parents, thank you for entertaining Melissa, Faith, and Jocelyn for the many years I was glued to my computer. The dinner leftovers are always still welcome, anytime, really! A special thanks to Stella for reviewing my dissertation.

Dr. Joseph F. Shelley, once I finally decided to study mechanical engineering, it was your skill as an engineer and teacher that inspired my interest in stress analysis. You showed a practical side of all topics taught in a classroom, a rare talent.

Bill McCabe, thank you for the opportunity to practice all that I have learned and enjoy. It is a rare occurrence that an employer takes the time to know his employees and provides them with the means for boundless growth.

Mike R. Spegel, whose knowledge of computers has simplified life. I am unable to put into words the computational pains that I have avoided because of your generosity and awe-inspiring eagerness to help.

Rick Bystricki, you've reminded me how fun life can be, and to let go of my professional and academic duties and just enjoy.

Dave and Jen Rosenthal, thank you for reviewing my dissertation and being there for me.

Dr. Sorin Siegler, your contagious passion has forever left its impression on me. It is a passion that extends beyond engineering to family values. You inspire me. Thank you for ALL you have taught me.

Dr. Carl Imhauser, thank you for the countless hours you spent with me and the hindfoot models, all while working on your doctorate. As a committee member, your advisement

went beyond detailed academia to sharing your experiences with the stressful situations I am sure all doctaoral candidates feel. Thank you for always making sure I stick in there.

Dr. Richard Brand, you have taught me to explore all possibilities of solving a problem. You have shown me many new aspects of science and research that I will spend the rest of my carrer trying to master. Thank you for opening the door and exposing me to a higher level.

Dr. Franco Capaldi, thank you for all of the insight you have given me. Your ability to reduce a complex problem to a solvable one is an amazing talent. Hopefully, some of that wore off on me.

Table of Contents

List of Tables

List of Figures

Abstract

Subject Specific Models of the Hindfoot Reveal a Relationship between Morphology and Passive Mechanical Properties

Jason Robert Toy

Sorin Siegler, Ph.D.

The morphology of the bones, articular surfaces, and ligaments, as well as the passive mechanical characteristics of the ankle complex were reported to vary greatly among individuals. The goal of this study was to test the hypothesis that the variations observed in the passive mechanical properties of the healthy and injured ankle complex are strongly influenced by morphological variations. To evaluate this hypothesis, six numerical models of the ankle joint complex were developed from morphological data obtained from magnetic resonance images of six cadaveric lower limbs, and from average reported data on the mechanical properties of ligaments and articular cartilage. The passive mechanical behavior of each model, under a variety of loading conditions, was found to closely match the experimental data obtained from each corresponding specimen. Since all models used identical material properties and were subjected to identical loads and boundary conditions, it was concluded that the observed variations in passive mechanical characteristics were due to variations in morphology, thus confirming the hypothesis. In addition, the average and large variations in passive mechanical behavior observed between the models were similar to those observed experimentally between cadaveric specimens. The results suggested that individualized subject specific treatment procedures for ankle complex disorders are potentially superior to a one size fits all approach.

Chapter 1: Introduction

The morphology of the bones, articulating surfaces and ligaments of the human ankle joint complex is reported to be highly variable. These morphological variations could be the main cause for the large variations observed in joint mechanics. They could influence the mechanical consequences of ligament injuries and may partially explain why some individuals are more predisposed to chronic ankle or subtalar instability than others. They may influence the outcome of surgeries such as joint fusion or joint replacement. Despite the potential importance of this morphology-passive mechanics relationship, a review of the literature indicates that it has not been previously studied either experimentally or through numerical models. Models that incorporate subject specific morphological data provide a convenient framework to explore this relationship since material properties, loading and boundary conditions can be kept identical between models thus isolating and identifying the contribution of morphology.

Main Goal

Develop a subject specific image based numerical model of the human hindfoot capable of capturing complex three dimensional mechanics that may be used to investigate a correlation between subject specific morphology and passive mechanical properties.

Hypothesis

Variations observed in the passive mechanical response of inversion range of motion and talar trochlear contact of the ankle complex are strongly influenced by morphological variations in bone geometry and ligament orientation.

Specific Aims

To achieve the main goal of this study, the following specific aims are described.

Aim #1 Develop a subject specific image based numerical model of the human hindfoot capable of capturing a variety of mechanical phenomenon, such as kinematics, load displacement characteristics, hysteresis, and load transmission through the joint including ligament recruitment and articular cartilage contact characteristics in response to externally applied loads.

Aim #2 Evaluate the model's ability to capture mechanical responses by comparing, on a one-to-one basis, multiple subject specific models to their own experimental data, and on an average basis, multiple subject specific models to independent experimental data.

Aim #3 Test the effects of morphology by observing variations in inversion range of motion and talar trochlear contact area and its location by a subject-to-subject comparison in the intact and injured lateral collateral ligament configurations. Individual models are prepared using identical material properties and subject to identical loads and boundary conditions. Thus,

the variable parameters between models are morphology, i.e., boney architecture, ligament insertion and orientation, and cartilage thickness.

Chapter 2: Background

Morphology

Morphology of the bones, articulating surfaces, and ligaments of the human ankle joint complex are reported to be highly variable. Morphological variations could be a main cause for large variations observed in joint mechanics and could influence the mechanical consequences of ligament injuries and surgical procedures such as joint fusion and joint replacement.

Osteology

The primary bones of the human hindfoot are distal tibia, distal fibula, talus, and calcaneus. Many authors [1-3] have described in detail the general shape and size of theses bones and articulating surfaces, all of which have reported significant variations of key features that could possibly affect passive mechanical properties.

Distal Tibia

The lower end of the tibia is formed by five surfaces: inferior, anterior, posterior, lateral, and medial with the latter prolonged distally by the medial malleolus [1] (Figure 1).

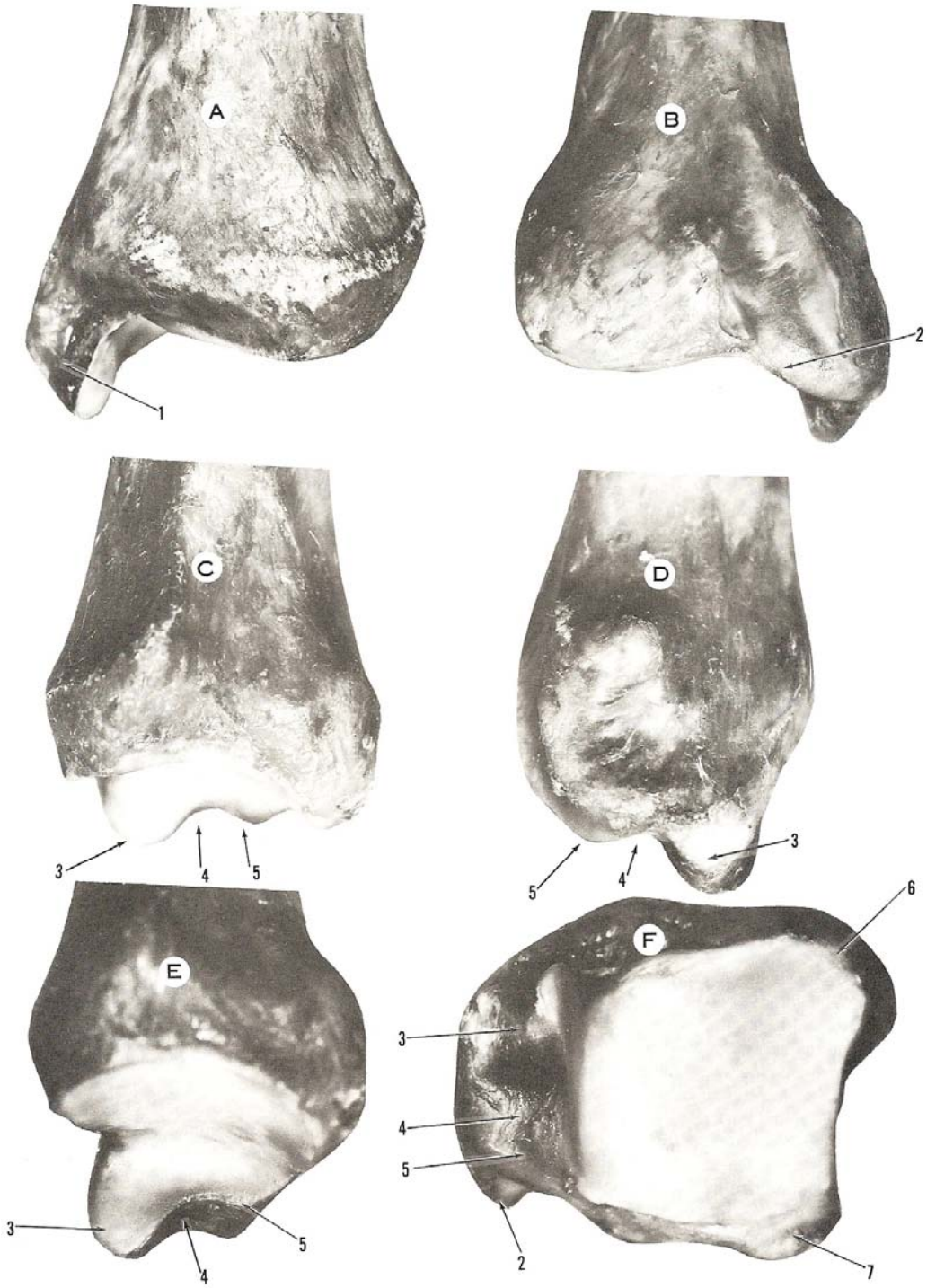

Figure 1. Tibia - General Features
(A) Anterior aspect of left distal tibia. (B) Posterior aspect of distal tibia. (C) Lateral aspect of distal tibia. (D) Medial aspect of distal tibia. (E) Lateral aspect of medial malleolus. (F) Inferior view of distal tibia. (1, medial malleolus; 2, sulcus for tibialis posterior tendon; 3, anterior colliculus; 4, intercolliculus groove; 5, posterior colliculus; 6, anterior tibial tubercle; 7, posterior tibial tubercle.) [Sarrafian, 1993]

The inferior surface articulates with the trochlear surface of the talus. The lateral border is larger than the medial and the anterior border is longer that the posterior. Geometrically, this surface is a section of a frustum of a cone with an average medial conical angle of 22° ± 4° [1]. This angle ranges from 0°, corresponding to a cylindrical surface, to 35° [1] (Figure 2).

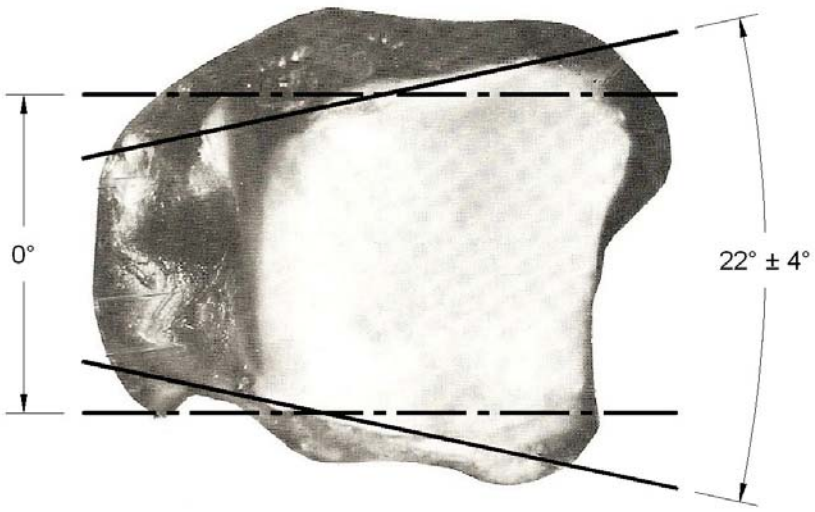

Figure 2. Tibial Plafond Conical Angle
[Sarrafian, 1993, modified]

The radius of this conical section is an average of 2 cm medial to lateral, and the corresponding articular arc measures 60°, on average [1] (Figure 3).

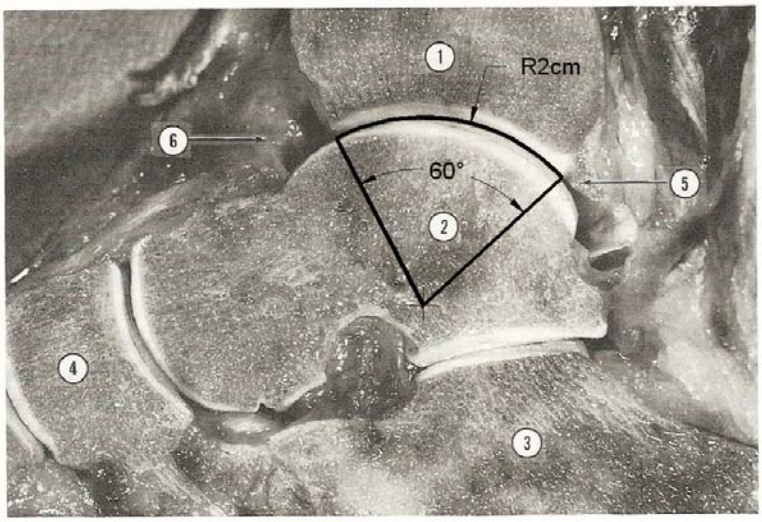

Figure 3. Tibia - Sagittal View through Plafond
1, tibia; 2, talus;, 3, calcaneus; 4, navicular [Sarrafian, 1993, modified]

Of the less frequent morphological variations, but worth noting, is the existence of a squatting articular facet located on the transverse ridge of the anterior border of the tibia [4, 5] (Figure 4). This additional facet, when present, may have up to three variations and is common among Indians and Australian Aborigines. When a tibial squatting surface is present, there is a mating articular facet located on the superior surface of the talar neck.

Figure 4. Tibia - Squatting Facet
[Singh, 1959, modified]

Talus

The talus is an intercalated bone located between the ankle bimalleolar fork and the tarsus. It is moored with strong ligaments but has no tendinous attachments [1]. The superior face forms the ankle joint, or tibiotalar joint, with the tibia plafond and lateral mallelous of the fibula. The inferior face forms the subtalar joint with the calcaneus. The talus is divided into three distinct regions: the body, the neck, and the head [1] (Figure 5).

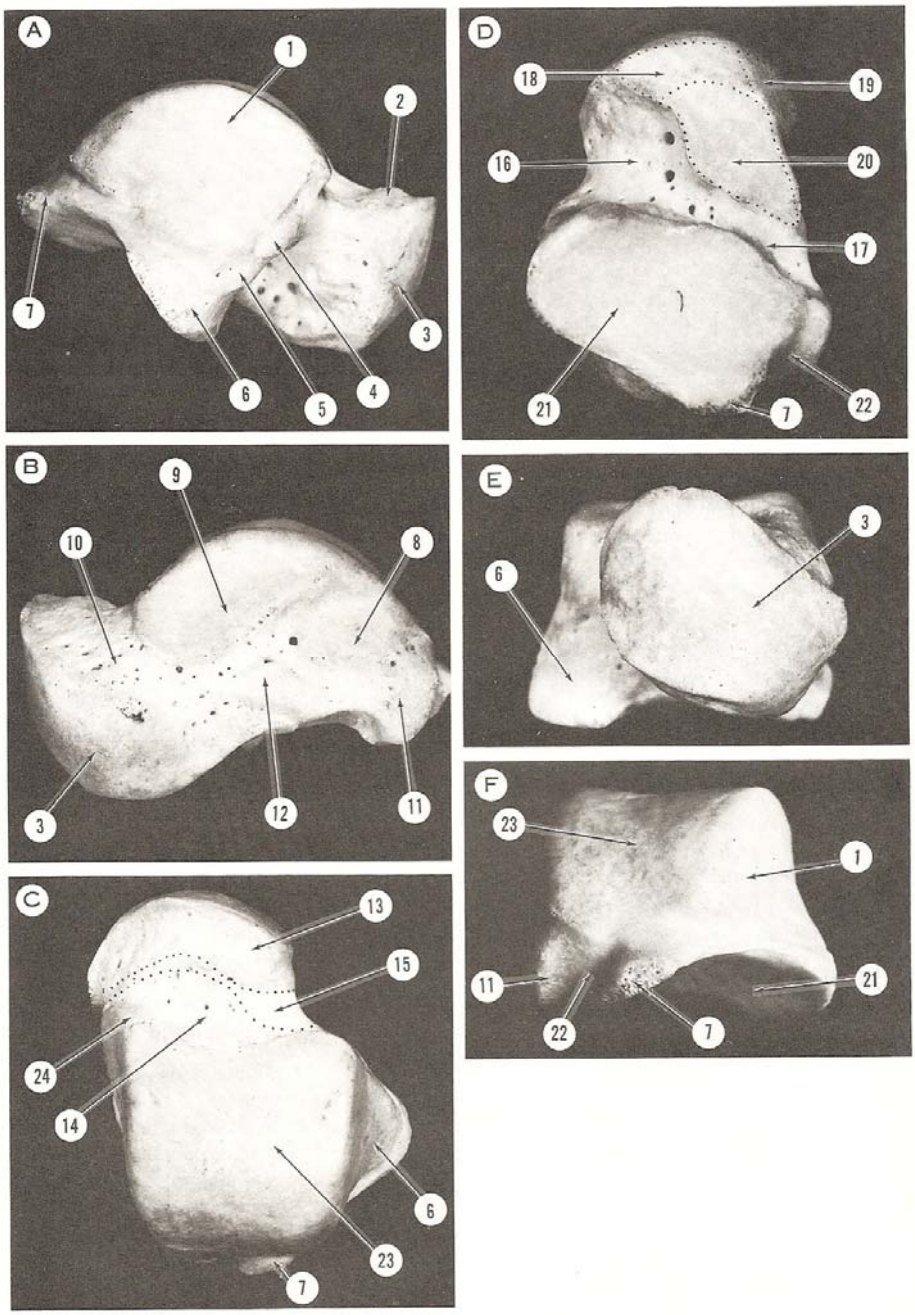

Figure 5. Talus - General Features

(A) Lateral aspect. (B) Medial aspect. (C) Superior aspect. (D) Inferior aspect. (E) Anterior aspect. (F) Posterior aspect. (1, articular surface - facies malleolus lateralis; 2, cervical collar; 3, articular surface - facies articularis navicularis; 4, 5, tubercles for insertions of anterior talofibular ligaments; 6, lateral process; 7, posterolateral tubercle; 8, oval surface for insertion of talotibial component of deltoid ligament; 9, articular surface - facies malleolaris medialis; 10, talar neck; 11, posteromedial tubercle; 12, tubercle of insertion of deltoid ligament; 13, segment of talar neck located within talonavicular joint; 14, segment of talar neck located within talotibial joint; 15, extra-articular segment of talar neck where a bursa may be found against which glides medial root of inferior extensor retinaculum; 16, sinus tarsi; 17, canalis tarsi; 18, anterior calcaneal articular surface of the talar head; 19, articular segment of talar head corresponding to superomedial and inferior calcaneonavicular ligaments; 20, middle calcaneal articular surface of talar neck; 21, posterior calcaneal articular surface of the talar body; 22, canal of the flexor hallucis longus tendon; 23, trochlear surface; 24, anteromedial extension of trochlear.) [Sarrafian, 1993]

The length and width of the bone measured on 100 dry tali. The average length (L) is 48 mm with a minimum of 40 mm and a maximum of 60 mm. The average width (W) is 37 mm with a minimum of 30 mm and a maximum 45 mm [1] (Figure 6).

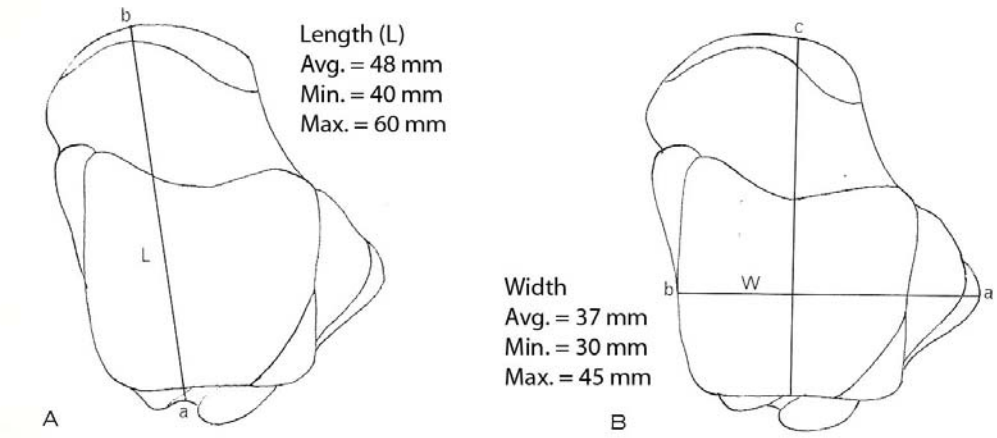

Figure 6. Talus - Length and Width Measurement
[Sarrafian, 1993, modified]

From an analytical approach, the length of the principal axes, which roughly coincide with the length and width measurements (Figure 6), are 53.74 ± 3.95 mm and 35.86 ± 3.30 mm, respectively [6]. This study measured morphological properties with the use of a computer aided three dimensional stress magnetic resonance image technique [7].

The morphology of the trochlear surface suggests that it is a frustum of a cone whose apex is directed medially and whose apical angle varies considerably from individual to individual, 24° ± 6° with a range of 0°, representing a cylinder, to 38° [2] (Figure 7). The apical angle of the talar trochlear surface is consistent with the tibial plafond, indicating congruent articular surfaces (Figure 2).

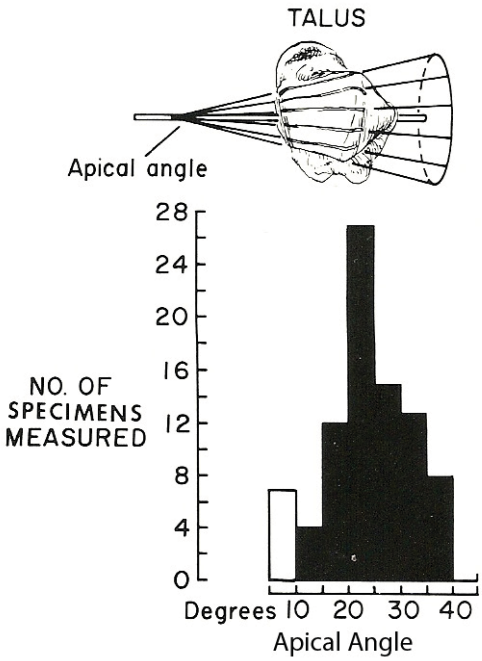

Figure 7. Talus - Trochlear Surface Apical Angle Variation
[Inman, 1991]

In the sagittal plane, the neck is deviated downward relative to the talar body and makes an angle of inclination that varies from subject to subject [1] (Figure 8).

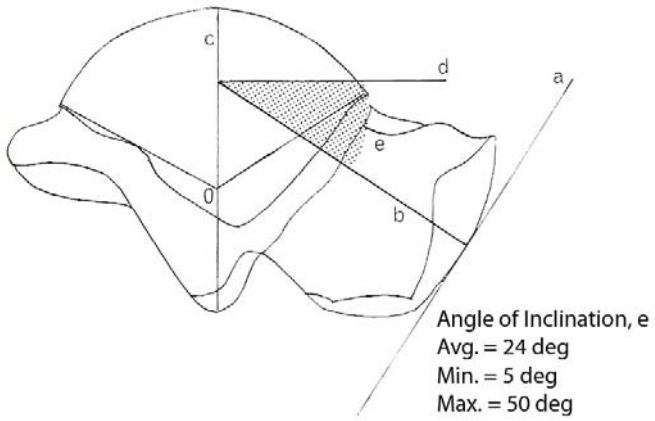

Figure 8. Talus - Inclination Angle of Talar Neck Relative to the Body
(e) The angle of the talar neck relative to the body. The center O of the lateral trochlear arc is determined. The arc is bisected by the radius OC. A tangent (a) is drawn at the apex of the navicular articular surface. A perpendicular line (b) is drawn at the tangential point. The line (b) gives the direction of the talar neck and intersects the radius OC of the talar trochlear arc. At this point of intersection a perpendicular line (d) is traced, determining the inclination angle (e). [Sarrafian, 1993, modified]

The inferior surface of the talus mates with the superior surface of the calcaneus. The inferior posterior articular facet, conforming to the posterior articular facet of the calcaneus, is a cylindrical shape and oriented from the anterior border of the trochlear surface (Figure 9).

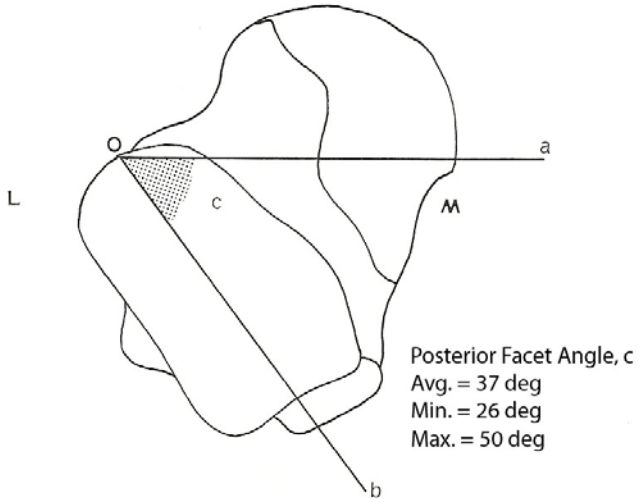

Figure 9. Talus - Inferior Posterior Articular Facet Orientation
Angle (c) formed by the long axis (ob) of the posterior calcaneal surface with a line (oa) parallel to the anterior trochlear border (line (oa) is projected from the superior surface). (L, lateral; M, medial). [Sarrafian, 1993, modified]

The inferior surface of the talus generally has three articular facets: anterior, medial, and posterior. However, many variations of the articular facets have been observed (Figure 10).

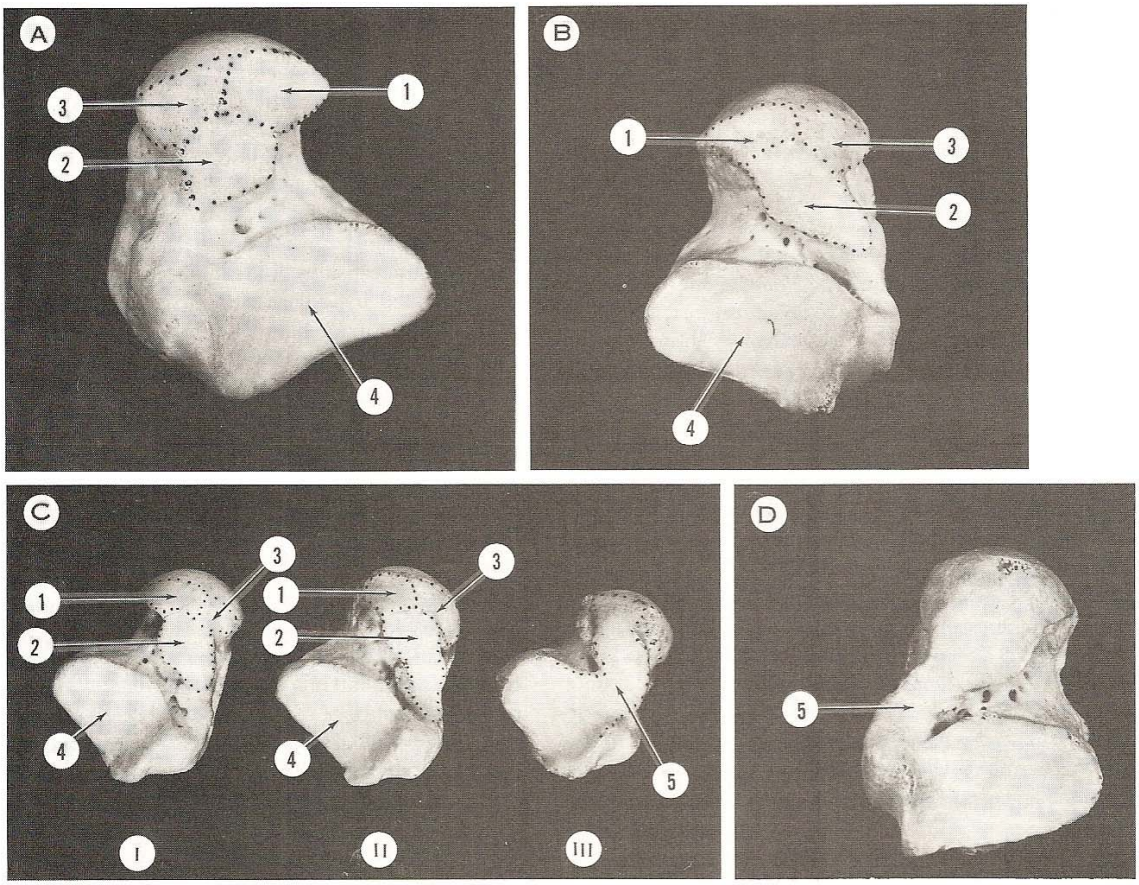

Figure 10. Talus - Variations of the Inferior Articular Surfaces
(A) Common configuration of the articular surfaces. (B) Posterior extension of the middle calcaneal surface. (C) (I) Moderate posterior extension of middle calcaneal surface. (II) Marked posterior extension of middle calcaneal surface. (III) Fusion (5) of all articular surfaces, obliterating the tarsal canal and a segment of the sinus tarsi. (D) Fusion (5) of the middle and posterior calcaneal surfaces on the medial aspect of the tarsal canal, which is still maintained. (1, anterior calcaneal articular surface of the talar head; 2, middle calcaneal articular surface of talar neck; 3, articular segment of talar head corresponding to superomedial and inferior calcaneonavicular ligament; 4, posterior calcaneal articular surface of talar body.) [Sarrafian, 1993]

Calcaneus

The calcaneus is the largest bone of the foot [1] (Figure 11). With respect to the hindfoot, it is attached to the talus, tibia, and fibula with ligaments. Its position is further maintained by tendon attachments and grooved tendon articulations.

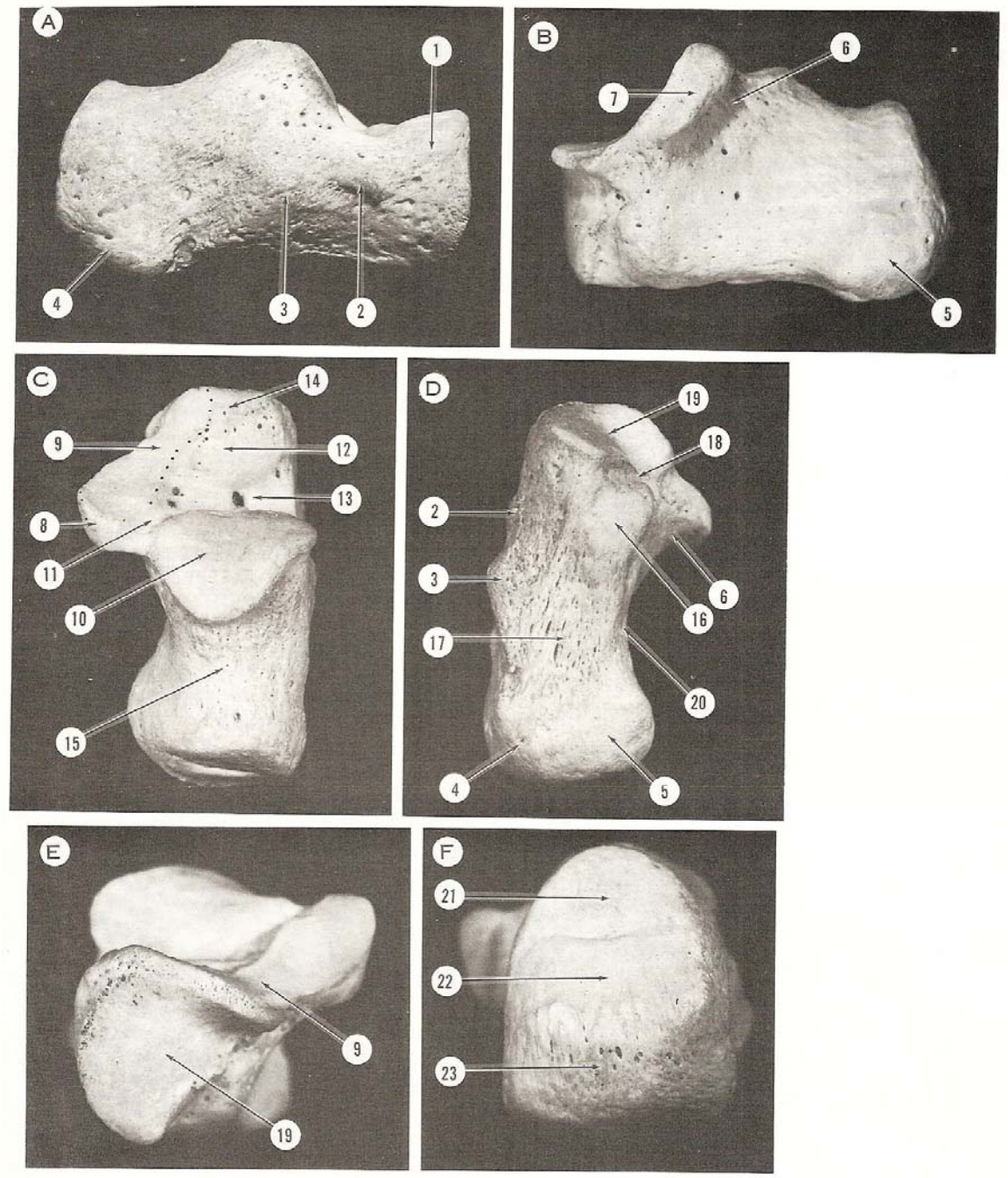

Figure 11. Calcaneus - General Features
(A) Lateral surface. (B) Medial Surface. (C) Superior surface. (D) Inferior surface. (E) Anterior surface. (F) Posterior surface. (1, great apophysis; 2, trochlear process; 3, eminentia retrotrochlearis; 4, lateral tuberosity; 5, medial tuberosity; 6, canal for flexor hallucis longus tendon; 7, medial surface of sustentaculum tali; 8, posterior border of sustentaculum tali; 9, fused anterior and middle talar articular surfaces; 10, posterior talar articular surface; 11, canalis tarsi; 12, sinus tarsi - bony eminence; 13, sinus tarsi - fossa calcanei; 14, sinus tarsi - insertion surface of bifurcate ligament; 15, posterior third of superior surface; 16, anterior tuberosity of inferior surface; 17, longitudinally striated inferior surface; 18, coronoid fossa; 19, cuboidal articular surface; 20, medial calcaneal canal; 21, upper third of posterior surface, corresponding to pre-Achilles bursa; 22, 23, middle and lower thirds of posterior surface, corresponding to insertion of Achilles tendon.) [Sarrafian, 1993]

The length, width, and height of the calcaneus vary (Figure 12). The average length (L) is 75 mm with a minimum of 48 mm and a maximum of 98 mm [1]. The average width (W) is 40 mm with a minimum of 26 mm and a maximum of 53 mm [1]. The average height (H), approximately 50% of the length, is 40 mm with a minimum of 33 mm and a maximum of 47 mm [1].

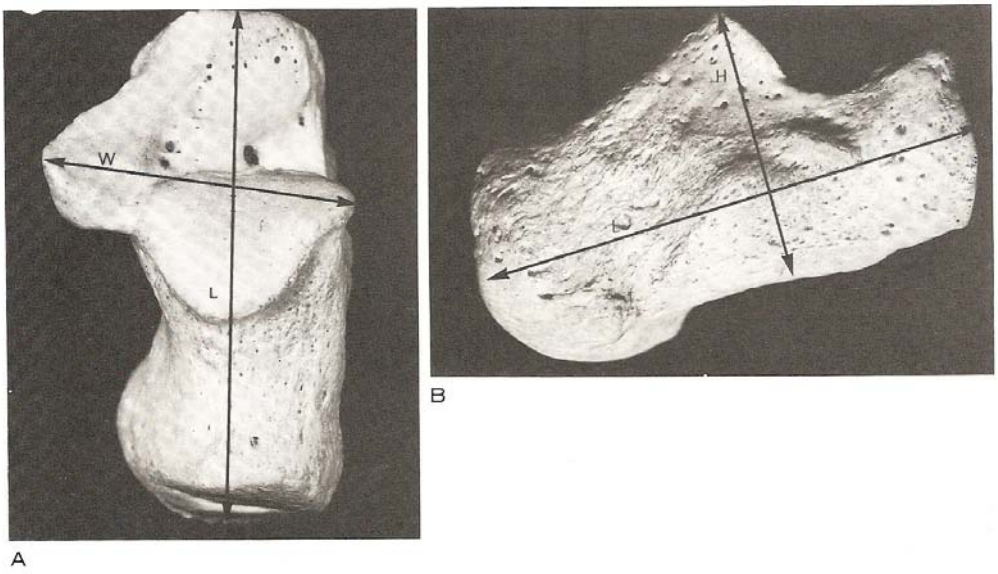

Figure 12. Calcaneus - Length and Width Measurement
(A) Superior View. (B) Lateral View. (L, length; W, width; H, height.) [Sarrafian, 1993, modified]

The length of the first geometric principal axis, the largest in magnitude roughly corresponding to the long axis, L (Figure 12), as measured by three dimensional reconstruction of magnetic resonance image data on 18 subjects is 79.48 ± 7.14 mm [6]. The second and third principal axis lengths relative to the width and height are 39.89 ± 4.44 mm and 37.54 ± 4.74 mm, respectively [6].

Its long axis is anteriorly pitched upward at an angle of inclination relative to the horizontal plane measuring 10° to 30° [2] (Figure 13).

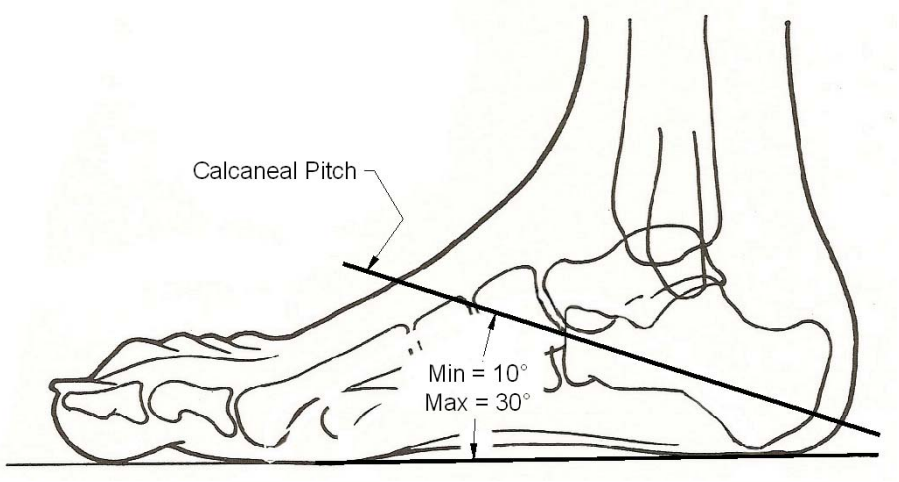

Figure 13. Calcaneus - Pitch Angle
[Kapandji, 1970, modified]

The calcaneus has several functional morphological features that vary from subject to subject such as: configuration of the anterior, middle, and posterior articulating facets, inclination of the posterior articular surface, and inclination and size of the sustentaculum tali.

The calcaneus may possess three distinct articular facets, anterior, middle, and posterior, or these facets may blend together (Figure 14). The anterior and middle articular surfaces of the calcaneus are located anterior-medially on the superior surface. They give support to the anterior and middle articular surfaces on the talar head and neck. The anterior surface is supported by the beak and the middle surface is supported by the sustentaculum tali [1]. The middle third of the calcaneus contains the posterior articulating surface, the largest of all on the calcaneus.

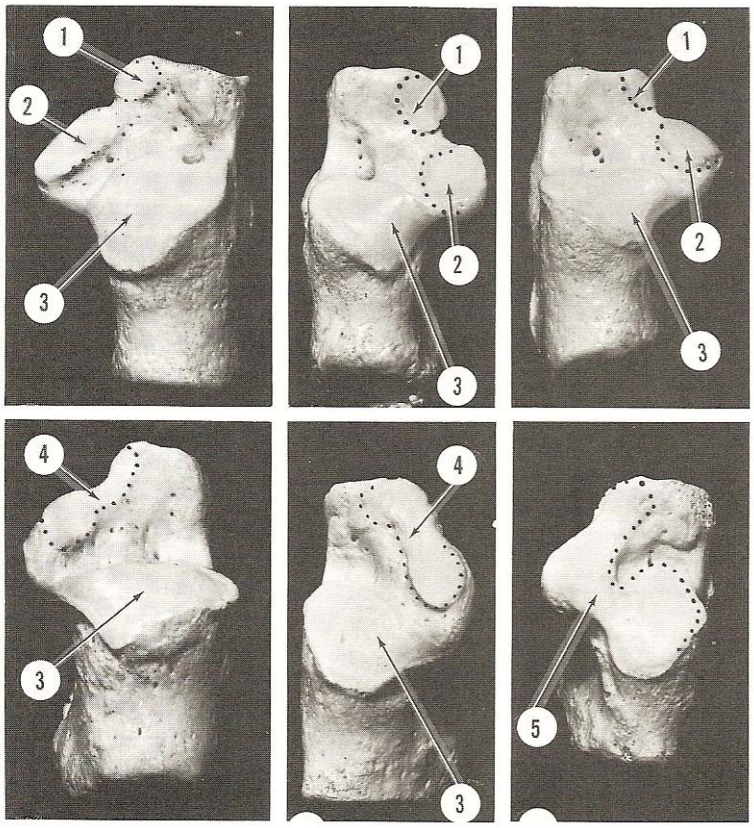

Figure 14. Calcaneus - Variations of the Superior Articular Surface
(1, anterior talar articular surface; 2, middle talar articular surface; 3, posterior talar articular surface; 4, fused anterior and middle talar articular surfaces; 5, fused anterior, middle, and posterior talar articular surfaces.) [Sarrafian, 1993]

Variations in the articular facets of the calcaneus have been classified into three types: A (all facets are distinct and separate), B (the anterior and middle facets are confluent), and C (all facets are united into a single surface) [8] (Figure 15).

		Occurrence (%)		
Author	**Number of Calcanei**	Type A	Type B	Type C
Laidlaw*†	750	32	69	
Bunning and Barnet‡	Veddah 10	0	60	40
	African 492	36	63	1
	British 194	67	33	0
	Indian 78	22	78	0
Present series	50	34	64	2
Padmanabhan	Indian 272	35	65	

* *Laidlaw reports complete absence of the anterior facet in 0.9%.*
† *Laidlaw PP: The os calcis, part II. J Anat Physiol 33:168, 1905*
‡ *Bunning PSC, Barnett CH: A comparison of adult and foetal talocalcaneal*

Figure 15. Calcaneus - Frequency of Articular Surface Variations
Present series [Sarrafian, 1993]

In addition to the three major articular facets of the calcaneus, up to three more accessory, or extension, facets may be present. The frequency of the presence of any of these accessory facets occurs less than 7% [9]. The accessory facet corresponding to the middle articular facet may form a union and obliterate the posterior end of the canalis tarsi [1, 9].

The posterior articulating facet makes a sharp change in orientation relative to the posterior segment, declining anteriorly and creating a step contour with the anterior process [1] (Figure 16).

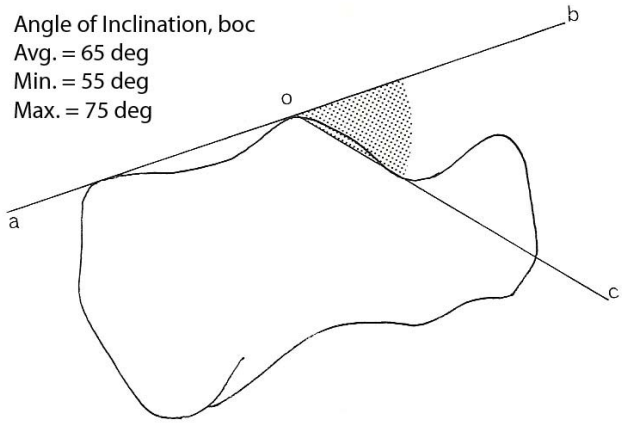

Figure 16. Calcaneus - Posterior Articular Surface Inclination
Angle of inclination (boc) of the posterior talar articular surface. [Sarrafian, 1993, modified]

The sustentaculum tali is a bracket-like projection, triangular with a posterior base and anterior apex. This surface projects anteromedial and is inclined downward and anteriorly at an average angle (boc) of 46° with a minimum of 30° and a maximum of 60° [1] (Figure 17).

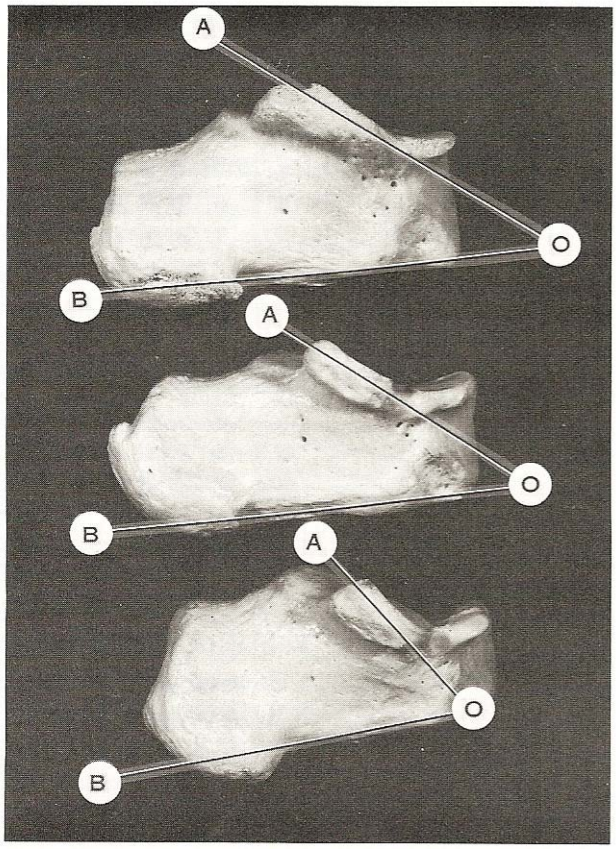

Figure 17. Calcaneus - Variable Inclination of the Sustentaculum Tali
Angle AOB [Sarrafian, 1993]

The width and length of the sustentaculum tali are variable. The width of the sustentaculum tali, as measured at the base, is on average 13 mm with a minimum of 8 mm and a maximum of 18 mm [1]. The ratio of the sustentacular width to the total width of the calcaneus is on average 0.33 with a minimum of 0.23 and a maximum of 0.47 [1]. These values may be correlated with the supportive function of the sustentaculum tali

relative to the talar head. An incompetent sustentaculum tali may fall into a group with minimum value [1].

The sustentaculum tali may also be classified by length as long or short [1]. A long sustentaculum is continuous through its medial border with the processus anterior, which is then associated with a fusion of the anterior and middle articular facets [1]. A short sustentaculum ends suddenly anteriorly, and a notch separates the two articular surfaces [1] (Figure 14 and Figure 17).

The lateral surface of the calcaneus gives insertion to the calcaneofibular ligament at a tubercle located approximately mid-length and mid-height (Figure 18). Cartilage covered gliding articulating facets may or may not be present in the sulci for the peroneus brevis and longus tendons [1].

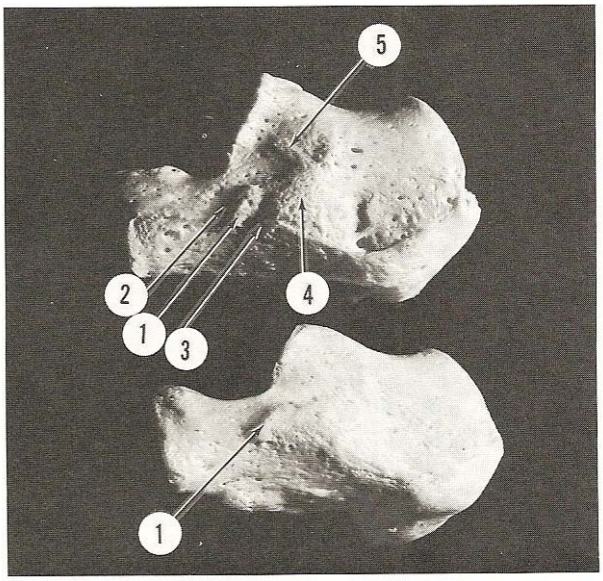

Figure 18. Calcaneus - Lateral Aspect
(1, trochlear process; 2, sulcus for peroneus brevis tendon; 3, sulcus for peroneus longus tendon; 4, eminentia retrotrochlearis; 5, tubercle for calcaneofibular ligament.) [Sarrafian, 1993]

Distal Fibula

The distal end of the fibula is articular on its medial side. It gives insertion to the anterior talofibular ligament on its anterior border and the calcaneofibular ligament on its inferior end (Figure 19).

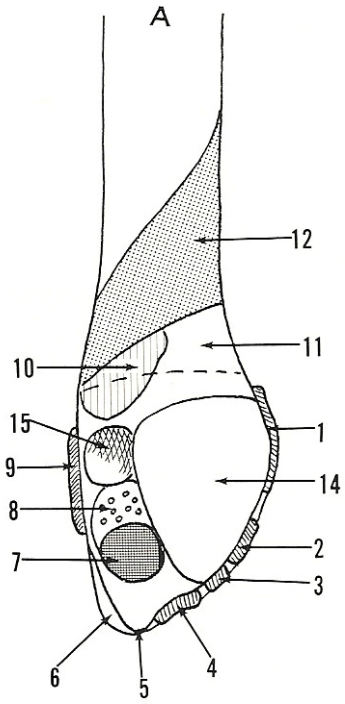

Figure 19. Fibula - General Features
Medial surface of distal fibula and lateral malleolus. (1, anterior tibiofibular ligament; 2, main component of anterior talofibular ligament; 3, secondary band of anterior talofibular ligament; 4, calcaneofibular ligament; 5, tip of lateral malleolus, free of insertion; 6, gliding surface of peronei tendons; 7, posterior talofibular ligament; 8, cribriform fossa; 9, superficial component of posterior tibiofibular ligament; 10, synovial fringe; 11, peroneal surface corresponding to tibioperoneal recess; 12, insertion of tibiofibular interosseous ligament; 14, articular surface for the lateral surface of the talus; 15, posterosuperior tuberosity.) [Sarrafian, 1993, modified]

The distal end of the fibula is pyramidal in shape and is known as the lateral malleolus. Together with the medial malleolus of the tibia, the tibiofibular mortise is formed, also known as the bimalleolar fork. It is a osseoligamentous retaining system to the talus and also provides stabilization of the calcaneus at the subtalar joint [1].

Syndesmology

The distal segment of the fibular shaft and the lateral malleolus are firmly attached to the distal tibia and form a moveable articulating system embracing the talar body [1]. Three ligaments uniting the distal fibular shaft and the lateral malleolus to the distal tibia are the anterior tibiofibular ligament, the posterior tibiofibular ligament, and the interosseous ligament [1]. This system of bones and ligaments is known as the distal tibiofibular complex.

The lateral mallelous of the fibula is connected to the talus by the anterior talofibular ligament and the posterior talofibular ligament. The calcaneofibular ligament spans from the fibula, over the talus, and connects to the calcaneus. These three ligaments comprise the lateral collateral ligament.

The medial malleolus of the tibia is connected to the talus and the calcaneus by the deltoid ligament. The deltoid ligament is divided into two layers, superficial and deep, each being formed by multiple fascicles [1]. A more descriptive breakdown of the deltoid ligament characterizes the posterior tibiotalar ligament and anterior tibiotalar ligament as connecting the medial malleolus to the talus, and the tibiospring ligament and the tibiocalcaneal ligament connecting the medial malleolus to the calcaneus [10].

The talus is firmly attached to the calcaneus by the cervical ligament and the interosseous talocalcaneal ligament. These are the primary ligaments of the subtalar joint.

All of the ligaments of the ankle joint complex, described above, vary in structure, insertion, orientation, and size from subject to subject. Of particular interest to this study are the anterior talofibular ligament and the calcaneofibular ligament of the lateral collateral ligament and their susceptibility to inversion injuries.

The most common musculoskeletal injury is an inversion sprain to the ankle [11, 12]. Approximately one million ankle injuries occur each year with a prevalence of 85 percent of them being sprains [13]. These sprains commonly injure the lateral ligaments, namely the anterior talofibular ligament and the calcaneofibular ligament. Injuries to these ligaments may lead to chronic lateral ankle pain, chronic instability, osteochondritis dissecans, and osteoarthritis [13-15].

Anterior Talofibular Ligament

The anterior talofibular ligament is flat and quadrilateral in shape (Figure 20). It is formed by two distinct bands with the upper being larger than the lower. A third band may occasionally be present. This ligament courses anteromedially from the anterior border of the lateral malleolus (Figure 19) and attaches to two tubercles on the anterior portion of the talar body (Figure 5).

Figure 20. Anterior Talofibular Ligament
(1, anterior talofibular ligament, main component; 2, anterior talofibular ligament, accessory component; 3, anterior tibiofibular ligament; 4, cervical ligament.) [Sarrafian, 1993]

Of the lateral collateral ligaments, the anterior talofibular ligament is the shortest, 1.781 ± 0.305 cm [16]. The cross sectional area of this ligament measures 0.129 ± 0.077 cm^2 [16]. Tensile tests of the lateral collateral ligaments of the ankle joint show this ligament to be the weakest with the lowest ultimate load, seeming to predispose this ligament to injury [16]. This may explain the frequency of injury of this ligament.

Calcaneofibular Ligament

The calcaneofibular ligament is a cordlike oval ligament 20 mm to 30 mm in length and 3 mm to 8 mm in diameter [1, 16] (Figure 21). It originates from the anteroinferior surface of the lateral malleolus (Figure 19) and roots itself on a tubercle on the lateral surface of the calcaneus (Figure 18).

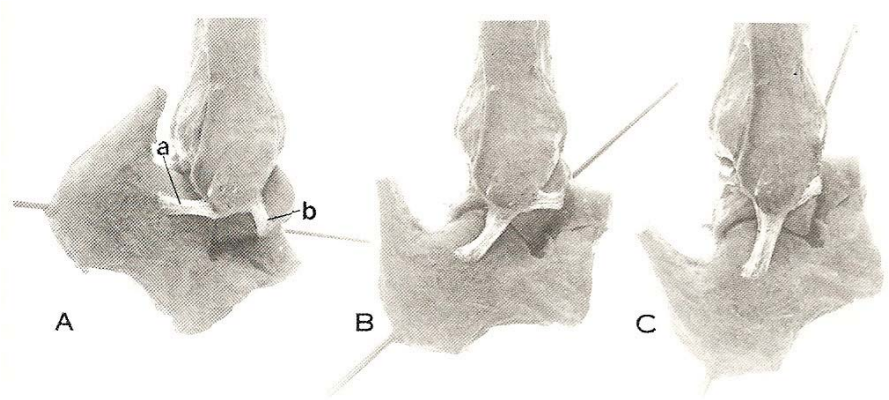

Figure 21. Calcaneofibular Ligament
(A) plantarflexion; (B) neutral; (C) dorsiflexion. (a, calcaneofibular ligament; b, anterior talofibular ligament.) [Inman, 1991]

The location of the calcaneal insertion is variable. In a study of 750 calcanei, the typical location in neutral position (Figure 21) occurs in 64.5%; anterior location, 25.5%; posterior location, 5.5%; downward location, 4.5% [9]. The variable insertions result in variable obliquity of the ligament orientation relative to the long axis of the fibula [1]. In a study based on 75 ankles, the orientation of this ligament relative to the long axis of the tibia varies from a common orientation (10° to 45°) to a vertical orientation (0°) and a horizontal orientation (80° to 90°). It may deviate from a cordlike structure as a fan shaped structure [17] (Figure 22).

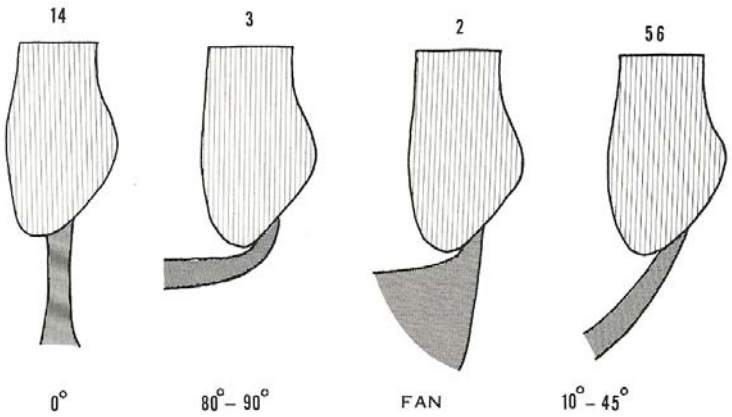

Figure 22. Calcaneofibular Ligament - Variable Orientation
[Sarrafian, 1993]

The calcaneofibular ligament is the strongest of the lateral collateral ligaments [16].

Cartilage Topology

Thickness

Cartilage of the ankle joint is thinner than its neighboring joints ranging from 1.06 mm to 1.63 mm on the tibia and 0.94 mm to 1.62 mm on the talus while the knee and hip are on average 2.16 mm and 1.74 mm, respectively [18].

In the joints of the ankle, articular cartilage thickness varies from one location to another on the same articular surface and from subject to subject. A detailed study of the ankle joint sampled thickness at various locations across the articulations on 14 subjects [19] (Figure 23)

.

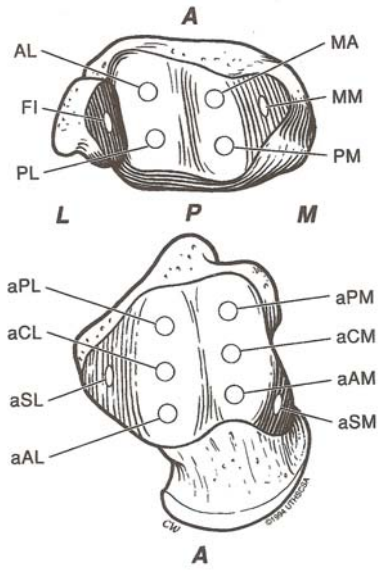

Figure 23. Cartilage Thickness - Sample Locations
On the top, the distal tibial surface shows the disection areas of the six specimens based on anatomical position. On the bottom, the talar dome surface shows the disection areas of the eight specimens based on anatomical positions. [Athanasiou, 1995]

Table 1. Thickness of Articular Cartilage of the Ankle Joint

Location (Figure 23)	**Avg. ± Std. Dev.** (mm)
Distal Tibia and Fibula	
(AL) anterolateral	1.30 ± 0.25
(MA) anteromedial	1.23 ± 0.27
(MM) medial malleolus	0.97 ± 0.16
(PM) posteromedial	1.20 ± 0.29
(PL) posterolateral	1.21 ± 0.25
(FI) fibula	0.95 ± 0.17
Superior Aspect of Talus	
(aAL) anterolateral	1.01 ± 0.31
(aCL) central-lateral	1.17 ± 0.27
(aSL) side-lateral	1.14 ± 0.23
(aPL) posterolateral	1.45 ± 0.42
(aPM) posteromedial	1.31 ± 0.26
(aCM) central-medial	1.31 ± 0.33
(aSM) side-medial	1.18 ± 0.24
(aAM) anteromedial	1.17 ± 0.34

[Athanasiou, 1995]

The tibial plafond appears to be relatively consistent in thickness throughout the surface. The articulating facets of the medial and lateral malleoli are the thinnest. The cartilage thickness of the trochlear surface of the talus seems to vary from thinnest to thickest in

the anterior to posterior direction. In all locations, notable standard deviations occur, indicating variations between subjects. This study also evaluated the material properties of the articular cartilage and found significant differences. Cartilage in the (MA) portion of the tibia had the largest aggregate modulus and the (aPL) and (aPM) portions of the talus were the softest [19]. Note that these softer regions correspond to the thickest sections of cartilage of the talus. Overall, tibial cartilage was slightly stiffer than talar cartilage [19]. Of further interest is that a significant difference in cartilage thickness was found between male (1.40 mm) versus female (1.02 mm) specimens [19].

In a study of the topographical distribution of articular cartilage thickness of the ankle joint, larger thickness variations compared to the previously discussed study [19] were found. This study utilized high resolution magnetic resonance imaging techniques to develop a three dimension reconstruction of the articular surfaces of the tibia, fibula, and trochlear talus [20] (Figure 24).

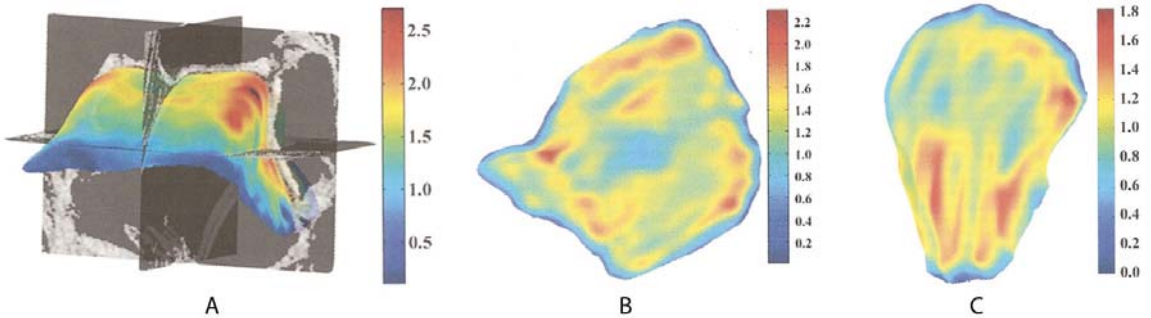

Figure 24. Cartilage Thickness - Spatial Distribution
(A) Talar Distribution. (B) Tibial Distribution. (C) Fibular Distribution. Three dimensional distribution map of cartilage thickness measured in mm. [Millington, 2006, modified]

The maximum cartilage thickness in this study was found to be 2.67 ± 0.25 mm occurring over the anterior-lateral and posterior-medial talar shoulders [20] (Figure 24A). These locations correspond to common occurrences of osteochondritis dissecans lesions [21].

Table 2. Thickness of Articular Cartilage of the Ankle Joint

Bone	**Avg ± Std. Dev.** (mm)	**Max. ± Std. Dev.** (mm)
Talus	1.34 ± 0.14	2.67 ± 0.25
Tibia	1.21 ± 0.14	2.44 ± 0.58
Fibula	0.91 ± 0.08	1.68 ± 0.18

[Millington, 2006]

The mean cartilage thickness of References [19] and [20] agree. However, the study of Reference [19] obtained samples from discrete locations, while the study of Reference [20] evaluated the spatial thickness distribution of the entire articulating surfaces.

Mechanics

The passive mechanical properties of the hindfoot are reported to be variable. These variations may be due to morphological variations of the bones, articulating surfaces, and ligaments.

Terminology of Motion

A discussion of mechanics of the motion of the ankle joint complex requires consistent terminology (Figure 25). The major motions about an anatomical joint coordinate system are rotations; plantarflexion / dorsiflexion, inversion / eversion, and internal / external rotation. The Y-axis is roughly parallel to the long axis of the tibia. The Z-axis is

aligned with the long axis of the foot. The X-axis passes through the tips of the lateral and medial malleoli and is known as the axis of rotation of the ankle [2].

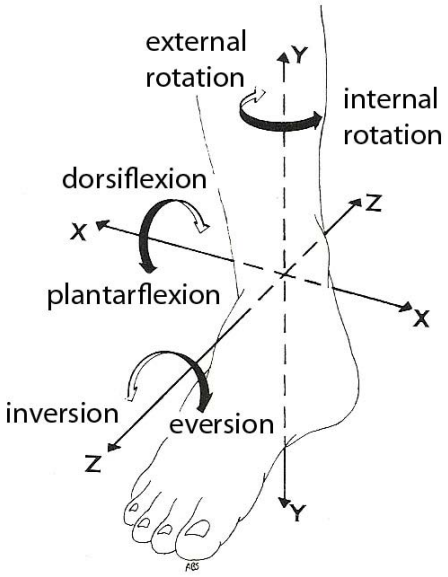

Figure 25. Mechanics - Terminology of Motion
[Sarrafian, 1993, modified]

Small translations along each axis may exist as each bone of the ankle joint possesses six degrees of freedom. One such translation with clinical relevance is along the Z-axis when manually diagnosing lateral collateral ligament injuries, namely of the anterior talofibular ligament. This is known as the anterior drawer test.

Plantarflexion / Dorsiflexion

Rotations about the X-axis (Figure 25 and Figure 26) are plantarflexion and dorsiflexion. Plantarflexion and dorsiflexion are the major components of the motion at the talocrural joint during gate [1]. Many authors cite variable ranges of motion for the ankle joint in the plantarflexion / dorsiflexion rotations (Table 3).

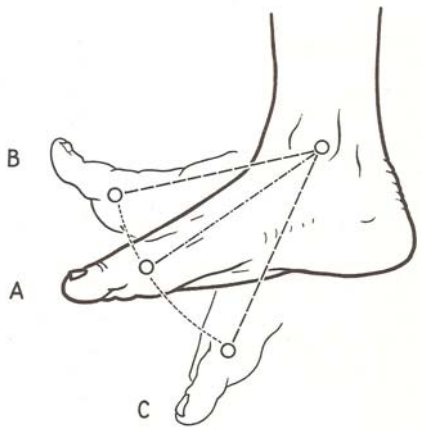

Figure 26. Range of Motion - Plantarflexion / Dorsiflexion
(A) Neutral. (B) Dorsiflexion. (C) Plantarflexion. [Kapandji, 1970]

Table 3. Range of Motion – Plantarflexion / Dorsiflexion

Range of Motion, (deg)		**Reference**
Plantarflexion	**Dorsiflexion**	
30 - 50	20 – 30	[22]
25 - 35	10 - 20	[23]
37.6 - 45.8	20.3 - 29.8	[24]
20 - 50	13 - 33	[25]

Motions in both directions were originally thought to occur about the same axis passing through the tips of the lateral and medial malleoli, or the axis of rotation of the ankle [2]. Since then, other investigators have demonstrated that the axis of rotation of the ankle is not fixed but has a variable axis that changes continuously throughout the range of movement [24, 26].

Inversion / Eversion

Rotations about the long axis of the foot, Z-axis (Figure 25 and Figure 27), are inversion and eversion. Motion in this direction is thought to be primarily contributed to by the subtalar joint [22]. The mechanism behind this thinking is the cylindrical shape of the posteroinferior articular surface of the talus and its congruent mate, the posterior articular facet of the calcaneus [22]. The long axis of the cylinder is oriented toward the long axis of the foot. Other contributions to this motion may come from the loose fit of the trochlear surface of the talus in the tibiofibular mortise. Many authors cite variations of motion in inversion and eversion (Table 4).

Figure 27. Range of Motion - Inversion / Eversion
(1) Neutral. (2) Inversion. (3) Eversion. [Kapandji, 1970]

Table 4. Range of Motion - Inversion / Eversion

Range of Motion, (deg)		**Reference**
Inversion	**Eversion**	
20	5	[22]
14.5 - 22	10 - 17	[24]
12.5 ± 5.8, in-vivo 12.6 ± 5.8, in-vitro	N/A	[27]
15 - 20	10 - 17	[28]
30	20	[1]
Total Range of Motion (Inversion + Eversion)		
10 - 65 (average 40° ± 7° standard deviation)		[2]

Internal / External Rotation

Rotations about the long axis of the tibia, Y-axis (Figure 25 and Figure 28), are internal and external rotation. These types of rotation usually do not occur by themselves but in combination with plantarflexion, dorsiflexion, inversion, and eversion. Many authors cite variations of motion in internal and external rotation (Table 5).

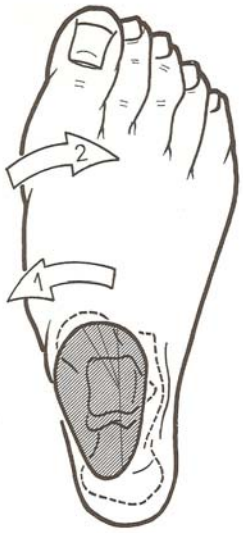

Figure 28. Range of Motion - Internal / External Rotation
(1) Internal Rotation. (2) External Rotation. [Kapandji, 1970]

Table 5. Range of Motion - Internal / External Rotation

Range of Motion, (deg)		**Reference**
Internal Rotation	**External Rotation**	
22 - 36	15.4 - 25.9	[24]
N/A	24	[29]
Total Range of Motion (Internal +External Rotation)		
35 - 45		[22]

Articular Joint Contact

Many studies have been performed to determine the contact area, location, and pressure of the joints of the ankle. It is difficult to ascertain from study to study what the contact area, location, or pressure may be due to many varying parameters such as: externally applied load, method of measurement, the presence of axial load, and boundary conditions. Instead, focus should be given to the variations in measurements over a single study.

A number of methods have been described which allow the determination of contact area, but most of them require that the joint be opened or invaded. These methods include the injection of colored materials into the joint space to tint the cartilage where it is not shielded by another apposed bit of cartilage, silicon casts of the joint space, which reveal the contact regions as openings in the model, and mechanical methods which rely on physical measurements of bone position from attached markers. The most commonly used method involves the insertion of pressure sensitive film into the joint, followed by application of a load, and measurement of the location and intensity of the colored regions which develop in the film. This method can give both the location of the contact and the distribution of pressure, but it must be done carefully to avoid altering the relationship between the bones and to ensure that the load has physiological meaning. These films are usually too stiff to conform to the small and relatively variable articular surface contours.

Ankle Joint Contact

The ankle joint articulation, or tibiotalar joint, is comprised of the tibial plafond (Figure 2) and the trochlear surface of the talus (Figure 5). The range of contact area reported within a single study may be influenced by morphological variations between subjects (Table 6). Variations in contact area between studies may be attributed to by the experimental setup and method of measurement.

Table 6. Ankle Joint Contact Area

n	**Method**	**Loading**	**Area**, (mm^2)	**Reference**
18	Pressure Sensitive Film	Neutral	327.4±31.9	[30]
3	Roentgen Stereophotogrammetric Analysis	Neutral	1.54–11.97	[31]
2	Tekscan Pressure Sensor	Neutral	295.1–493.6	[32]

n = number of subjects

Subtalar Joint Contact

The subtalar joint articulation is comprised of the multiple superior facets of the calcaneus, and all of its variations (Figure 14), and the multiple inferior facets of the talus, and all of its variations (Figure 10). The range of contact area reported within a single study may be influenced by morphological variations between subjects (Table 7). Variations in contact area between studies may be attributed to by the experimental setup and method of measurement.

Table 7. Subtalar Joint Contact Area

n	**Method**	**Loading**	**Area**, (mm^2)	**Reference**
9	Pressure Sensitive Film	Neutral	Anterior: 28±15 Posterior: 89±21	[33]
46	Injected Colored Dyes	Neutral	Middle: 43-71 Posterior: 380-559	[34]
9	Pressure Sensitive Film	Inversion	Total: 124-148	[33]
46	Injected Colored Dyes	Inversion	Anterior: 42-300 Middle: 132-217 Posterior: 406-598	[34]

n = number of subjects. For Reference [33] the anterior facet is defined as the combination of the anterior facet and middle facet.

Morphology-Mechanics Relationship

The morphology of the bones, articulating surfaces, and ligaments of the human ankle joint complex are reported to be variable [8, 35, 36]. These morphological variations could be a main cause for the variations observed in joint mechanics [24, 26]. The passive mechanical properties of the hindfoot may be influenced by the contour of the articulating surfaces, material properties of cartilage, the geometric and material properties of the ligaments, the retinacular system around the hindfoot, and the crossing and attached tendons.

Mechanical Analogs

Analytical models of the ankle joint have been proposed to describe mechanics that reproduce the plantarflexion / dorsiflexion motion during activities such as gate. Similar analytical analogs have been proposed to reproduce inversion / eversion rotations at the subtalar joint.

Ankle Joint

The simplest model of the ankle joint is a cylindrical surface acting about a fixed axis [22] (Figure 29). This model decouples morphology, with exception of the cylindrical radius of the tibial plafond (Figure 3), from the mechanics by limiting its motions to plantarflexion / dorsiflexion, thus not capturing kinematic coupling that has been observed at the ankle joint [24].

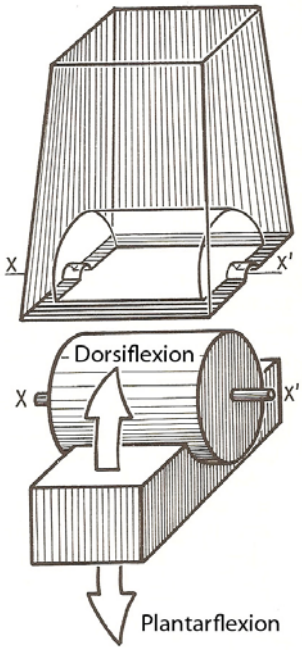

Figure 29. Ankle Joint - Cylindrical Analog
[Kapandji, 1970, modified]

Another view of the behavior of the ankle joint, incorporating morphological features, represents talar trochlear surface as a frustum of a cone (Figure 7). The conical trochlear surface is congruent with the conical tibial plafond and in the medial-lateral direction the talus is held snug within the medial and lateral malleoli in the neutral position [2]. During plantarflexion, the wedged, or narrowed, posterior end of the trochlear surface enters the ankle mortise and there is concern of a loosening of talar support because width of the posterior end of the trochlear surface is narrower than the width of the tibiofibular mortise [1]. However, during this motion, the fibula is known to tighten the ankle mortise and the talus also undergoes a coupled internal rotation, thus cocking the medial and lateral aspects of the talus against their tibial and fibular counterparts [2].

One method proposed that the ankle joint acts around a single axis that passes through the distal tips of the medial and lateral malleoli [2] (Figure 30). Even this simple analog begins to show variations among subjects.

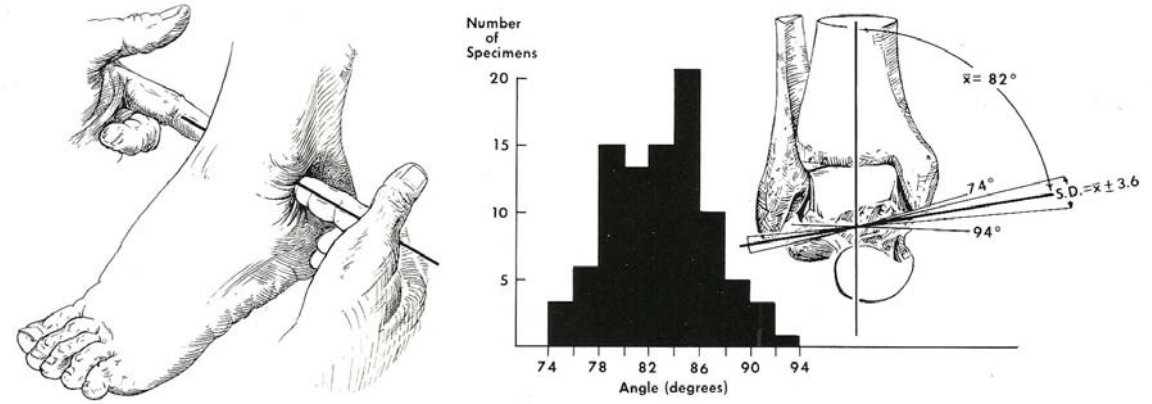

Figure 30. Ankle Joint - Single Axis of Motion
[Inman, 1991]

Later, motion of the ankle joint in plantarflexion / dorsiflexion was described to occur about two distinct axes [37, 38]. These studies indicate that motion about the ankle joint in dorsiflexion occurs about an axis inclined downward and laterally and in plantarflexion about an axis inclined downward and medially (Figure 31).

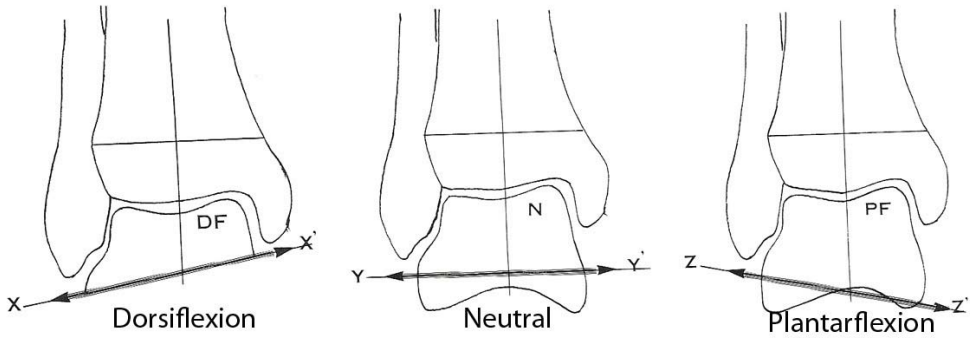

Figure 31. Ankle Joint - Multiple Axes of Motion
Ankle joint axis variation in dorsiflexion, neutral, and plantarflexion. [Sarrafian, 1993]

Subtalar Joint

Mechanical analogs have been used to describe motion about the subtalar joint. One study described an axis of the subtalar joint and found it to be highly variable among subjects [2]. This axis is oblique, oriented upward, anteriorly, and medially [1] (Figure 32). It penetrates the posterolateral corner of the calcaneus, passes perpendicular to the canalis tarsi, and pierces the superomedial aspect of the talar neck [1]. The orientation of the subtalar joint axis is in the transverse and sagittal planes.

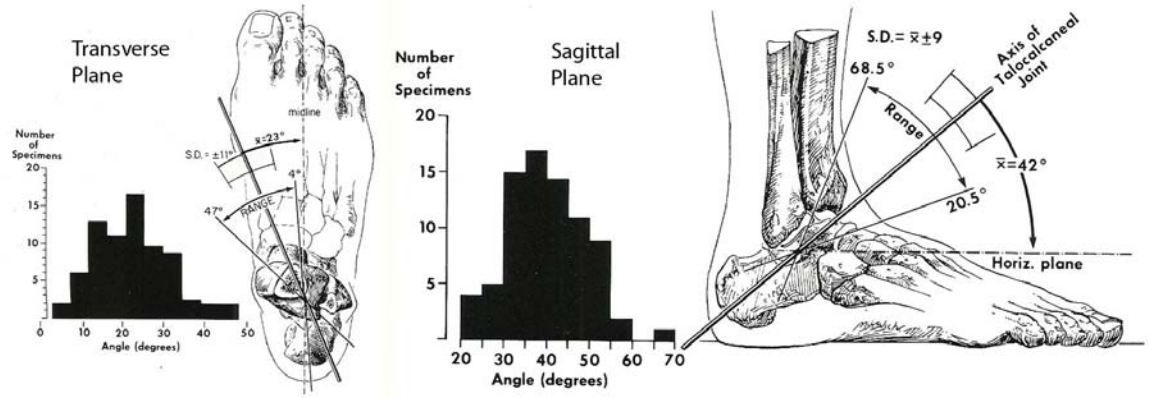

Figure 32. Subtalar Joint - Axis of Motion
[Inman, 1991]

Another study of motion around the subtalar axis recognized and measured a longitudinal displacement along the calcaneal axis and described the motion at the subtalar joint as that of a screw [2, 39] (Figure 33). During inversion motion of the subtalar joint, the talus rotates about the longitudinal axis of the calcaneus and translates anteriorly [39].

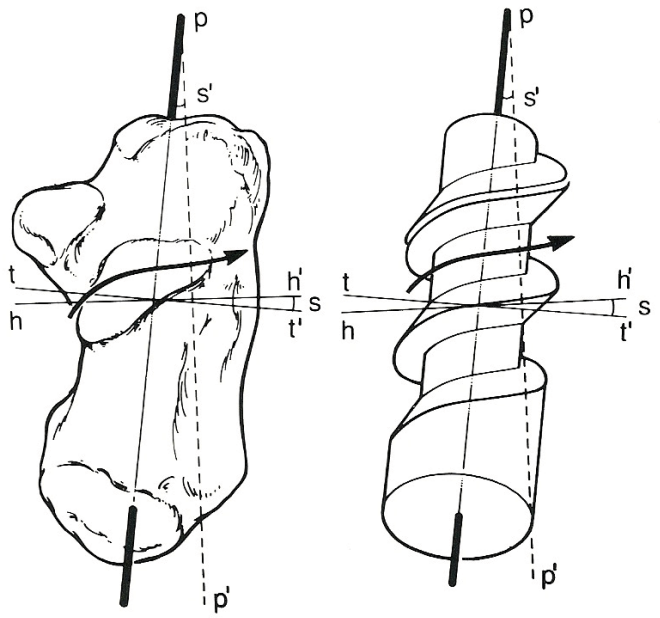

Figure 33. Subtalar Joint - Helical Screw Analog
Comparison of a right posterior facet with a right-handed screw. As the screw is turned in a clockwise direction, it advances. *hh'* is the horizontal plane in which motion is occurring. *tt'* is a plane perpendicular to the axis of the screw. *s* is the helix angle of the screw formed by the intersection of *hh'* and *tt'* and is equal to *s'*, which is obtained by dropping an perpendicular *pp'* from the axis. [Inman, 1991]

A following study of the screw behavior of the subtalar joint found only 58% of subjects exhibit some anterior forward motion of the talus when subject to inversion motion [2]. Twenty percent exhibit an initially backward motion followed by a forward motion, and another group, 20%, exhibited a random back and forth motion [2]. And finally, 3% showed pure rotary motion [2].

As each of these mechanical analogs increase in complexity, they rely on identification of morphological features to describe motion. Morphological features, that are known to be variable, may be the source of variability in subject to subject mechanical measurements.

Imaging Techniques

Mechanical analogs have been found to be obsolete in light of more sophisticated imaging techniques. Imaging techniques reveal the joints of the hindfoot to behave with all translational and rotational degrees of freedom. Studies of motion using these techniques reveal variations in mechanical response of the ankle joint complex, the ankle joint, and subtalar joint [6, 24, 27].

Functional Morphology

Variations of morphological features may influence their function in determination of resulting passive mechanical behavior. Functional morphology describes the relationship between variations of morphological features and variations of mechanical response.

Boney Architecture

At maximum dorsiflexion, the superior aspect of the talar neck may jam, or bear, against the anterior-inferior border of the tibia (Figure 34). This rigid limitation, or stop, is independent of surrounding soft tissues. Dorsiflexion may then be limited by the tibiotalar articular arc angle, radius, and the inclination angle of the talar neck (Figure 3 and Figure 8).

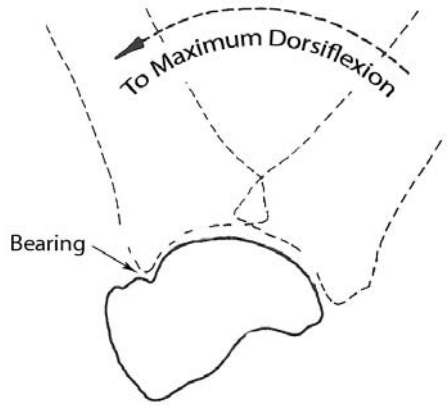

Figure 34. Maximum Dorsiflexion Bone-to-Bone Bearing
[Sarrafian, 1993, modified]

The degree of orientation of the posterior articular facet of the calcaneus (Figure 16) may affect plantarflexion range of motion. The posterior calcaneal surface inclination angle ranges from 55° to 75° relative to a line drawn along the superior surface of the calcaneal body. A larger inclination angle provides more plantarflexion motion [1].

The talar inferior posterior facet angle (Figure 9) may affect plantarflexion, dorsiflexion, inversion, and eversion motions. The facet angle ranges from 26° to 50° relative to the anterior trochlear border. A greater angle orients the surface in a longitudinal direction increasing dorsiflexion / plantarflexion, whereas a smaller angle orients the surface more transversely and increases inversion / eversion [1]. Applying the helical screw analog to inversion motion (Figure 33), a greater angle increases the screw pitch, thus increasing anterior translation of the talus.

Ligament Mechanics

The calcaneofibular ligament serves to stabilize the ankle and subtalar joints. The variability of the tension in the calcaneofibular ligament may be explained on the basis of the variability of ligament insertion [1]. The ligament may be oblique, horizontal, vertical, or fan shaped [17] (Figure 22 and Figure 35). This has a direct bearing on the tension developed by this ligament. When the calcaneofibular ligament is nearly horizontal, in eversion position of the heel, the distance between the origin and the insertion increase; the distance decreases in inversion [1]. The ligament is taut in eversion, and less tense in inversion [1]. When the ligament is vertical, the distance between the origin and the insertion increases in inversion and decreases in eversion [1]. When the ligament has an intermediary obliquity, the ligament tension remains unchanged throughout motion [1, 17].

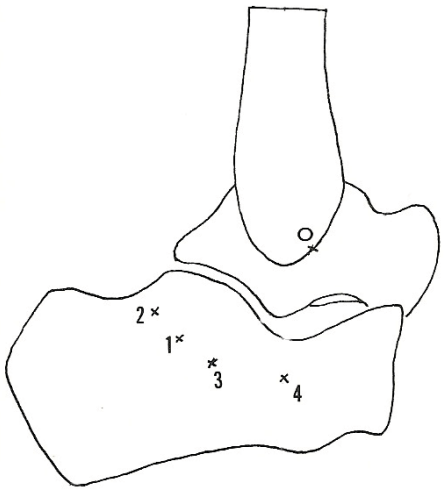

Figure 35. Calcaneofibular Ligament - Variable Insertion
O indicates the fibular origin of the calcaneofibular ligament and the numbers *1* to *4* the calcaneal insertion of the same ligament. The variable insertion determines the obliquity of the ligament; *1*, common insertion, oblique ligament; *2*, horizontal ligament; *3*, ligament located along the projection of the talocalcaneonavicular axis; *4*, vertical ligament. [Sarrafian, 1993, modified]

The calcaneofibular ligament alone resists 50% inversion loading under no axial load [40]. With coupled dorsiflexion, this ligament resists 65% of the applied load. Under inversion loads, the calcaneofibular ligament is strained to a range of 24% to 49% [41].

The anterior talofibular ligament limits the anterior shift and internal rotation of the talus. It is a major ligament determining stability in a load bearing plantarflexed position [1]. In the neutral position, the ligament is oriented horizontally [1] (Figure 21B). In dorsiflexion, the ligament is directed slightly upward [1] (Figure 21C). In marked plantarflexion, the ligament firmly braces the talar body as it stretches over the anterolateral corner of the trochlear surface, thus positioning it downward, medially, and anteriorly [1] (Figure 21A).

It has been suggested that a coupling effect exists between the anterior talofibular and calcaneofibular ligaments [2]. As the ankle joint passes from dorsiflexion to plantarflexion, the calcaneofibular ligament is less able to resist talar tilt, and reciprocally, the anterior talofibular ligament is more able to resist talar tilt [2].

Many of the above relationships drawn between morphology and mechanics are from observation with qualitative conclusions. To fully appreciate the complexity of the morphology-mechanics relationship, a three dimensional study that includes subject specific morphology is required.

Numerical Models of the Hindfoot

The objective of this study is to explore the relationship between subject specific morphology and passive mechanical properties using numerical modeling techniques. Numerical models permit control of parameters such as soft tissue properties, whereas in experiment, such parameters may not be manipulated. For instance, the morphology-mechanics relationship can be studied by creating patient specific models of the hindfoot while keeping all other parameters such as; ligament material properties, cartilage material properties, boundary conditions, and externally applied loads fixed between models. In such a model, the individual's boney architecture and ligament insertion may vary from subject to subject, isolating morphological effects.

Two fundamental strategies are used to develop previous models of the ankle joint complex. The first established mechanical analogues (e.g., ankle joint cylindrical analog, single axis of motion, helical screw analog, revolute joints, and four bar linkage) to approximate experimental observations [2, 39, 42, 43]. These models are based on average hindfoot characteristics such as fixed axes of rotation and ligament isometry in the sagittal plane [42]. They are not used to investigate the mechanical consequences of morphological variations between individuals.

The second modeling strategy is based on representation of the morphological and mechanical properties of the underlying anatomical structures. These models [44, 45] are limited to loading conditions that produce small displacements, such as axial loading of the foot [46], loading of the Achilles [47], or impulsive loading of the calcaneus [44].

They are used to explore only a small portion of the total three dimensional envelope of motion of the ankle complex. Models in this category are based on morphological data obtained from a single subject. They do not explore the effects of natural anatomical variations on the mechanical behavior of the joint.

A review of literature indicates that no previous experimental or modeling studies of the foot or ankle joint complex investigated the effects of morphological variations on the mechanical behavior. Previous modeling strategies fail to capture the three dimensional, coupled nature of hindfoot mechanics and are limited to evaluation of a narrow range of loading conditions that do not explore mechanical behavior in all three anatomical planes [42-44, 46, 47].

Chapter 3: Materials and Methods

This chapter describes the materials and methods used to develop subject specific numerical models of the human hindfoot capable of capturing passive mechanical behavior, evaluate the numerical models ability to predict passive mechanical properties, and test the effects of morphological features on passive mechanical properties.

Model Development

The model development begins with processing subject specific magnetic resonance image data to create morphologically unique hindfoot numerical models. Three dimensional rigid body dynamic and finite element models are used to study the relationship between morphology and passive mechanical properties.

Image Processing

Six models of the ankle joint complex are developed from magnetic resonance image data obtained with a 1.5 Tesla commercial General Electric Signa magnetic resonance image scanner from six non-pathological un-embalmed cadaveric legs (average age 71.5 years, 2 males and 4 females). The scanning protocol consists of a three dimensional Fast Gradient Echo pulse sequence with a TR/TE/flip angle of 11.5 ms/2.4 ms/60^0, a 512 x 256 in-plane acquisition matrix, a 731.2 receiver bandwidth, and a 180mm x 180mm field of view. Sixty 2.1 mm-thick contiguous sagittal slices were collected to cover the

foot from the medial to the lateral aspect. Consequently, the spatial resolution is 0.35mm x 0.7mm x 2.1mm [6, 27].

Each slice is processed, using 3DVIEWNIX [7], by a segmentation step to identify the bone boundary, an iso-shaping step to uniformly truncate long bones, a surface construction step to render the bone surface, and an estimation of morphological and architectural parameters step to obtain volume and inertial properties. The output produces point cloud data, a listing of three dimensional spatial coordinates of surface points for the generation of computerized three dimensional representations of the bones of the hindfoot for use in numerical simulations (Appendix A).

Six subjects are processed with all ligaments intact in the neutral and inversion positions [6]. Five subjects are processed with the anterior talofibular ligament and calcaneofibular ligament sectioned in the inversion position [6]. The sectioned anterior talofibular ligament and calcaneofibular ligament configuration represents an inversion injury. The neutral position is the basis for numerical model creation. The inversion position for the intact and injured ligament configurations are the basis for experimental data.

Computerized Bone Representations

Cartesian coordinates describing the points on the outer surface of each hindfoot bone, in the form of point cloud data, are used to identify coordinates to triangulate a polygon representation of the bone surfaces [48]. The triangulated point cloud data is processed, using Geomagic Studio [49], by a global noise reduction step to filter scanned artifacts, a

point wrapping step to fit the surface with polygons, a local surface smoothing step to remove rough contours, and a point decimation step to reduce model size (Appendix A).

The polygon representations are converted to file formats compatible with rigid body dynamic and finite element simulation software. The rigid body dynamic simulation software accepts geometry input as a stereolithograph (stl) format. The finite element software accepts geometry input as an initial graphics exchange specification (iges).

Simulation Models

The models for the hindfoot include a rigid body dynamic model and a finite element model. The rigid body dynamic model simulates motions of the ankle joint complex and computes passive mechanical properties of the hindfoot. The finite element model refines the description of articular contact by removing rigid body penetrations from the dynamic model through deformation of articular surfaces.

The rigid body dynamic model simulates plantarflexion / dorsiflexion, inversion / eversion, internal / external rotation, and anterior drawer. It captures range of motion, load-displacement characteristics, hysteresis, ligament force and strain, and bone position throughout the load duration.

The finite element model uses bone position data from the dynamic simulation to relocate the calcaneus and talus to a desired simulated position (Appendix B). Once positioned, the finite element representations of the bones are interpenetrated as a result of the rigid

body dynamic simulation. The description of contact area is refined by allowing the flexible bodies of the finite element model to deform, thus removing the rigid body penetration.

Rigid Body Dynamic Model

The rigid body dynamic model is constructed using the polygon representations of the bones of the hindfoot in the neutral position. Subject specific ligament insertions sites are obtained from the three dimensional surface reconstruction of the magnetic resonance image data. Ligament and cartilage material properties are obtained from literature [50, 51]. Subject specific average cartilage thickness is used to determine contact stiffness (Appendix A).

The rigid body dynamic simulation software, Adams [52], uses a Newton-Raphson predictor-corrector numerical algorithm to solve the dynamic equations based on the motion time history and current motion trajectory. The dynamic analysis involves developing [53] and then integrating [54-56] the non-linear ordinary differential equations of motion. The RAPID™ Interference Detection Algorithm [57] is used to determine contact between rigid bodies. Its algorithms compute efficient and exact interference detection between complex polygons undergoing rigid body motion [57].

Finite Element Model

The finite element model is developed using the computerized bone representations of the rigid body dynamic model in the neutral position. The polygon representation is further processed to offset the surface representing the subject specific cartilage layer. The material properties of cartilage are defined using a linear elastic constitutive law.

The cartilage layer is represented in the finite element model as a uniformly thick layer determined by the subject specific average measured at the tibiotalar joint. A linear elastic, homogeneous, isotropic constitutive law is used in the finite element model. The material properties required for this material model are: modulus of elasticity, 0.374 MPa [50], and Poisson's ratio, 0.05 [19]. These material properties are constant throughout all subjects.

The cartilage layer inner surface represents the interface between bone and cartilage. On this surface, the bones are constrained in space. The ratio of the modulus of elasticity of bone, 35.63 MPa [58], to that of cartilage, 0.374 MPa [50], is approximately 100:1. The stiffness of bone compared to cartilage is much greater, therefore, a rigid constraint on the interface surface is appropriate.

The uniformly thick cartilage layer is generated by operating on the original bone surface and the offset bone surface. Upon importing, the surfaces are converted to volumetric bodies. The volume shared by the original and offset bones is subtracted to form a continuous volumetric shell, representing a uniform cartilage thickness and adjacent bone surface (Figure 36).

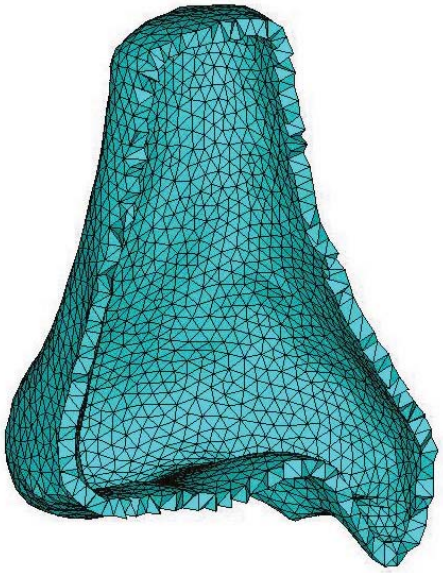

Figure 36. Finite Element Geometry - Cartilage Thickness Shell

The arrangement of polygons representing the original and offset surfaces is preserved to maintain continuity for uniform meshing. The inner and outer surface polygon vertices are connected with line geometry through the thickness of the cartilage layer. The surface discretization and internal line geometry are connected in a regular manner, therefore, regularly shaped tetrahedral element may be applied without loss of numerical accuracy due to shape errors [59].

The cartilage layer is meshed with three dimensional solid elements, or brick elements, degenerated to their tetrahedral form [59] to conform to the irregular articular surfaces (Figure 37 [59]). The element has three degrees of freedom at each node: translations in the nodal x, y, and z directions [59]. This is an isoparametric element with linear shape functions for the four node tetrahedral form (Figure 38 [59]).

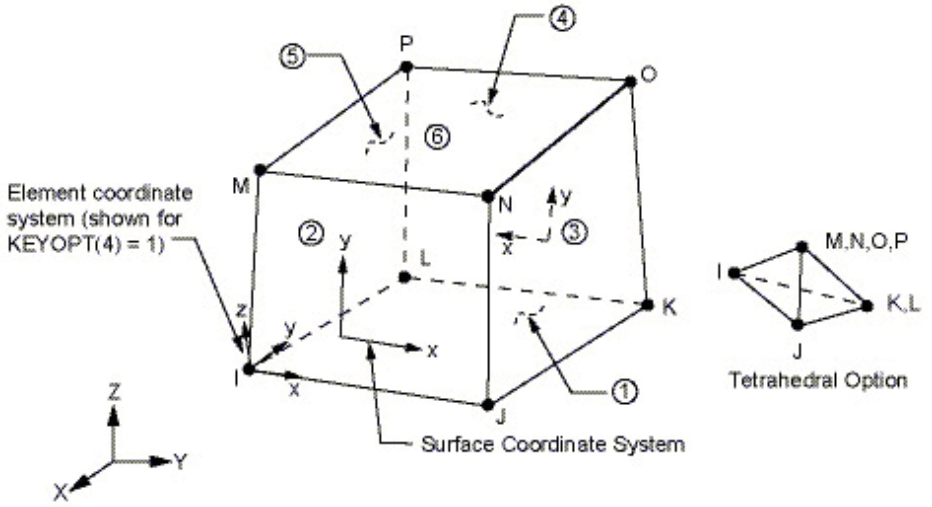

Figure 37. Three Dimensional Structural Solid Element

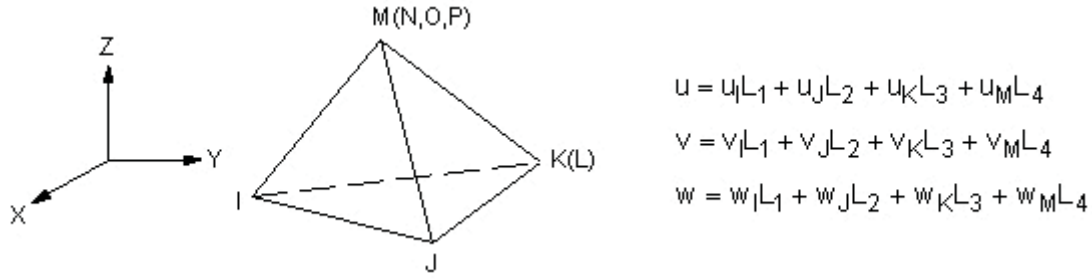

Figure 38. Three Dimensional Structural Solid Element - Shape Functions

The element stiffness matrix, K, determines the response of the local element degrees of freedom [60] (Equation 1).

$$K = \int_V B^T CB dV \qquad \textbf{Equation 1}$$

B is the strain-displacement transformation matrix, C is the material property matrix, and dV is the volume differential. The volume integration extends over the natural coordinate volume [60]. The material property matrix, C, can be reduced to two parameters, the modulus of elasticity, E, and Poisson's ratio, ν, for a isotropic, homogeneous, linear elastic constitutive law.

The surface-to-surface contact elements overlie the three dimensional solid structural elements like an infinitesimally thin membrane. Contact between the articular surfaces is detected by these elements and initial penetration of contacting bodies is removed using the Augmented Lagrangian Method. The Augmented Lagrangian Method is a combination of the Pure Penalty Method and the Lagrange Multiplier Method [59], requiring a contact stiffness and a penetration tolerance [59].

The penalty method of enforcing contact compatibility uses a contact spring to establish a relationship between two interacting surfaces [61]. The spring stiffness is called the penalty parameter or more commonly the contact stiffness. The spring is inactive when the surfaces are apart (open status), and becomes active when the surfaces begin to interpenetrate (closed status). The contact spring deflects an amount, Δ, such that equilibrium is satisfied: $F = k\Delta$, where, k, is the contact stiffness (Figure 39 [61]).

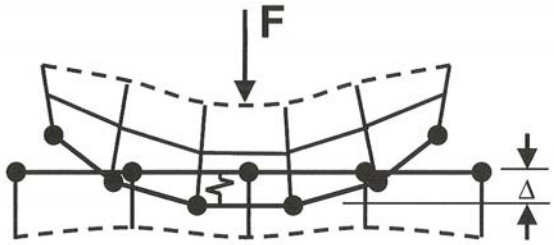

Figure 39. Contact Stiffness - Penalty Method

Δ represents the interpenetrating distance. Some amount of penetration is required mathematically to generate a contact force at the interface. This contact force is required to satisfy equilibrium conditions, thus Δ must be greater than zero for equilibrium. However, physical contacting bodies do not interpenetrate. Therefore, the goal is to minimize the amount of penetration that occurs at the contact interface. This implies that, ideally, the contact stiffness should have a very great value. However, too high of a value can lead to convergence difficulties. If the contact stiffness is too high, a slight penetration will generate an excessive contact force, potentially throwing the contacting surfaces apart in the next iteration of the nonlinear solution. With the Pure Penalty Method, using too great a contact stiffness usually leads to oscillating convergence, and often to outright divergence [61].

The contact stiffness is the most important parameter affecting both accuracy and convergence behavior [61]. The valve of the contact stiffness is often problem dependant. The contact stiffness is a function of a user defined contact stiffness factor, FKN, and the stiffness of the underlying solid element, $k_{underlying}$ (Equation 2).

$$k_{contact} = FKN \times k_{underlying} \qquad \textbf{Equation 2}$$

For bulky solids in contact, a value of $FKN = 1.0$ will use a contact stiffness value the same as the stiffness, in the normal direction, of the underlying solid element [61].

An alternative method to the Pure Penalty Method, the Lagrange Multiplier Method, adds an extra degree of freedom (contact pressure) to satisfy the impenetrability condition. Therefore, it does not require a contact stiffness term. Theoretically, this method offers the realistic impenetrable contact behavior. However, a host of numerical difficulties surround the implementation of this method such as: chattering problems, over constraint, and zero diagonal stiffness matrix terms [59].

The Augmented Lagrangian Method combines both the Penalty Method and Lagrange Multiplier Method to enforce contact compatibility [59, 61]. In the first series of equilibrium iterations of the nonlinear numerical solution, contact compatibility is determined based on the penalty stiffness [61]. Once equilibrium is achieved, the penetration tolerance is checked [61]. At this point, if necessary, the contact pressure is augmented and the iterations continue [61]. The penetration tolerance is described as a penetration distance or depth (Figure 40 [61]).

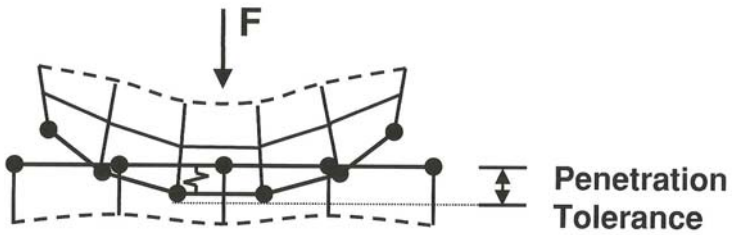

Figure 40. Contact Penetration Tolerance - Augmented Lagrangian Method

The penetration tolerance is determined by the depth of the underlying element (Figure 41 [59]) (Equation 3). *FTOLN* is a user defined penetration tolerance factor and *h* is the depth of the underlying element.

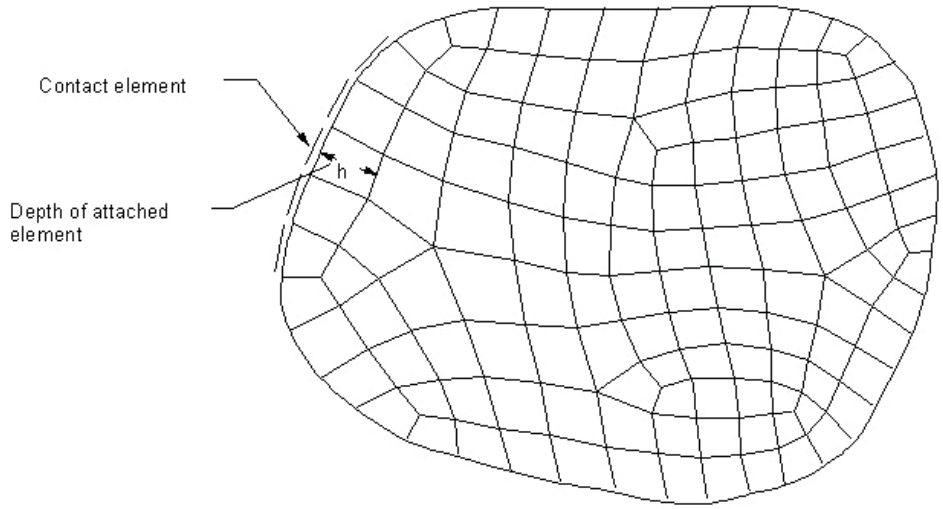

Figure 41. Contact Penetration Tolerance - Underlying Element Depth

$$Tolerance = FTOLN \times h \qquad \textbf{Equation 3}$$

As penetration tolerance is tightened, the accuracy may improve but at the expense of more difficult convergence. It is recommended to let the contact stiffness enforce compatibility and fine-tune the penetration with a reasonable value of *FTOLN* [61].

The Small Static Displacement Solution Controls setting in the finite element software is used to invoke a linear static analysis. For the nonlinearity introduced by contact, the Automatic Time Stepping was left at the default, Program Chosen. The Sparse Matrix Direct Solver was used as the equation solver.

Model Evaluation

The patient-specific image-based numerical model's ability to capture mechanical responses is evaluated by comparing, on a one-to-one basis, multiple subject specific models to their own experimental data and on an average basis to independent experimental data. The materials and methods used to evaluate subject specific models for their ability to capture passive mechanical properties of the ankle joint complex are described.

Experimental Data

Evaluation of the models is based on a one-to-one comparison (n=6) and a group mean comparison (n=15) to evaluate average model behavior. This second group excludes the six specimens used to create the models. Externally applied loads and boundary conditions applied to the model mimic the experiment.

One-to-One Model-to-Experiment Comparison

For the one-to-one comparison, the experiments consisted of loading the ankle joint complex in inversion simulating clinical tests for evaluating integrity of the anterior talofibular ligament and calcaneofibular ligament [6, 62]. First, each specimen is positioned in neutral in a magnetic resonance compatible loading device [27] with the tibia and fibula fixed and the calcaneus constrained to move only in the direction of the applied loads, then scanned. Next, an inversion moment increasing from zero to $3400 Nmm$ is slowly applied over a three second duration, the device is locked in the

maximally loaded position, and the loaded specimen is rescanned. The procedure is repeated with the anterior talofibular ligament and calcaneofibular ligament sectioned.

The rotations and translations of the calcaneus from neutral to each maximally loaded configuration are computed from the magnetic resonance image data [27]. A finite rotation about an axis is calculated using the inertial axis coordinate system of the calcaneus expressed relative to the tibia in the neutral and loaded configurations [63, 64].

The contact area and its location on the talar trochlear surface is measured by identifying boney regions falling within a specified distance between adjacent articulating surfaces. The three dimensional computerized bone representations of the hindfoot are assembled, using Geomagic Qualify [65] in the inversion loaded position. The three dimensional computerized bone representations of the experimental data do not undergo a local smoothing operation to prevent artificial manipulation of the bone and articulating surfaces, leaving a staircase structure (Appendix A). Each bone of the ankle joint is assembled relative to the global coordinate reference frame of the magnetic resonance image scanner. Therefore, each bone maintains its relative position as the ankle joint is assembled. Computerized bone representations are in the form of wrapped polygons and the associated points at the triangular vertices. Of the hindfoot bones in the assembly, the user selects a *Reference* set and a *Test* set (Figure 42).

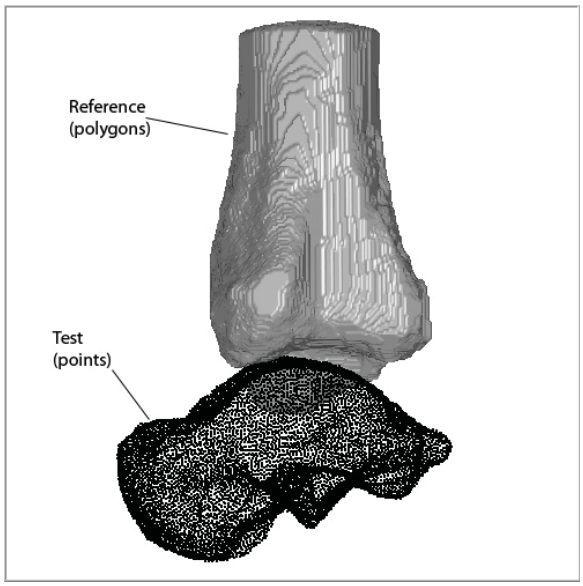

Figure 42. Reference and Test Object Definition

Measurements between articulating surfaces are based on the average tibiotalar cartilage thickness. Contact is identified as bone falling within the proximity of the average cartilage thickness from the talar trochlear surface (Figure 43). These points are projected onto the talar trochlear surface.

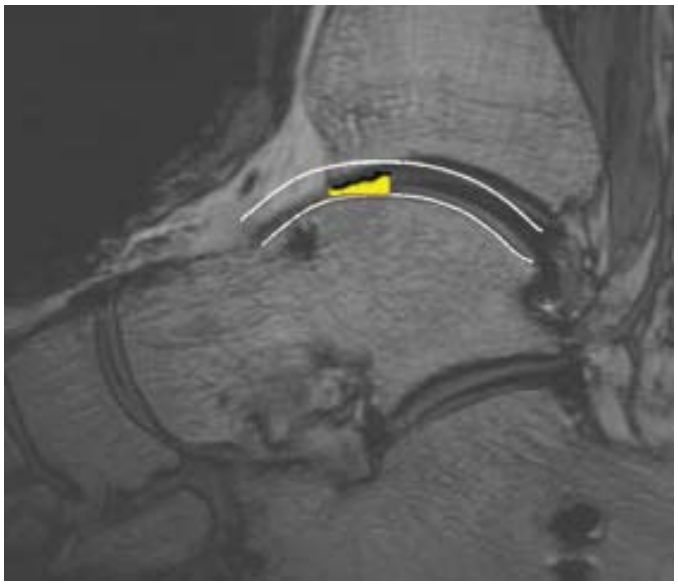

Figure 43. Experimental Contact Area Proximity Measurement

The *3D Compare* tool is used to calculate the distances between surface points of the *Test* object to the surface of the polygons of the *Reference* object. The *Deviation Type* is set to *3D Deviation*, which calculates the shortest distance from the *Test* object to any point on the *Reference* object. A *Maximum Deviation* is set by the user. In this application, the *Maximum Deviation* is set to an average articular cartilage pair thickness. The color contour map of distance is projected onto the target surface and formatted to signify contact area and location. This is carried out over the three dimensional surface (Figure 44).

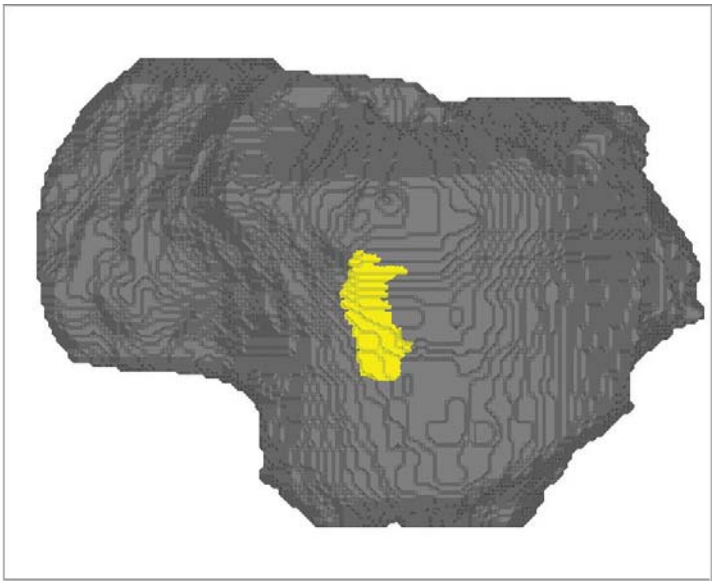

Figure 44. Experimental Estimation of Contact Area and Location
Potential contact; yellow, No contact; gray

Average Model-to-Experiment Comparison

The rotational passive displacement load properties in all three anatomical planes (plantarflexion / dorsiflexion, inversion / eversion and internal / external rotation) are used for model evaluation based on comparison of group means. Load-displacement

properties are obtained using an experimental set-up [24, 66] that allowed the application of pure moments to the calcaneus. Loads were slowly cycled between zero and $\pm 8000 Nmm$. The tibia and fibula are fixed and the motion of the unconstrained talus and calcaneus are recorded via a three dimensional sonic digitizer [24, 66]. All primary and coupled rotations are calculated using an anatomical joint coordinate system [67] applied to the ankle joint, subtalar joint, and ankle joint complex [24, 27].

Measurements

Measurements of range of motion and contact area and its location are used to evaluate the models and test the effects of morphology in response to externally applied loads. Inversion range of motion of the ankle joint complex and talar trochlear contact area and location are measures used to evaluate models, on a one-to-one basis, to their own experimental data. Primary and coupled plantarflexion, dorsiflexion, inversion, eversion, internal rotation, and external rotation of the ankle joint complex, ankle joint, and subtalar joint are measures used to evaluate the models, on an average basis, to experimental data of multiple independent subjects. Inversion range of motion of the ankle joint complex and talar trochlear contact area and location are measures used to test the effects of morphology on a subject-to-subject basis.

Range of Motion

Range of motion of the hindfoot is measured as a finite helical axis rotation (degrees). In order to calculate helical axis rotation, the rigid body dynamic model measures

directional cosines and centroidal positions between inertial reference frames attached to each bone. Ankle joint complex rotation is measured between the calcaneal and fixed tibial inertial frames. Ankle joint rotation is measured between the talar and fixed tibial inertial frames. Subtalar joint rotation is measured between the calcaneal and talar moving inertial frames.

Finite helical axis rotation is a well established technique used to describe three dimensional rotation of a rigid body in space [68, 69] (Equation 4). Accordingly, a finite rotation is described as rotation, Φ, about an axis in a direction defined by a unit vector, n.

$$tr\left[\Phi\right] = 1 + 2\cos\Phi \qquad \textbf{Equation 4}$$

To implement the finite helical axis rotation, the direction cosines and centroidal position at the neutral and loaded states are required. Ω_f is a 4x4 matrix of the direction cosines and centroidal position in the final position (the last time step of the simulation corresponding to the fully loaded position); and Ω_i is a 4x4 matrix of the direction cosines and centroidal position in the initial, or neutral, position (Equation 5).

$$\Phi = \cos^{-1}\left[\frac{1}{2}tr\left(\Omega_f\Omega_i^{-1}\right) - 2\right] \qquad \textbf{Equation 5}$$

Contact Area and Location

Measurements of contact area and location are made relative to a superimposed grid on a two dimensional superior view of the talar trochlear surface. The superior view is oriented relative to the long axis of the tibia in the scanner reference frame [6]. The talar trochlear surface is divided into a 3x3 grid in the shape of a four sided polygon (Figure 45). The near square four sided polygon is fit to the extents of the trochlear surface using AutoCAD®, a general purpose drafting program. The extents of the trochlear surface are identified by selecting (as per the user's perspective) the anterior and posterior borders and the trochlear shoulders. Each of the four edges of the polygon is divided into three equal segments and lines drawn between the divided points creating a 3x3 grid. The grid areas, referred to as zones, are labeled A, B, C, D, E, F, G, H, and I; where A is the anterior-medial zone, B the central-medial zone, C the posterior-medial zone, D the anterior-central zone, E the central zone, F the posterior-central zone, G the anterior-lateral zone, H the central-lateral zone, and I the posterior-lateral zone. Models 4L and 5L are mirrored for sake of visual comparison.

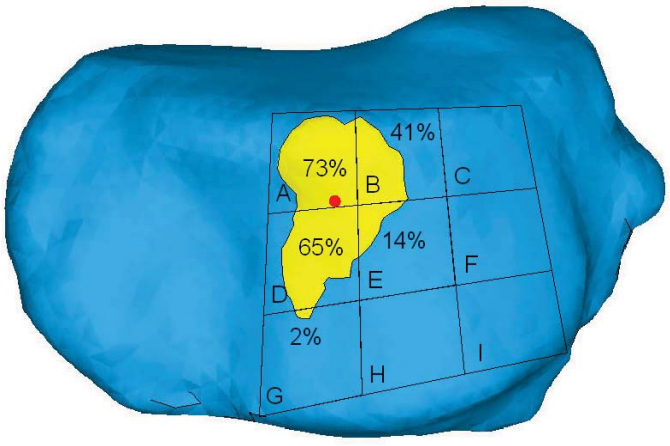

Figure 45. Talar Trochlear Contact - Model-to-Experiment Comparison
Contact area: yellow, contact area centroid: red dot

The contact area is compared between model and experiment as the percentage of each zone (A through I) occupied by contacting area (Figure 45). Similar grid systems are constructed on the model and experimental trochlear surfaces. Each zone area is measured as a unit less value representing the individual zone's total area, or 100%. The contacting area occupied within a particular zone is measured as a unit less value. The contact area coverage in each zone is described as a percentage of the zone area. This provides a unit less ratio of areas independent of scale.

For example, Zone A measures a total unit less area of 1.1095. The unit less contacting area occupied in Zone A is 0.8123. The ratio of contacting area to total area is 0.73, or 73% .

The contact area centroid location is determined by evaluating the area properties of the total contact area (spanning all zones) (Figure 45). The location of the contact area centroid, indicated by a red dot, is identified by the zone it occupies.

Effect of Morphology

The effect of morphology on the mechanical response to externally applied loads is tested by comparing passive mechanical properties on a subject-to-subject basis. Additionally, features are altered on a local scale to test their functional morphology. The subject-to-subject comparison provides an indication of the effects of the morphology of the bones, articulating surfaces, and ligaments across the ankle joint complex by evaluating passive mechanical variations among subjects. Local morphological features are individually modified, such as shape and size of the sustentaculum tali and calcaneofibular ligament orientation, to test the alteration's effect by observing variations in mechanical behavior.

Subject-to-Subject Passive Mechanics Comparison

The subject-to-subject comparison tests the hypothesis by comparing the inversion range of motion and contact area and location for each subject in the intact and injured (sectioned) ligament configurations. In each model, the boundary conditions, external loads, ligament material properties, and cartilage material properties are identical, thus, isolating the effects of the morphology of the bones, articulating surfaces, and ligaments. Therefore, differences in response of inversion range of motion and talar trochlear contact characteristics are dependent on the individual's morphology of the ankle joint complex.

Inversion range of motion across the ankle joint complex is measured for each subject. The effect of morphology on inversion range of motion is evaluated by comparing the upper and lower magnitudes and the standard deviation to the average.

Talar trochlear contact area and contact location is measured for each subject. The contact area measurement, mm^2, is output directly available from the contact elements of the finite element software. The contact area location on the talar trochlear surface is described by identifying its centroidal position relative to a superimposed grid. The contact area is further described by the percentage of the total contact area divided among each zone (Figure 46).

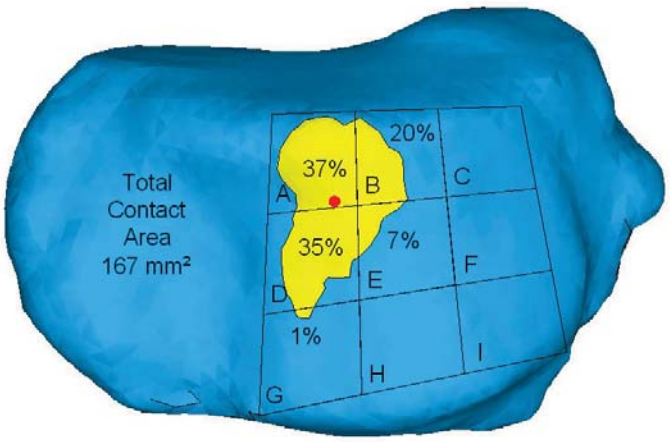

Figure 46. Talar Trochlear Contact - Subject-to-Subject Comparison
Contact area: yellow, contact area centroid: red dot

For example, the total talar trochlear contacting area of a subject is $167 mm^2$ (Figure 46). Zone A is occupied by 37%, or $61.8 mm^2$, of the total contacting area. Variations of the contact area centroid location are identified by indicating the zone it occupies. Variations of the contact area location are further compared by plotting the percent of the total contact area in each zone for each subject to show relative magnitudes and by evaluating the average and standard deviation of percent of total contact area in each zone.

Subject-to-Subject Morphological Variations

Morphological variations of individual features are compared on a subject-to-subject basis. These variations of individual features may influence the passive mechanical response of the hindfoot. Measurements of the calcaneal length, width, and height, calcaneal articular facet configuration, sustentaculum tali inclination, sustentaculum tali dimensions and classification, calcaneofibular ligament orientation, and talar trochlear cartilage thickness distributions are made for each subject. Descriptions of the measurements are given in the Background and Results Sections.

Functional Morphology

The functional morphology of local features is evaluated by altering their properties and observing model behavior. The sustentaculum tali is altered by changing its shape and size and observing inversion range of motion. The orientation of the calcaneofibular ligament is altered by adjusting its calcaneal insertion and variation in inversion range of motion is observed.

Sustentaculum Tali Geometry

The functional morphology of the sustentaculum tali during inversion loadings is evaluated by altering its shape and size in incremental steps and observing its effects on the inversion range of motion. The shape and size of the sustentaculum tali are manipulated by altering the computerized bone representation. All other model parameters are held constant to isolate the effect of the sustentaculum tali. The

alterations, in five steps on a single subject, varied from the unaltered sustentaculum tali to a completely removed, or flush, medial surface. For each alteration, the inversion range of motion across the ankle joint complex is measured.

The rigid body dynamic model is used to simulate inversion loading for each alteration. The calcaneus is replaced with the altered calcaneus in the rigid body dynamic model. The neutral calcaneal position and orientation is maintained relative to the unaltered state preserving a common reference for each simulation.

Calcaneofibular Ligament Orientation

The functional morphology of the calcaneofibular ligament orientation during inversion loading is evaluated by altering the calcaneal insertion from vertical to horizontal in incremental steps and observing its effect on the inversion range of motion. The inversion range of motion across the ankle joint complex is measured to study the morphological dependency of the calcaneofibular ligament orientation in resisting an inversion loading.

The calcaneal insertion location of the calcaneofibular ligament in the rigid body dynamic model is manipulated to orientations; vertical, 30 deg, 60 deg, and horizontal measured from the long axis of the tibia. The actual ligament orientation is also included in the studying the functional morphology of calcaneofibular ligament orientation.

Chapter 4: Results

Six subject specific hindfoot models capable of capturing passive mechanical properties are developed. Each model is evaluated on a one-to-one basis to its own experimental data and on an average basis to independent experimental data. To test the effects of morphology of the ankle joint complex, variations of inversion range of motion and talar trochlear contact of each model are compared on a subject-to-subject basis. Variations of morphological features are compared between models. Variations of inversion range of motion due to alterations of the sustentaculum tali and calcaneofibular ligament orientation are evaluated, testing the functional morphology of these features.

Model Development

Rigid body dynamic and finite element models are developed from patient specific magnetic resonance image data (Figure 47). The dynamic model captures range of motion, load-displacement characteristics, ligament recruitment, and contact force for a variety of loadings and boundary conditions. The finite element model enhances the description of contact area.

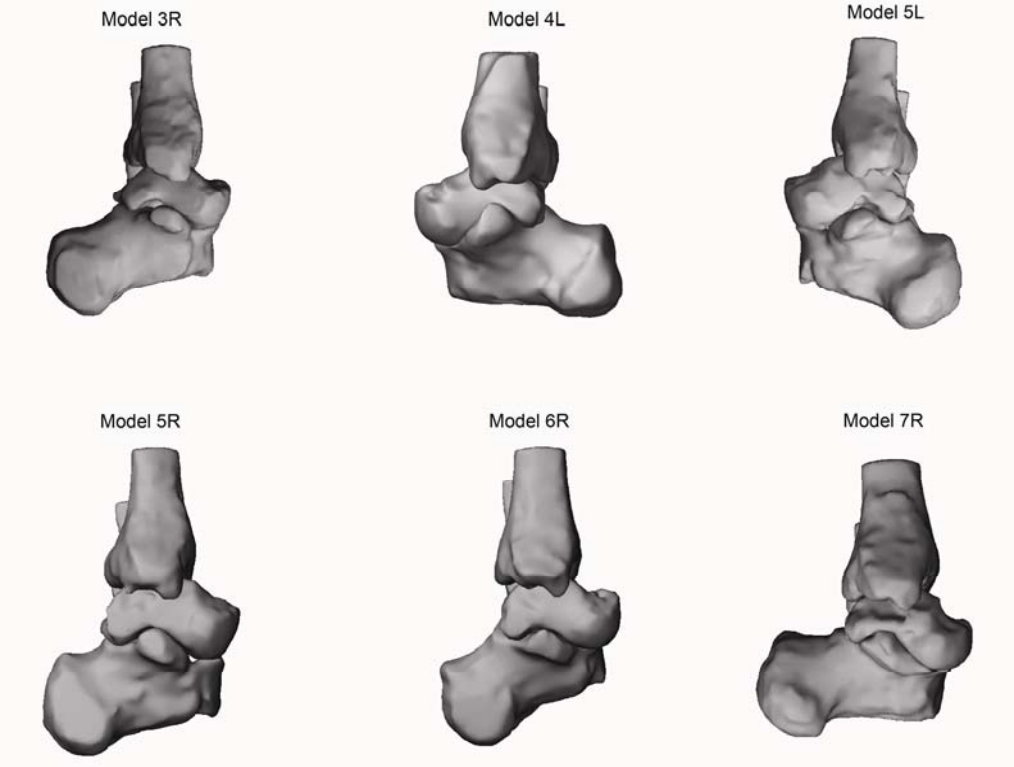

Figure 47. Medial View of All Hindfoot Models in the Neutral Position

Rigid Body Dynamic Model

The rigid body dynamic model is evaluated in the intact ligament configuration under static externally applied inversion and cyclic externally applied plantarflexion / dorsiflexion, inversion / eversion and internal / external loads. The model is evaluated in the injured ligament configuration under static inversion load. Static loads are applied from the neutral position, increased, and held at the maximum externally applied load (Figure 48). Cyclic loads are applied from the neutral position and loaded over the full range of motion, for example, inversion to eversion, then back to inversion for three cycles (Figure 49).

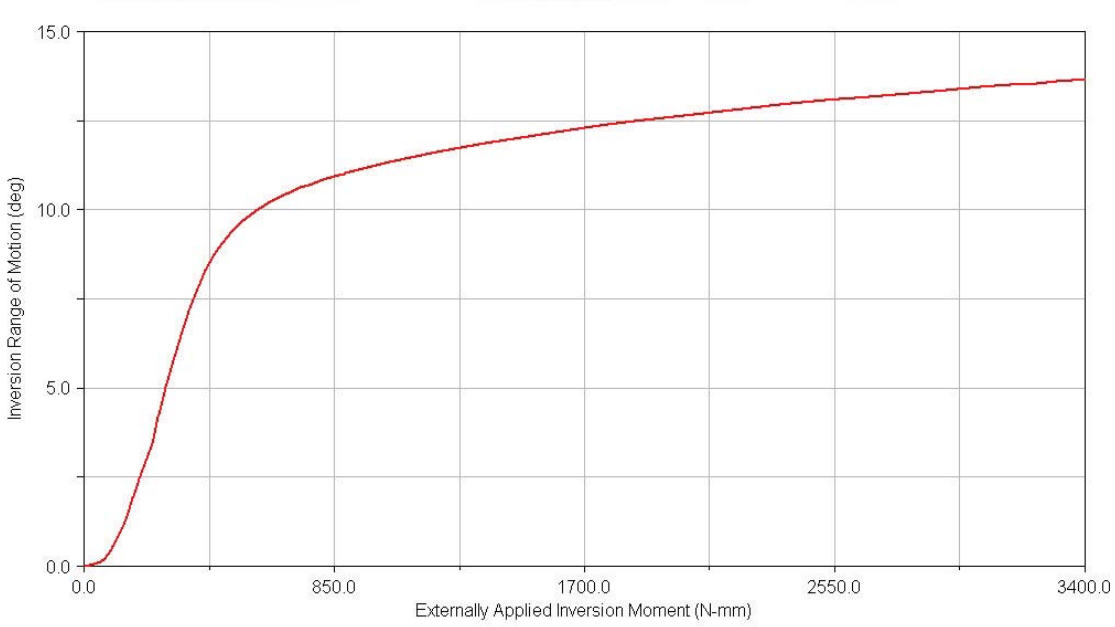

Figure 48. Load-Displacement Characteristics

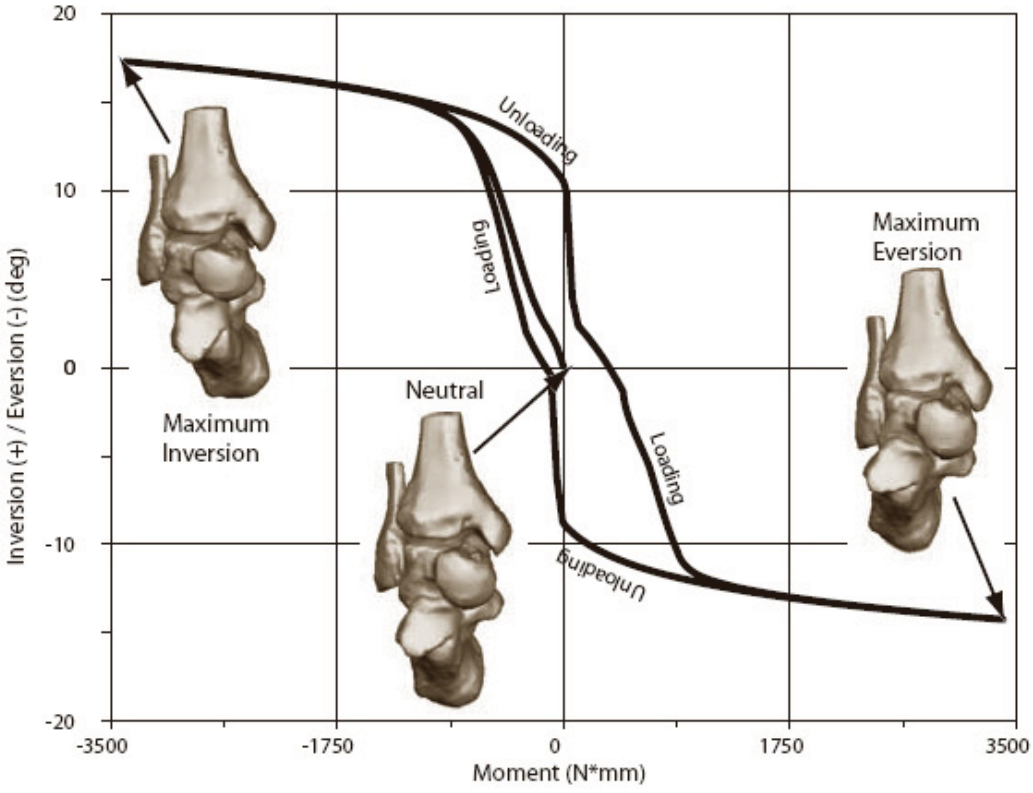

Figure 49. Load-Displacement with Hysteresis

Ankle complex inversion range of motion is the rotation (degrees) of the calcaneus relative to the tibia from the neutral position to the inversion position loaded by an inversion moment. For example, the inversion range of motion is 13.7° (Figure 48).

Hysteresis during cyclic motion is captured by the rigid body dynamic (Figure 49). Once cyclic motion has stabilized, in one loading cycle from neutral, loading and unloading do not follow the same path. Viscoelastic ligament material properties and non-linear contact characteristics are sources of hysteresis.

The viscoelastic ligament material model behaves nonlinearly with an initial high flexibility followed by an exponentially increasing stiffness with increasing ligament strain [51] (Figure 50, and Appendix A). The calcaneofibular ligament, for example, markedly increases stiffness at approximately 9% strain.

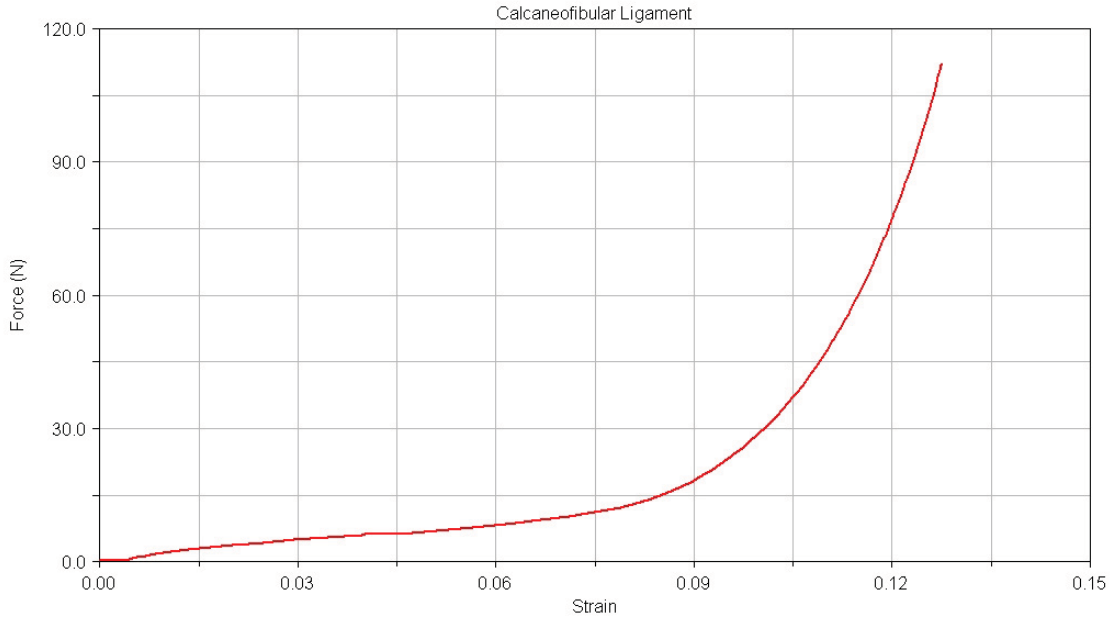

Figure 50. Ligament Force Characteristics

The contact model behaved nonlinearly with an initial high flexibility followed by an exponentially increasing stiffness with penetration depth (Figure 51). The articular cartilage of the tibiotalar joint, for example, deformed with a low stiffness up to approximately $1.0mm$, then, increased in stiffness at approximately 40% cartilage compression.

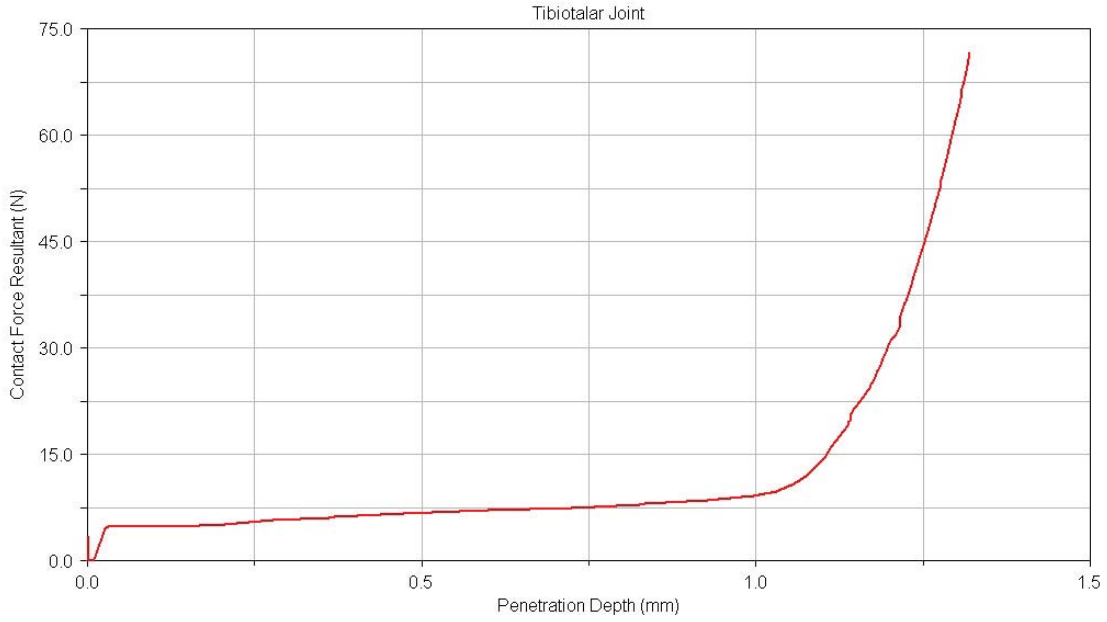

Figure 51. Contact Characteristics
Example: average tibiotalar cartilage thickness; 2.3 mm.

Contact force is represented as a single resultant vector. The contact force resultant acts along a line directed from the centroid of the interpenetrating volume to the normal on the contacting surface. The rigid body contact can be viewed by manipulating the graphical representation of the bone surface models (Figure 52). The outline represents a continuous line common on both articulating surfaces at the intersection of the penetrating volumes.

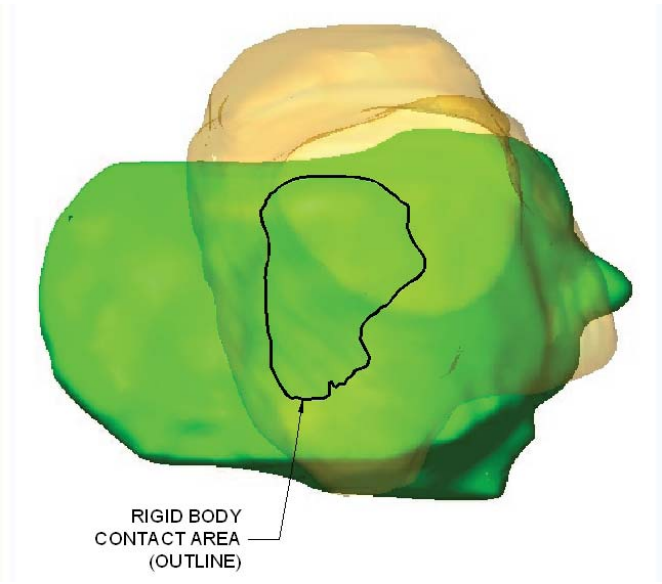

Figure 52. Rigid Body Contact Area
Superior aspect of talus viewed through translucent tibia.

The tibial articular cartilage thickness and the talar trochlear cartilage thickness are measured at nine locations in the tibiotalar joint. Three measurements of tibial and talar cartilage thickness (anterior, middle, and posterior) are taken in a sagittal oriented view plane in the three dimensional magnetic resonance image reconstruction (Figure 53). The measurements are repeated with the view plane located medially, centrally, and laterally across the trochlear surface.

Figure 53. Tibiotalar Cartilage Thickness

At each location, the tibial and talar cartilage thicknesses are summed. The average of the nine tibiotalar cartilage thicknesses is calculated (Table 8).

Table 8. Tibiotalar Average Cartilage Thickness

Subject	**Average Thickness**, mm
3R	2.7 ± 0.4
4L	2.3 ± 0.7
5L	2.7 ± 0.6
5R	2.8 ± 0.5
6R	2.3 ± 0.5
7R	3.0 ± 0.6

Solution time for the statically loaded models was approximately twenty minutes. For cyclically loaded models, the solution time was approximately one hour for three cycles.

Finite Element Model

Contact area is recovered by removing the interpenetrated rigid body volume by deformation of the articular surface in the finite element model. The finite element model is used in conjunction with the rigid body dynamic simulations for evaluating the model on the one-to-one basis and testing the effects of morphology for the intact and injured ligament configurations.

The talus and calcaneus in the finite element model are repositioned and reoriented from their neutral state to that corresponding to the maximum applied inversion moment as determined by the positional output of the rigid body dynamic model. The articulating surfaces in the undeformed finite element model are initially interpenetrated as in the rigid body dynamic model. The finite element contact solution removes the initial penetration by deformation of the articular surface (Figure 54).

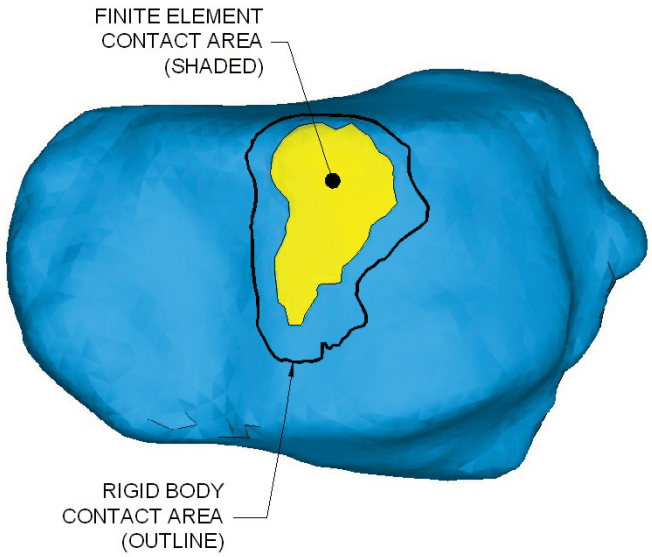

Figure 54. Finite Element Contact Area

Residual contact penetration is less than $0.01mm$, or 0.9%, of the underlying element depth based on the thinnest average talar cartilage thickness of the six specimens. A contact stiffness parameter, FKN, of 1.0 is used. A penetration tolerance, $FTOLN$, of 0.003 is used.

A sensitivity study of the penetration tolerance parameter reveals low sensitivity on contact area and location. A penetration tolerance default value of 0.01 produces a residual penetration of $0.04mm$. Tightening the penetration tolerance to 0.003 achieved the target residual penetration. The change in contact area between the two penetration tolerance settings was less than 1%. Computationally, four to five additional equilibrium iterations were required.

Approximately 9,000 triangular surface polygons are used to represent each bone in the rigid body dynamic model and approximately 4,500 in the finite element model. During the decimation process, small deviations from the original surface occurred. Shape preservation was enforced and the maximum deviation was $0.04mm$, or 4% of the minimum average cartilage thickness (Figure 55).

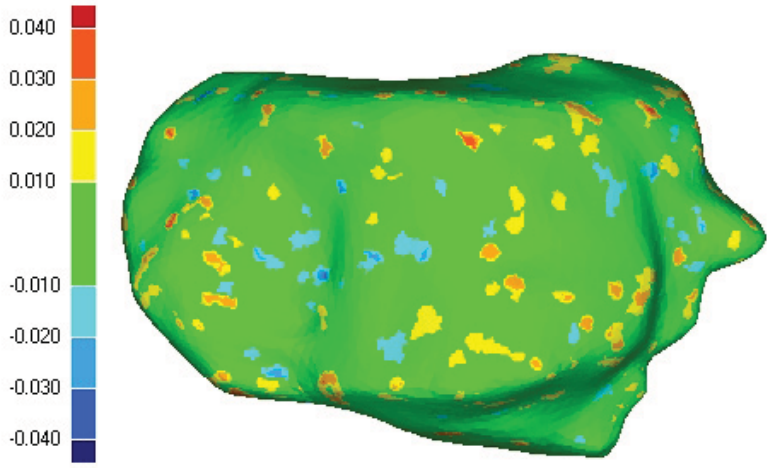

Figure 55. Bone Surface Representation Deviation - Rigid Body vs Finite Element

A mesh density convergence study shows that one element through the thickness (Figure 36) is sufficient to capture the contact area and location. A mesh discretization dividing the solid and contact element size in half, on the surface and through the thickness, has a 4% effect on the contact area.

The average number of elements used in the finite element model is 123,000. The average number of nodes is 21,000, varying approximately $\pm 10\%$. Of these elements, approximately 65,000 are solid representing cartilage and the remaining 58,000 are contact elements overlying the surface.

The linear elastic material properties exhibit a low sensitivity to the estimation of contact area. The modulus of elasticity of articular cartilage is varied from $3.74 \times 10^{-3} MPa$ to $37.4 MPa$. The difference in contact area from one extreme of the range to the other is 16% (Figure 56).

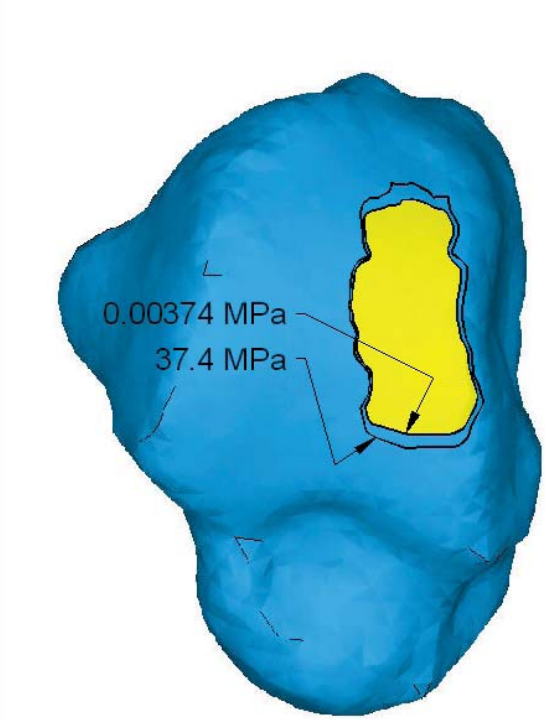

Figure 56. Modulus of Elasticity - Contact Area and Location Sensitivity

The solution time for the finite element model ranges from thirty minutes to two hours. The solution time is dependant on the number of equilibrium iterations necessary for convergence. All simulations require only one time step with approximately ten to fifteen equilibrium iterations. In a few simulations, the time step increment required bisection, as the automatic time step initial assumption did not converge. In most simulations, the default time step increment provided an efficient solution, and bisection was associated with longer solution times. The simulations are run on a $2.21GHz$ dual core processor with $3GB$ of random access memory on a $32bit$ operating system.

Model Evaluation

The six patient specific hindfoot models are evaluated on a one-to-one basis and an average basis for their ability to reproduce passive mechanical properties determined by experiment. The one-to-one basis compares the model predicted inversion range of motion across the ankle joint complex and contact area and location on the talar trochlear articulating surface against the subjects own experimental data. The average basis compares the model predicted primary and coupled range of motion in plantarflexion / dorsiflexion, inversion / eversion, and internal / external rotation against fifteen independent specimens in the intact ligament configuration.

One-to-One Model-to-Experiment Comparison

The one-to-one model-to-experiment evaluation compares the inversion range of motion and contact area and location in the intact and injured ligament (anterior talofibular ligament and calcaneofibular ligament sectioned) configurations.

Intact Ligament Configuration

The inversion range of motion of the ankle joint complex with an intact ligament configuration is calculated using the rigid body dynamic model. An external inversion moment was applied to the calcaneus. The calcaneus is constrained permitting rotations only in the plane of the applied moment. The tibia and fibula are fixed against translations and rotations in all degrees of freedom. The model predicted inversion range

of motion is compared to its corresponding experimentally measured inversion range of motion (Table 9).

Table 9. One-to-One Model-to-Experiment Intact Inversion Range of Motion

Specimen	Model	Experiment	% Difference
3R	10.9°	11.8°	8%
4L	8.3°	13.9°	40%
5L	13.7°	11.3°	21%
5R	10.2°	5.8°	76%
6R	16.3°	21.8°	25%
7R	6.2°	6.4°	3%
Avg. ± Std. Dev.	10.9° ± 3.6°	11.8° ± 5.8°	

The contact area and location on the talar trochlear articular surface is calculated using the finite element model. The finite element model is simulated at the position of maximum inversion determined by the rigid body dynamic model.

The model and experiment percent contact area coverage in each zone on the talar trochlear articulating surface are compared graphically side by side. Model results are shown on the left and experimental results on the right. In all figures, the view is superior with respect to the trochlear surface, with the anterior aspect of the talus on the left, the lateral aspect on the bottom, the posterior aspect on the right, and the medial aspect on the top. The bar graph shows a side by side model to experiment comparison of the percent contact area coverage in each contact area zone.

The model to experiment comparison of percent contact area coverage and spatial distribution among zones of subject 3R are within a 16% difference in Zones A, B, D, E, and G (Figure 57). The average percent difference between zones is 8%. Experimental data includes 1% contact area coverage in lateral-central Zone H, where the model does not. The contact area centroid lies in Zone A in the model and in Zone D in the experiment. However, model and experiment centroids share the common border between Zones A and D. The shape of the model contact area has an uncanny resemblance to the continent Africa.

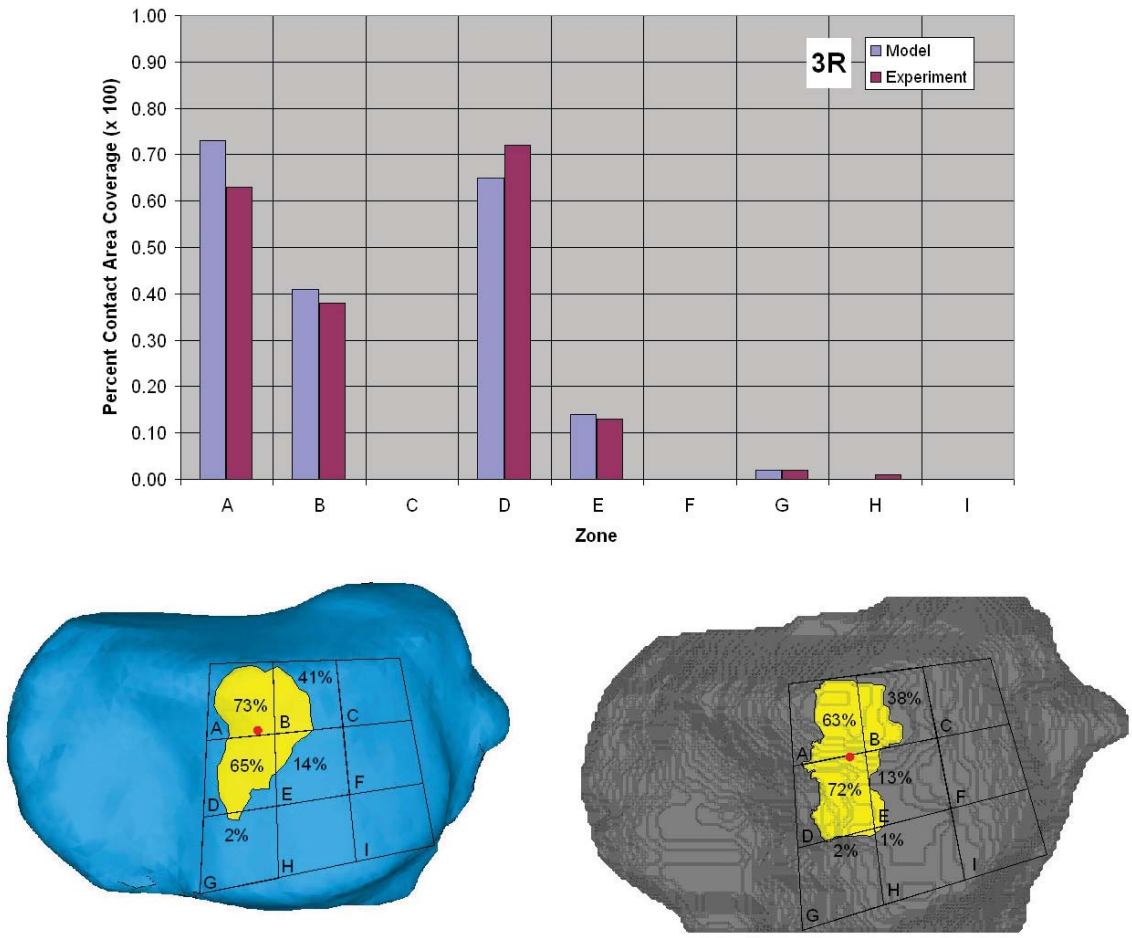

Figure 57. Model-to-Experiment Intact Contact Area and Location, 3R

The model to experiment comparison of percent contact area coverage and spatial distribution among zones of subject 4L are within a 17% difference in Zone B (Figure 58). The model predicts contact in Zone A, where experiment does not. The contact area centroid in the model and experiment are both located near the middle of the anterior edge of Zone B.

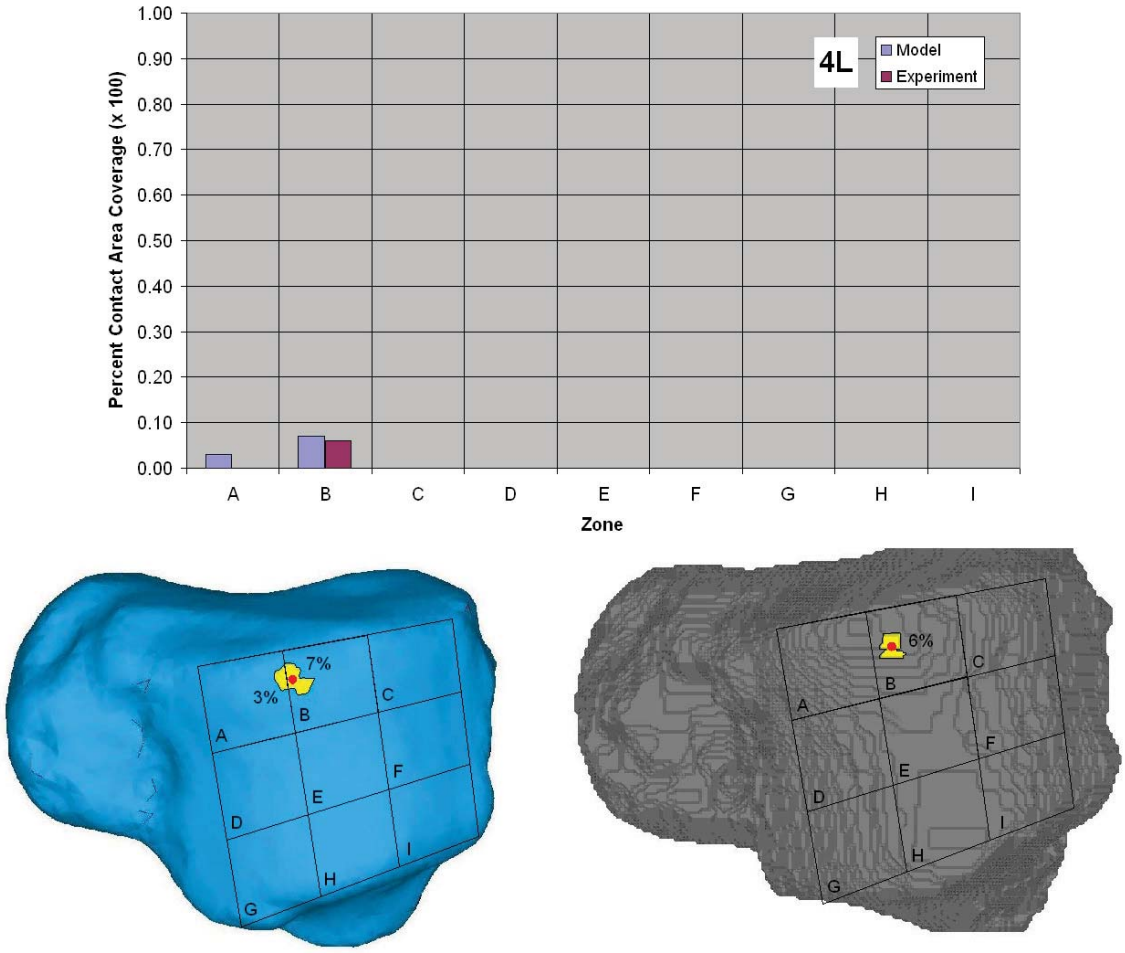

Figure 58. Model-to-Experiment Intact Contact Area and Location, 4L

The model to experiment comparison of percent contact area coverage and spatial distribution among zones of subject 5L are within a 62% difference in Zones A and D (Figure 59). Experimental data includes 1% contact area coverage in Zone E, where the model does not. The contact area centroid is located in Zone A in the model and Zone D in the experiment.

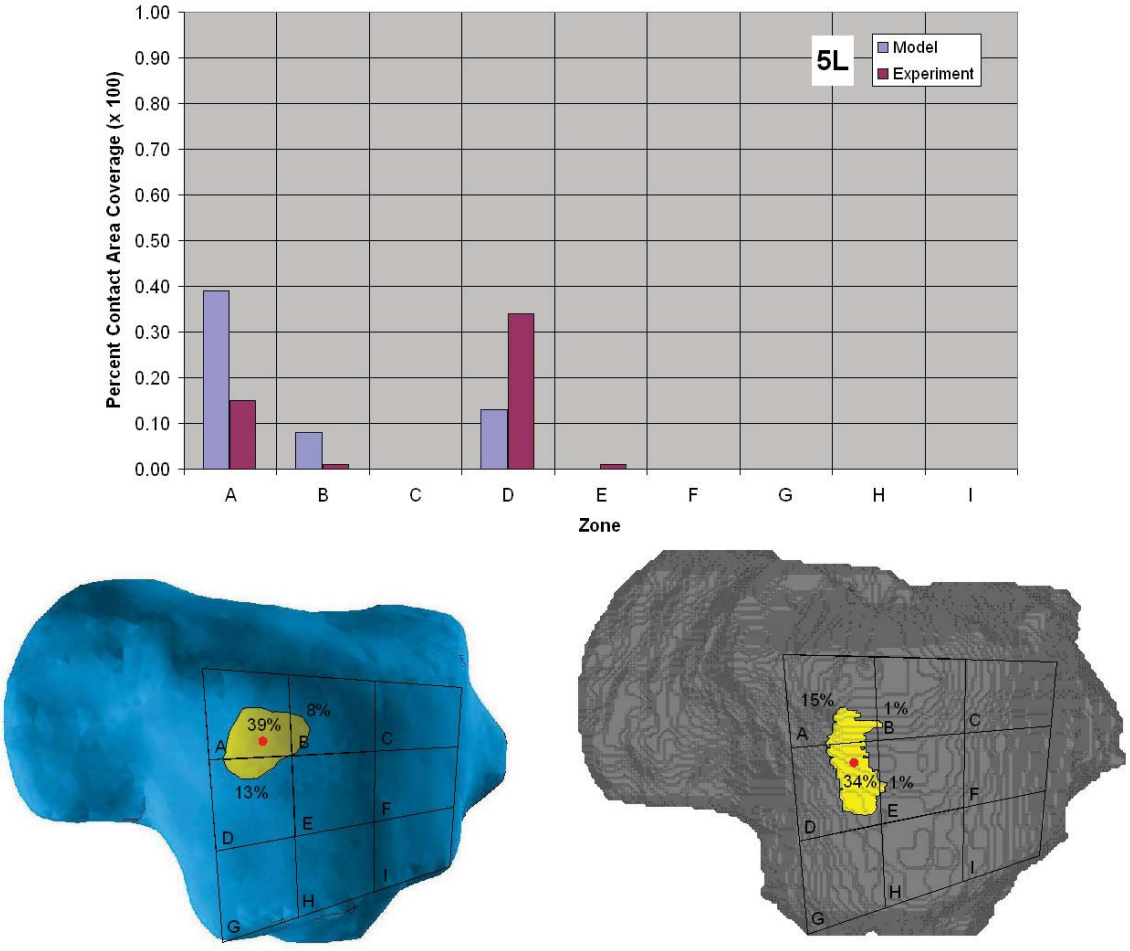

Figure 59. Model-to-Experiment Intact Contact Area and Location, 5L

The model to experiment comparison of percent contact area coverage and spatial distribution among zones of subject 5R are on average 56% different (Figure 60). The contact area centroid is located in Zone E in both model and experiment. Both centroids share an anterior position in Zone E, but the model favors the medial side while the experiment favors a central location.

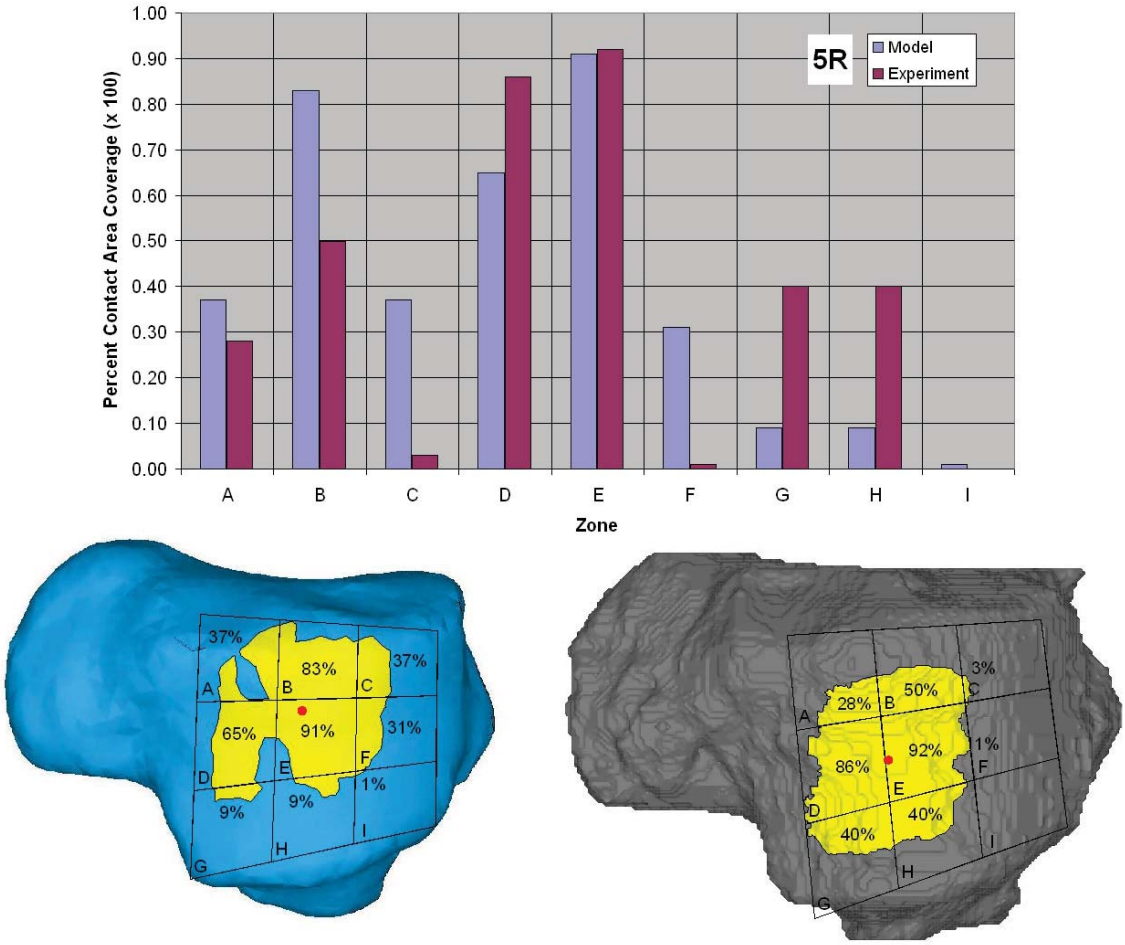

Figure 60. Model-to-Experiment Intact Contact Area and Location, 5R

The model to experiment comparison of percent contact area coverage and spatial distribution among zones of subject 6R are within a 40% difference in Zones A, B, D, and E (Figure 61). The average percent difference between zones is 33%. The contact area centroid is located in the lateral-posterior corner of Zone A in the model and in the lateral-anterior corner of Zone B in experiment.

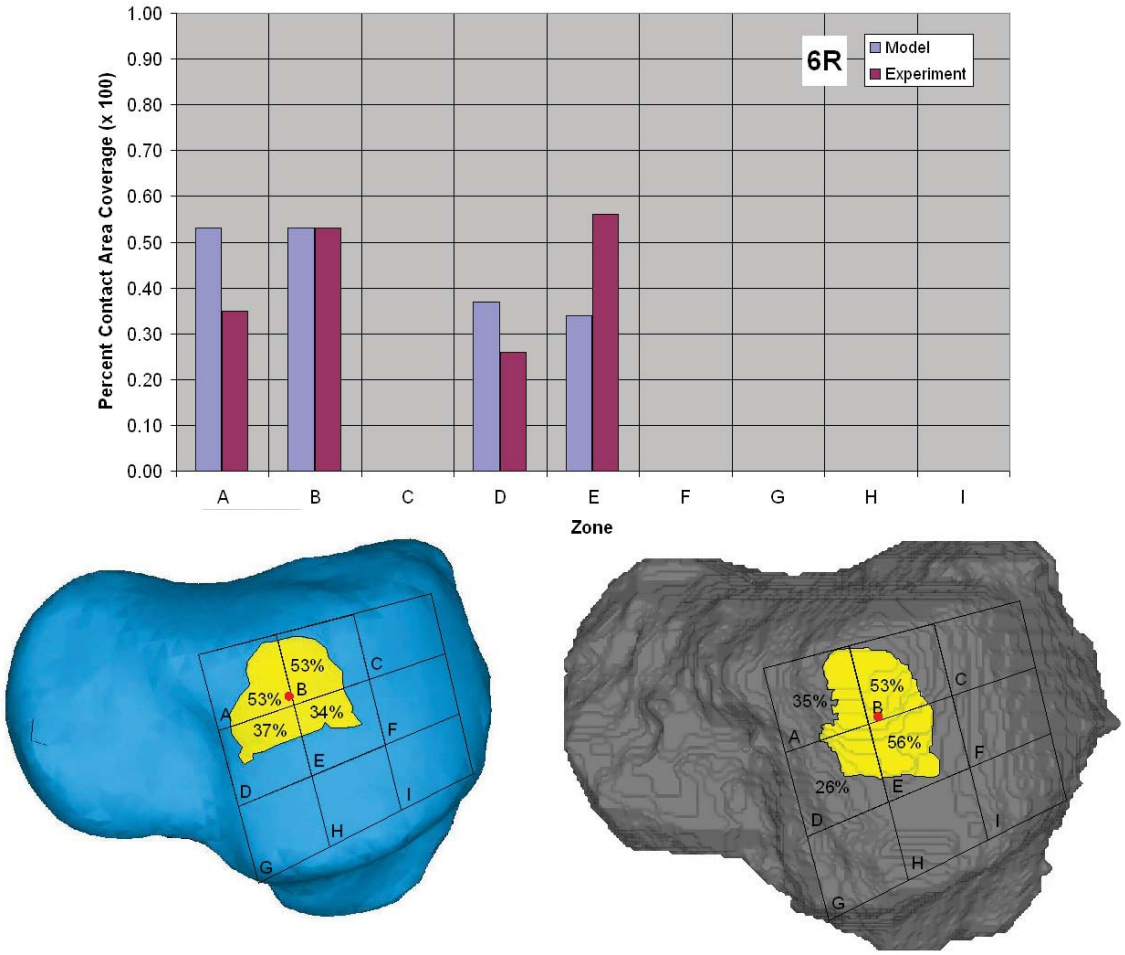

Figure 61. Model-to-Experiment Intact Contact Area and Location, 6R

The model to experiment comparison of percent contact area coverage and spatial distribution among zones of subject 7R are within a 48% difference in Zones A, B, C, D, E, and F (Figure 62). The average percent difference between zones is 25%. These are oblong slot-shaped areas oriented anterior to posterior contained within the medial side and anterior to posterior central strip. The contact area centroid is located on the medial-central border of Zone E in both model and experiment.

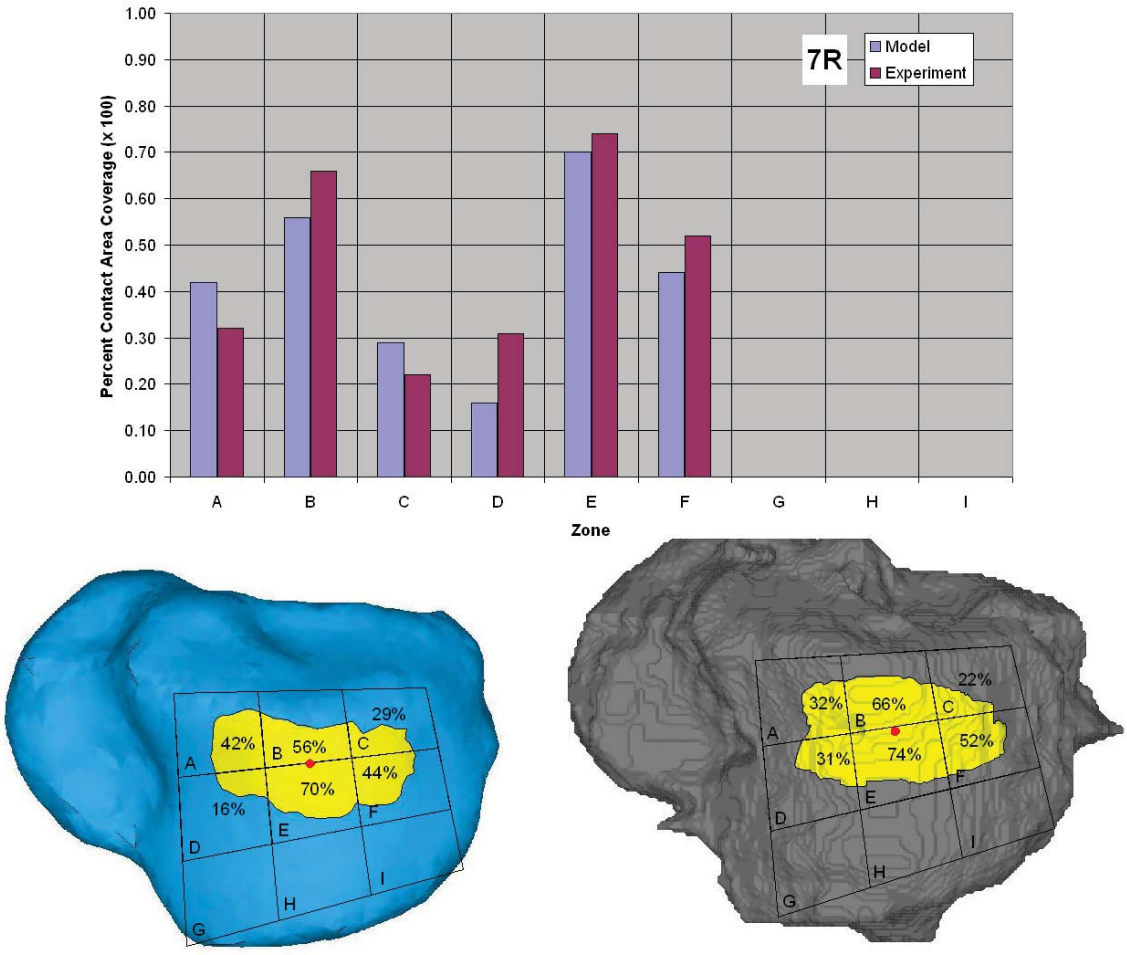

Figure 62. Model-to-Experiment Intact Contact Area and Location, 7R

Injured Ligament Configuration

The inversion range of motion of the ankle joint complex with an injured (sectioned) ligament configuration is calculated using the rigid body dynamic model. An external inversion moment is applied to the calcaneus. The calcaneus is constrained permitting rotations only in the plane of the applied moment. The tibia and fibula are fixed against translations and rotations in all degrees of freedom. The model predicted inversion range of motion is compared to its corresponding experimentally measured inversion range of motion (Table 10).

Table 10. One-to-One Model-to-Experiment Injured Inversion Range of Motion

Specimen	Model	Experiment	% Difference
3R	40.0°	24.2°	65%
4L	27.9°	22.5°	24%
5L	28.3°	22.2°	27%
5R	33.6°	21.1°	59%
6R	38.8°	30.8°	26%
Avg. ± Std. Dev.	33.7° ± 5.6°	24.2° ± 3.9°	

The contact area and location on the talar trochlear articular surface is calculated using the finite element model. The finite element model is simulated at the position of maximum inversion determined by the rigid body dynamic model.

In both model and experiment of subject 3R, contact is not present (Figure 63). This indicates that the ankle joint completely opened, thus losing tibiotalar contact.

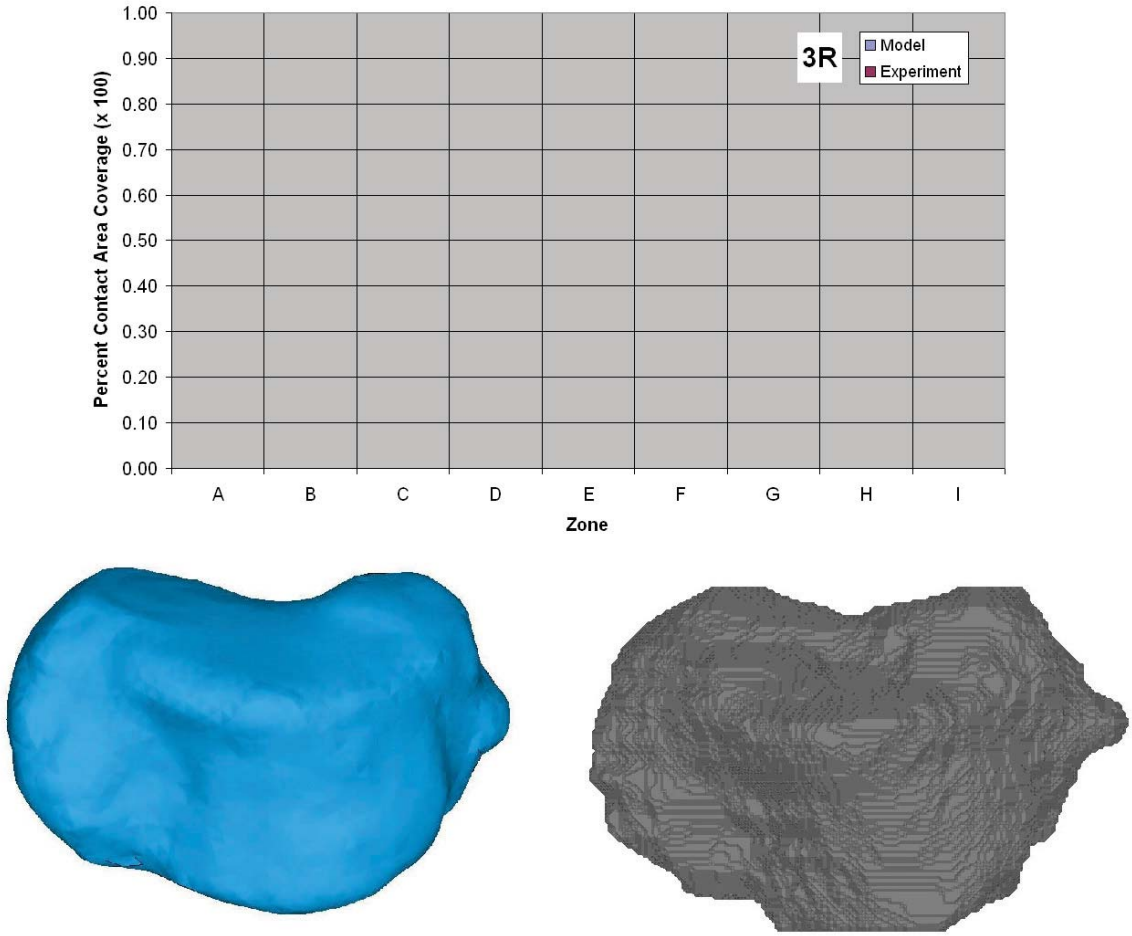

Figure 63. Model-to-Experiment Injured Contact Area and Location, 3R

The model to experiment comparison of percent contact area coverage and spatial distribution among zones of subject 4L are within a 58% difference in Zones A and B (Figure 64). Experimental data includes contact in Zones D and E, where the model does not. The contact area centroid is located in the anterior portion of Zone B in model and experiment.

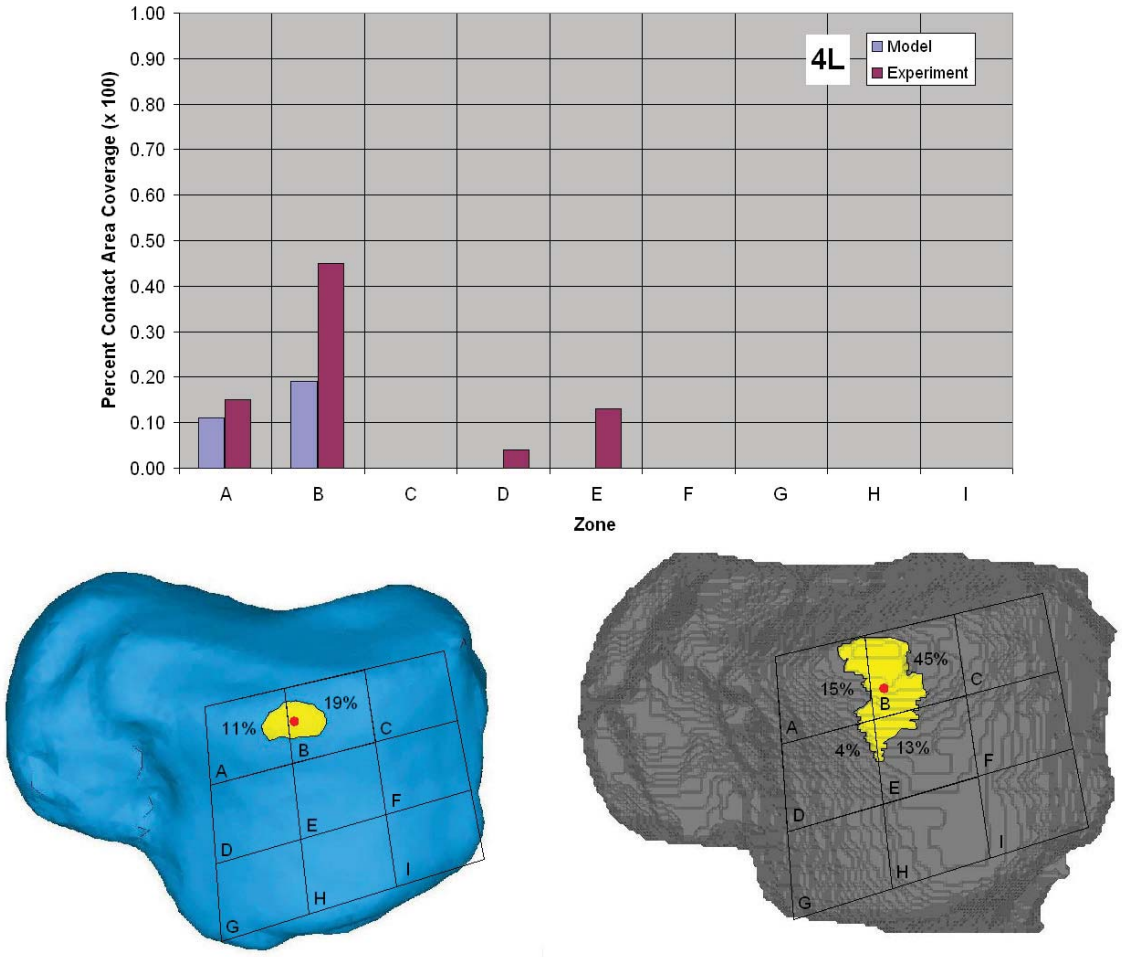

Figure 64. Model-to-Experiment Injured Contact Area and Location, 4L

The model results of subject 5L do not exhibit contact (Figure 65). Contact is present in the experiment in the anterior-medial Zones; A, B, D, and E with its centroid located in the anterior-lateral corner of Zone B.

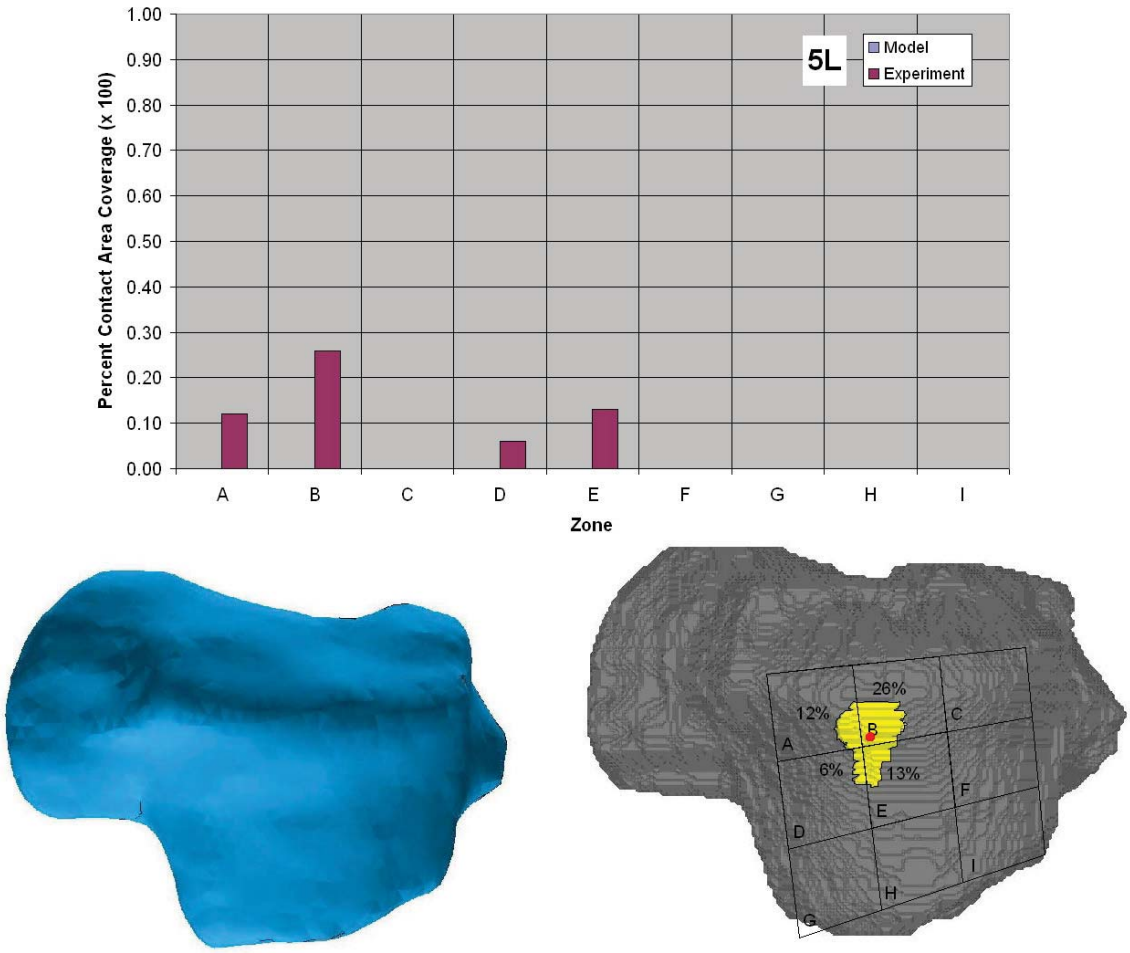

Figure 65. Model-to-Experiment Injured Contact Area and Location, 5L

The model to experiment comparison of percent contact area coverage and spatial distribution among zones of subject 5R share contact in Zone A (Figure 66). Experimental data included contact in Zones B, D, and E, where the model does not. The contact area centroid is located in Zone A for both model and experiment.

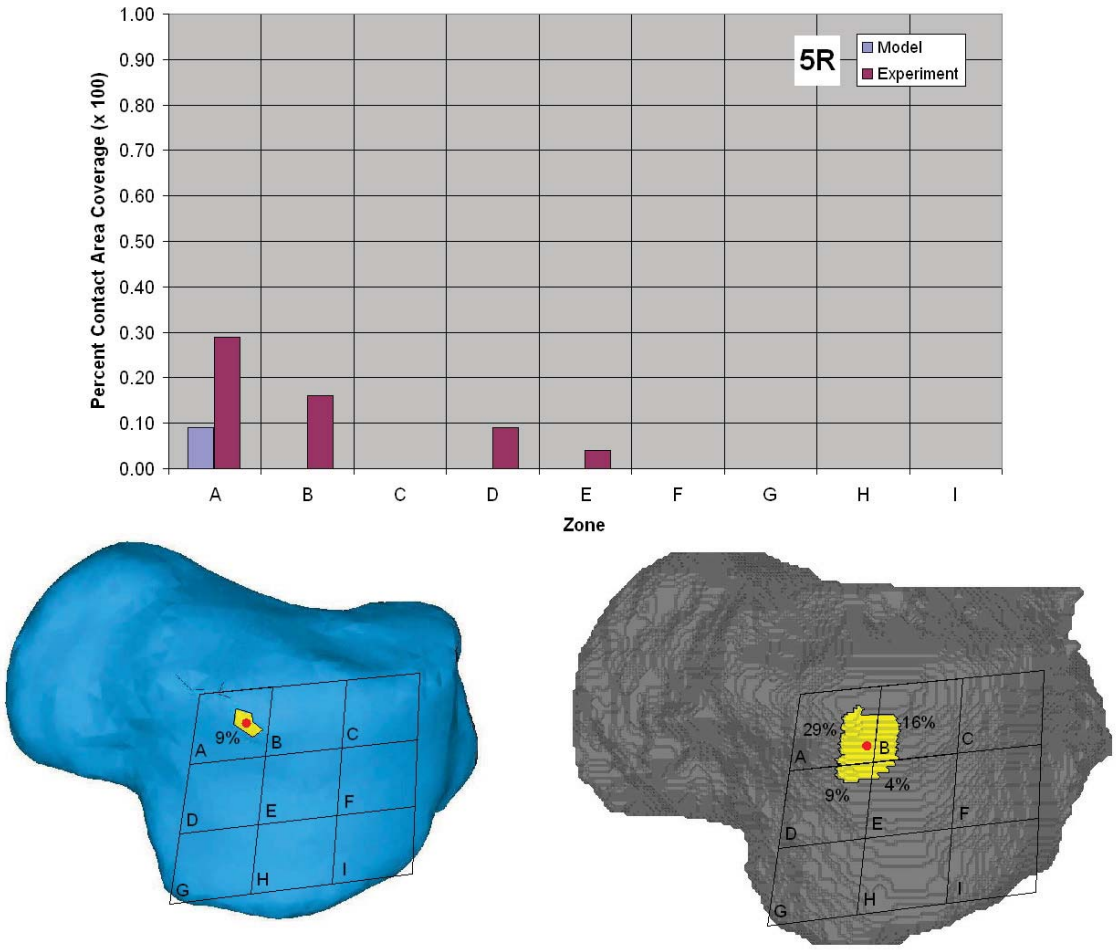

Figure 66. Model-to-Experiment Injured Contact Area and Location, 5R

The model to experiment comparison of percent contact area coverage and spatial distribution among zones of subject 6R are on average 103% different (Figure 67). The contact area centroid is located Zone B in both model and experiment.

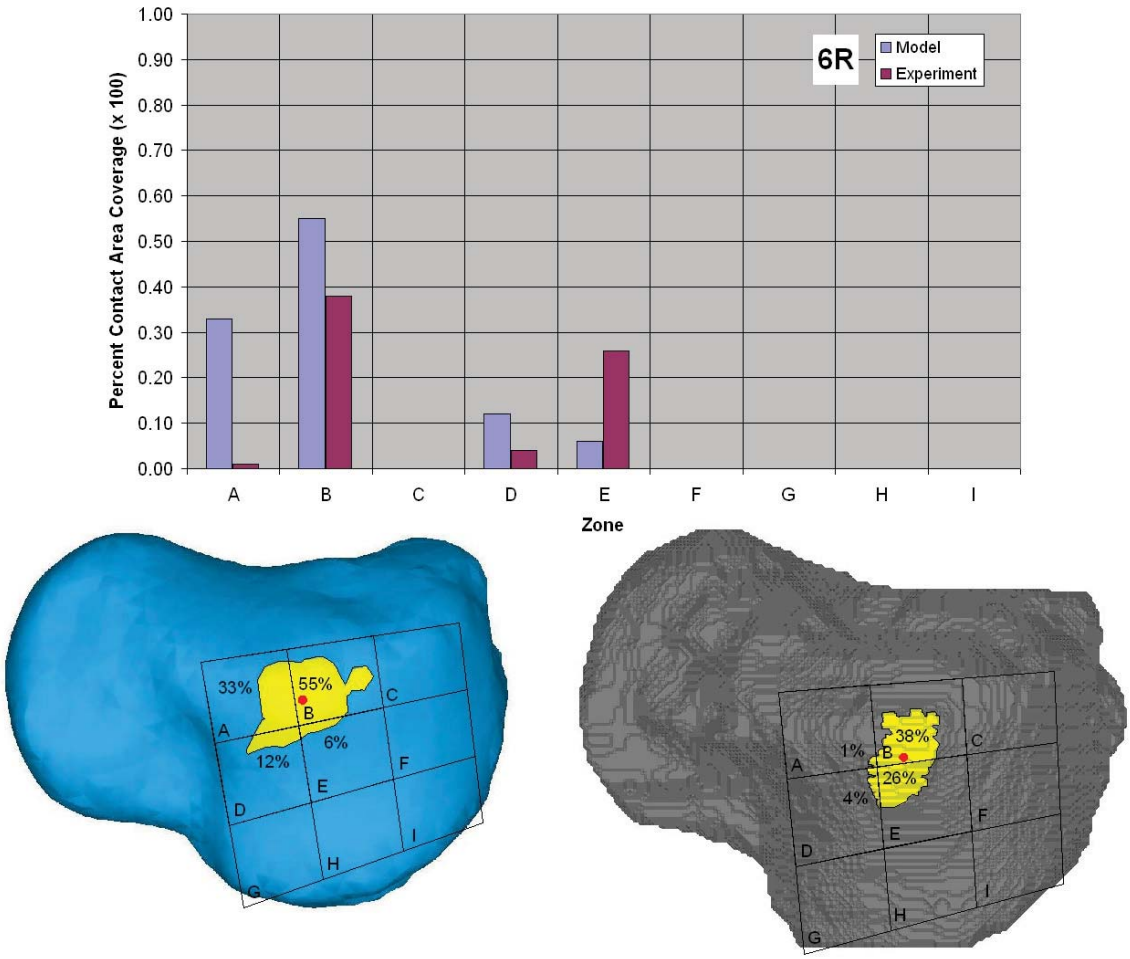

Figure 67. Model-to-Experiment Injured Contact Area and Location, 6R

Average Model-to-Experiment Comparison

The average model-to-experiment evaluation compares plantarflexion / dorsiflexion, inversion / eversion, and internal / external primary and coupled range of motion of the ankle joint complex, tibiotalar joint, and subtalar joint. The average range of motion of the six rigid body dynamic simulations is compared to the average experimental data of fifteen independent cadaveric specimens (Figure 68 and Figure 69). The boundary conditions of the experiment and model fix the tibia and talus against translations and rotation in all degrees of freedom while the talus and calcaneus are free in all degrees of freedom.

	Rotation at the AJC in degrees											
	Plantarflexion		Dorsiflexion		Inversion		Eversion		Internal rotation		External rotation	
	Model	Experiment	Model	Experiment	Model	Experiment	Model	Experiment	Model	Exp	Model	Experiment
Direction of applied moment												
Plantarflexion												
AVG	**39.6**	**40.9**			9.0			0.4	0.4	2.4		
STDV	11.7	4.3			9.5			4.7	7.6	3.5		
Dorsiflexion												
AVG			**35.3**	**24.7**	0.4			0.5		0.4	0.6	
STDV			7.0	3.2	4.6			5.0		5.8	9.6	
Inversion												
AVG	26.0	22.4			**16.1**	**16.3**			11.0	21.9		
STDV	6.3	9.1			8.5	3.9			12.5	8.7		
Eversion												
AVG		11.8	17.1				**13.2**	**15.9**			0.0	11.0
STDV		10.3	13.1				5.8	4.4			7.0	6.9
Internal rotation												
AVG	8.1	14.4			5.6	5.9			**26.6**	**29.8**		
STDV	9.7	6.9			5.1	2.8			11.7	7.6		
External rotation												
AVG		9.8	17.3				8.4	6.3			**15.0**	**22.0**
STDV		9.4	8.0				6.6	2.7			5.6	6.0

Figure 68. Average Range of Motion of the Ankle Joint Complex

The percent difference in range of motion predicted by the model and determined by experiment are 3% for plantarflexion, 43% for dorsiflexion, 1% for inversion, 17% for eversion, 11% for internal rotation, and 32% for external rotation (Figure 68).

	AJC		AJ		STJ	
	Model	Experiment	Model	Experiment	Model	Experiment
Plantarflexion (deg)						
AVG	39.6	40.9	26.9	32.7	10.6	9.0
STDV	11.7	4.3	7.9	3.8	7.1	4.1
Dorsiflexion (deg)						
AVG	35.3	24.7	27.4	19.7	6.5	5.4
STDV	7.0	3.2	4.2	4.0	4.9	3.2
Inversion (deg)						
AVG	16.1	16.3	4.8	4.6	12.8	15.0
STDV	8.5	3.9	5.9	4.9	7.9	5.7
Eversion (deg)						
AVG	13.2	15.9	4.7	6.3	9.8	8.5
STDV	5.8	4.4	1.8	4.4	5.1	3.4
Internal rotation (deg)						
AVG	26.6	29.8	7.0	14.3	20.7	15.6
STDV	11.7	7.6	4.7	3.7	12.4	6.6
External rotation (deg)						
AVG	15.0	22.0	5.1	12.2	10.5	10.2
STDV	5.6	6.0	4.6	3.7	7.1	5.4

Figure 69. Average Range of Motion of the Tibiotalar and Subtalar Joints
Primary range of motion (in bold)

Both model and experimental average data show negligible coupling (less than 2.4º) associated with dorsiflexion and plantarflexion with an exception of an average of 9 ± 9.5º of inversion coupled with plantarflexion exhibited by the models (Figure 68). Both model and experiment show plantarflexion and internal rotation coupled with inversion. The experimental data shows, on average, plantarflexion and external rotation coupled with eversion. In contrast, the models predict only dorsiflexion coupled with eversion. Both the model and experiment show plantarflexion and inversion coupled with internal rotation and eversion coupled with external rotation.

Similar to the average experimental data, all six models exhibit non-linear load-displacement behavior, which manifested as high initial flexibility around neutral that decreased towards the extreme ranges of motion, and viscoelastic behavior, which manifested as hysteresis (Figure 49, Figure 70, and Figure 71).

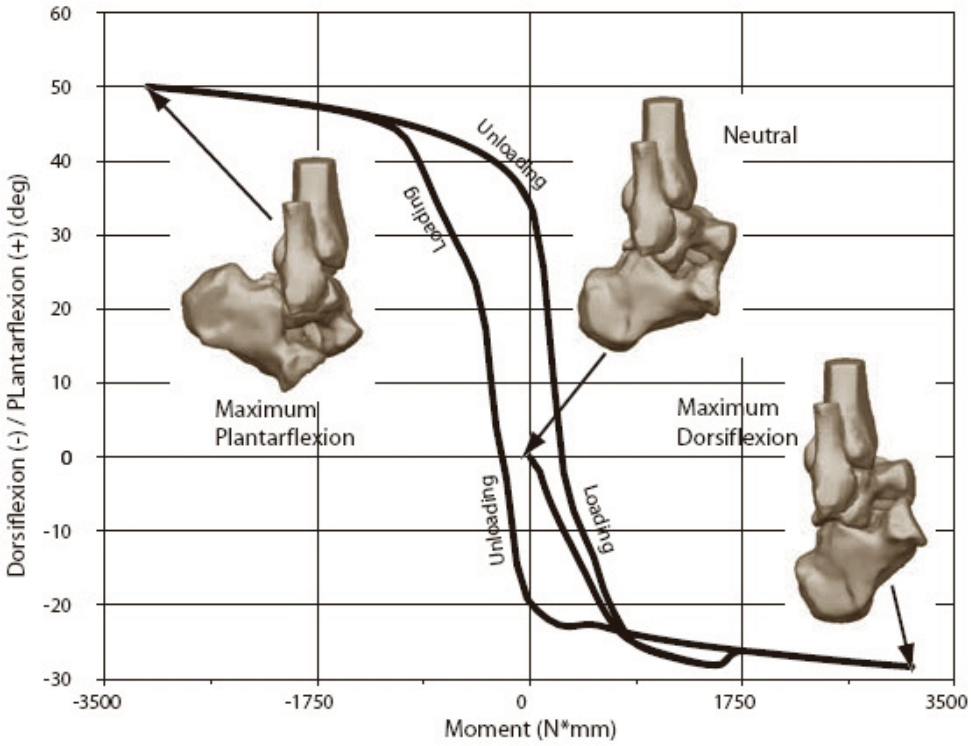

Figure 70. Load-Displacement Characteristics in Plantarflexion / Dorsiflexion

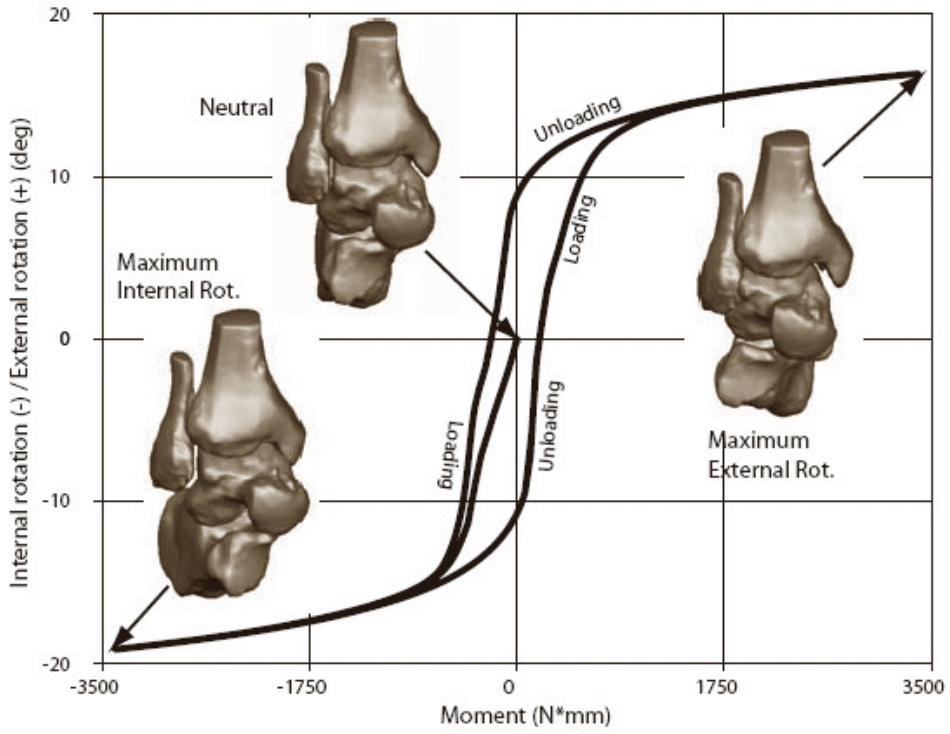

Figure 71. Load-Displacement Characteristics in Internal / External Rotation

Effects of Morphology

The effect of morphology on the variation of passive mechanical properties of the hindfoot in the intact and injured ligament configurations are evaluated on a subject-to-subject basis loaded in inversion. Also, morphological features of these subjects are measured and compared. The sustentaculum tali geometry and the calcaneofibular ligament orientation are altered and their effects on passive mechanical properties measured. Models of the subject-to-subject comparison are those numerical models that were evaluated to their own experimental data in previous sections. The dynamic numerical model and the finite element model are created such that the only variable parameters among subjects are their specific morphology of bone geometry, ligament orientation and length, and cartilage thickness. Ligament and cartilage material properties, boundary conditions, and externally applied loads are constant among subjects. Thus, revealing the effects of morphology.

Subject-to-Subject Passive Mechanics Comparison

The effects of morphology are compared on a subject-to-subject basis using subject specific numerical models to evaluate variations in inversion range of motion of the ankle joint complex and the corresponding talar trochlear contact area and its location.

Intact Ligament Configuration

The variation in inversion range of motion of the ankle joint complex with an intact ligament configuration is compared on a subject-to-subject basis (Figure 72). The

average inversion range of motion is 10.9° with a standard deviation of ±3.6°, and a coefficient of variance of 0.33 (Table 9). The inversion range of motion varies from a minimum of 6.2°, 7R, to a maximum of 16.3°, 6R, a range of 10.1°, or a factor of 2.6 .

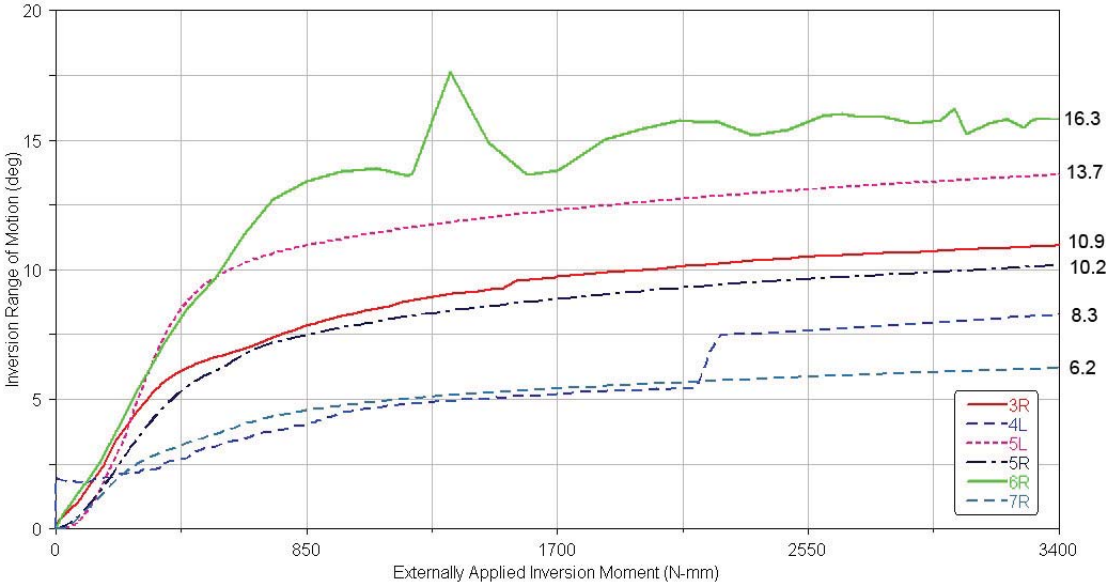

Figure 72. Subject-to-Subject Intact Inversion Range of Motion Comparison

Model 6R experiences a discontinuity in the range of motion during the applied loading at $1300 N \bullet mm$. This is associated with a plantarflexion rotation of the talus as it toggles about a fulcrum on the sustentaculum tali. To a lesser extent, Model 4L experiences a plantarflexion rotation and an internal rotation toggling about the sustentaculum tali.

All six models exhibit contact in Zone A ranging from 11%, of the total contact area, 5R, to 67%, 5L, with an average of 32% and a standard deviation of ±19% (Figure 73, Figure 74, and Figure 75). All six models exhibit contact in Zone B ranging from 12%, 5L, to 70%, 4L, with an average of 29% and a standard deviation of ±21%. No other zones

exhibited contact in all six models. Three models, 5R, 6R, and 7R, exhibit contact in Zone C, 8%, 22%, and 10%, respectively, with an average of 13% and standard deviation of ±8%. All models, except 4L, exhibit contact in Zone D ranging from 7%, 7R, to 35%, 3R, with an average of 20% and a standard deviation of ±10%. Models 3R, 5R, and 7R exhibit contact in Zone E ranging from 7% to 28%, with an average of 20% and a standard deviation of ±11%. Models 5R, 7%, and 7R, 16%, exhibit contact in Zone F, with an average of 12% and standard deviation of ±6%. Models 3R, 1%, and 5R, 2%, exhibit contact in Zone G. Model 5R exhibited contact in Zone H, 3%. Model 5R exhibited contact in Zone I, 1%.

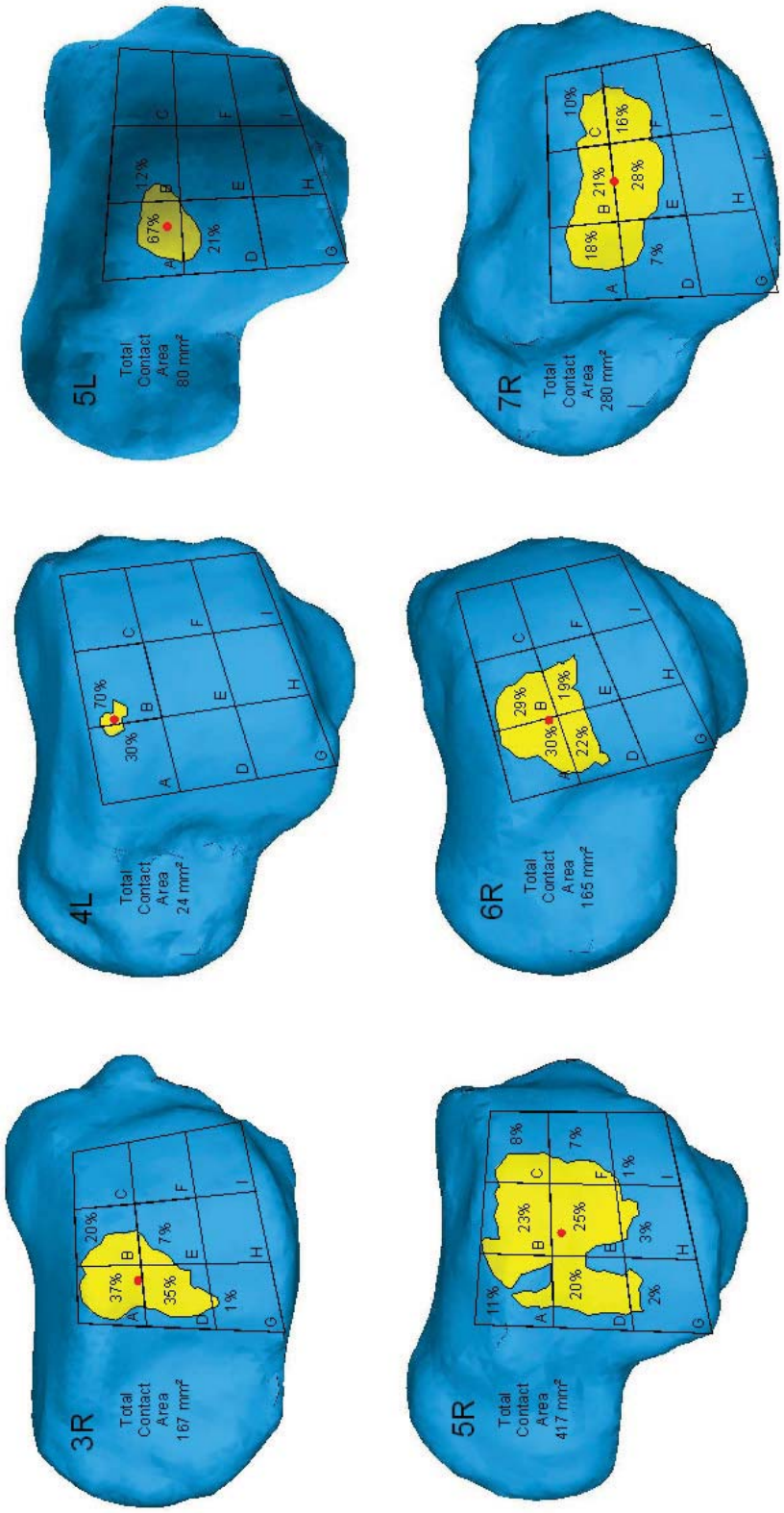

Figure 73. Subject-to-Subject Intact Contact Area and Location Comparison

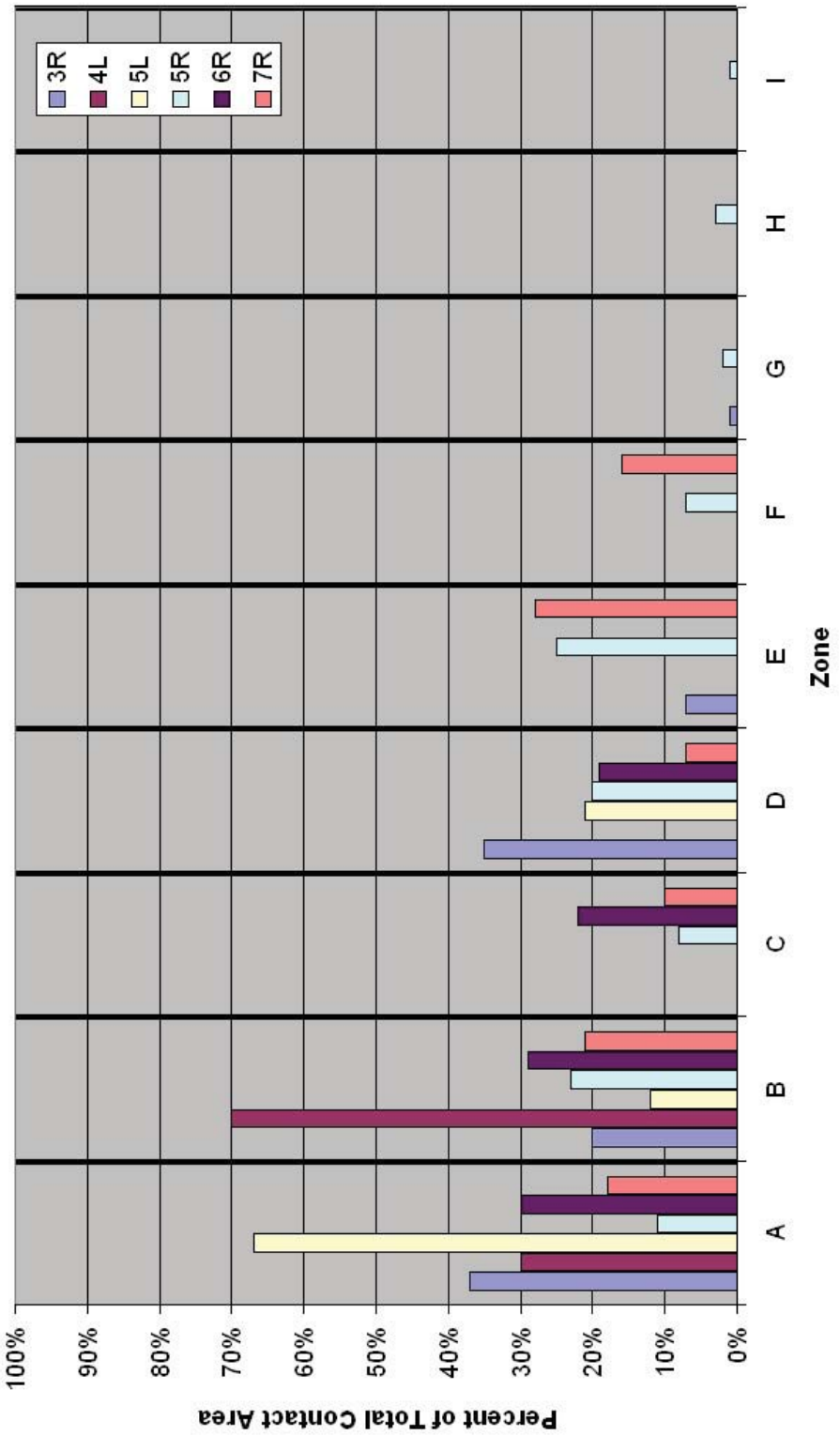

Figure 74. Subject-to-Subject Intact Contact Area and Location Comparison

		Zone								
		A	B	C	D	E	F	G	H	I
Subject	3R	0.37	0.20	0.00	0.35	0.07	0.00	0.01	0.00	0.00
	4L	0.30	0.70	0.00	0.00	0.00	0.00	0.00	0.00	0.00
	5L	0.67	0.12	0.00	0.21	0.00	0.00	0.00	0.00	0.00
	5R	0.11	0.23	0.08	0.20	0.25	0.07	0.02	0.03	0.01
	6R	0.30	0.29	0.22	0.19	0.00	0.00	0.00	0.00	0.00
	7R	0.18	0.21	0.10	0.07	0.28	0.16	0.00	0.00	0.00
	Avg	0.32	0.29	0.13	0.20	0.20	0.12	0.02	0.03	0.01
	Std. Dev.	0.19	0.21	0.08	0.10	0.11	0.06	0.01	--	--

Figure 75. Subject-to-Subject Intact Contact Area and Location Comparison

The contact area centroid location ranges from subject to subject in the anterior-medial Zones A, B, D, and E (Figure 73 and Table 11). The contact area is a minimum of $24mm^2$, 4L, and a maximum of $417mm^2$, 5R, with an average of $189mm^2$ and a standard deviation of $142mm^2$, and a coefficient of variability of 0.75 (Table 11). The contact area shapes are irregular without common features.

Table 11. Subject-to-Subject Intact Contact Area and Centroid Location

Subject	**Zone**	**Area** (mm²)
3R	A	167
4L	B	24
5L	A	80
5R	E	417
6R	A	165
7R	E	280
Avg. ± Std. Dev.		189 ± 142

Injured Ligament Configuration

The variation in inversion range of motion of the ankle joint complex with an injured (sectioned) ligament configuration is compared on a subject-to-subject basis (Figure 76). The average range of motion is 33.7° and a standard deviation 5.6°, and a coefficient of variance of 0.17 (Table 10). The minimum is 27.9°, 4L, and maximum of 40.0°, 3R, with a range of 12.1° among the six subjects.

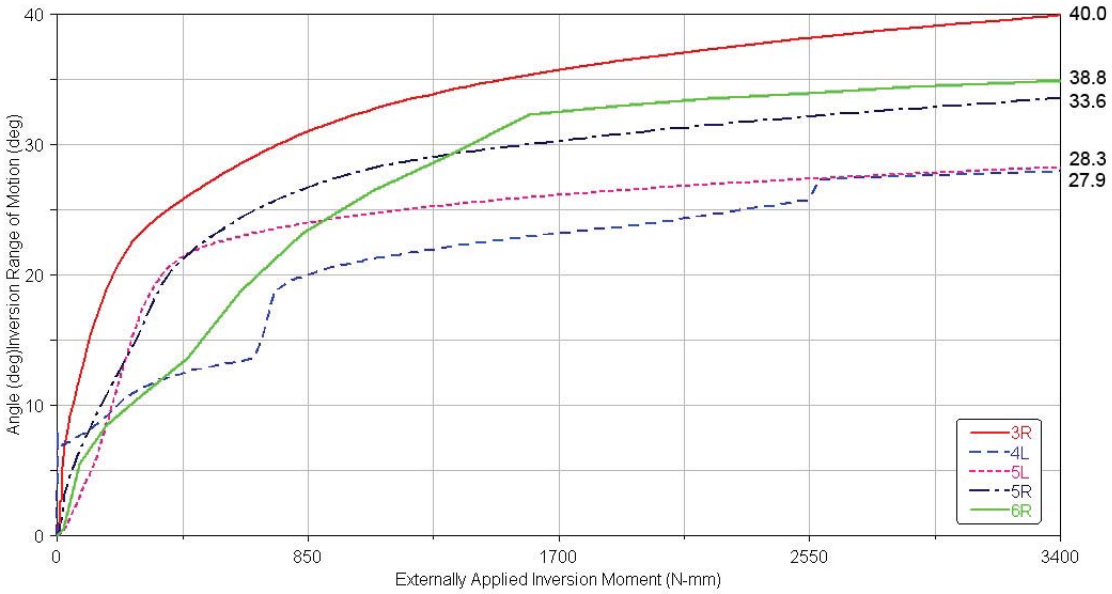

Figure 76. Subject-to-Subject Injured Inversion Range of Motion Comparison

Models 3R and 5L experienced no contact on the talar trochlear surface when loaded in inversion (Figure 77 and Figure 78). Models 4L, 5R, and 6R exhibit contact in the anterior-medial/central corner of the trochlear surface (Zones A, B, D, and E). Models 4L, 5R, and 6R exhibit contact in Zone A ranging from 33%, 6R, to 100%, 5R with an average of 57% and a standard deviation of 37% (Figure 79). Models 4L, 62%, and 6R, 51%, exhibit contact in Zone B. Model 6R exhibited contact in Zones D and E, 11% and 5%, respectively.

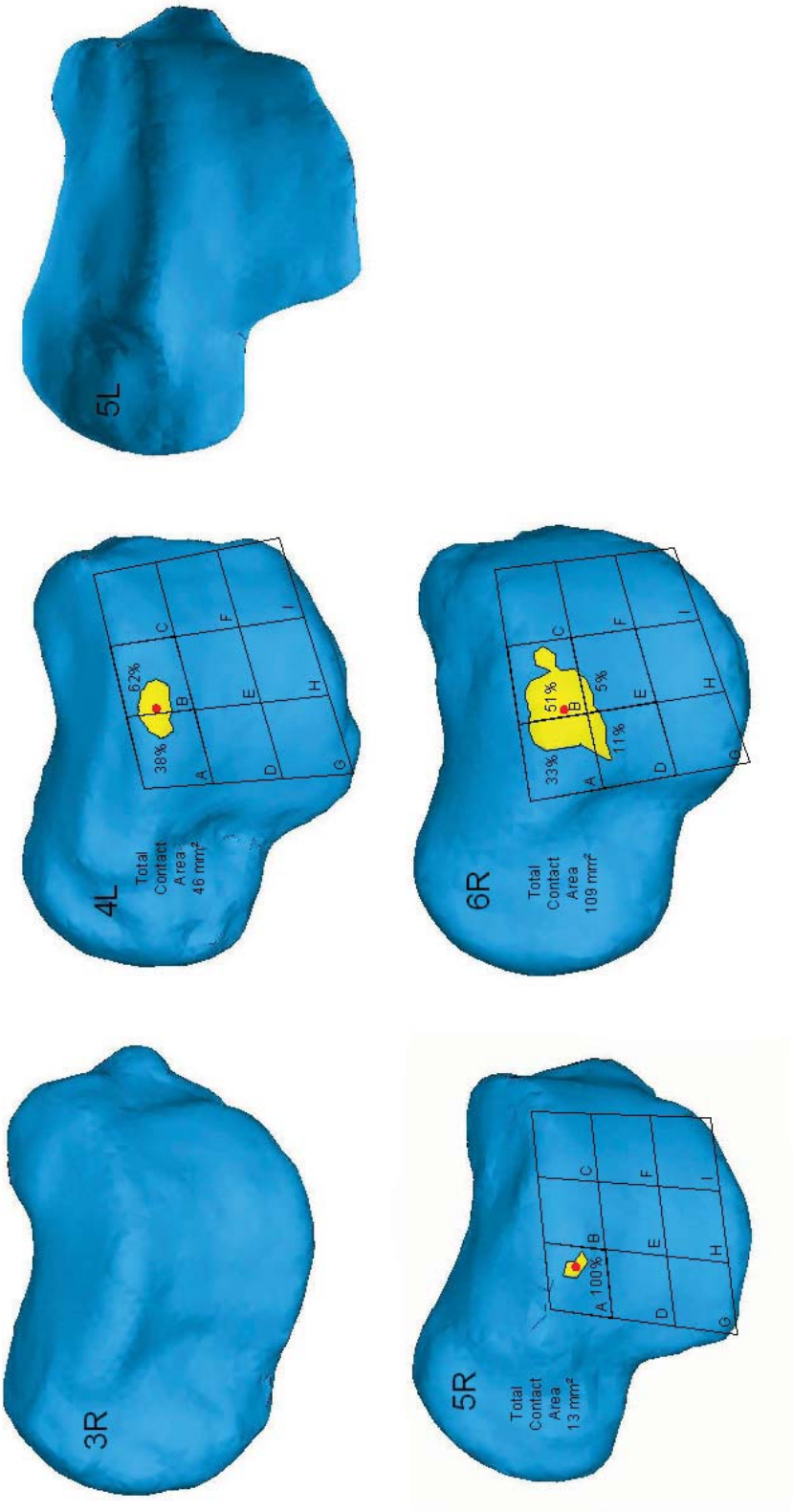

Figure 77. Subject-to-Subject Injured Contact Area and Location Comparison

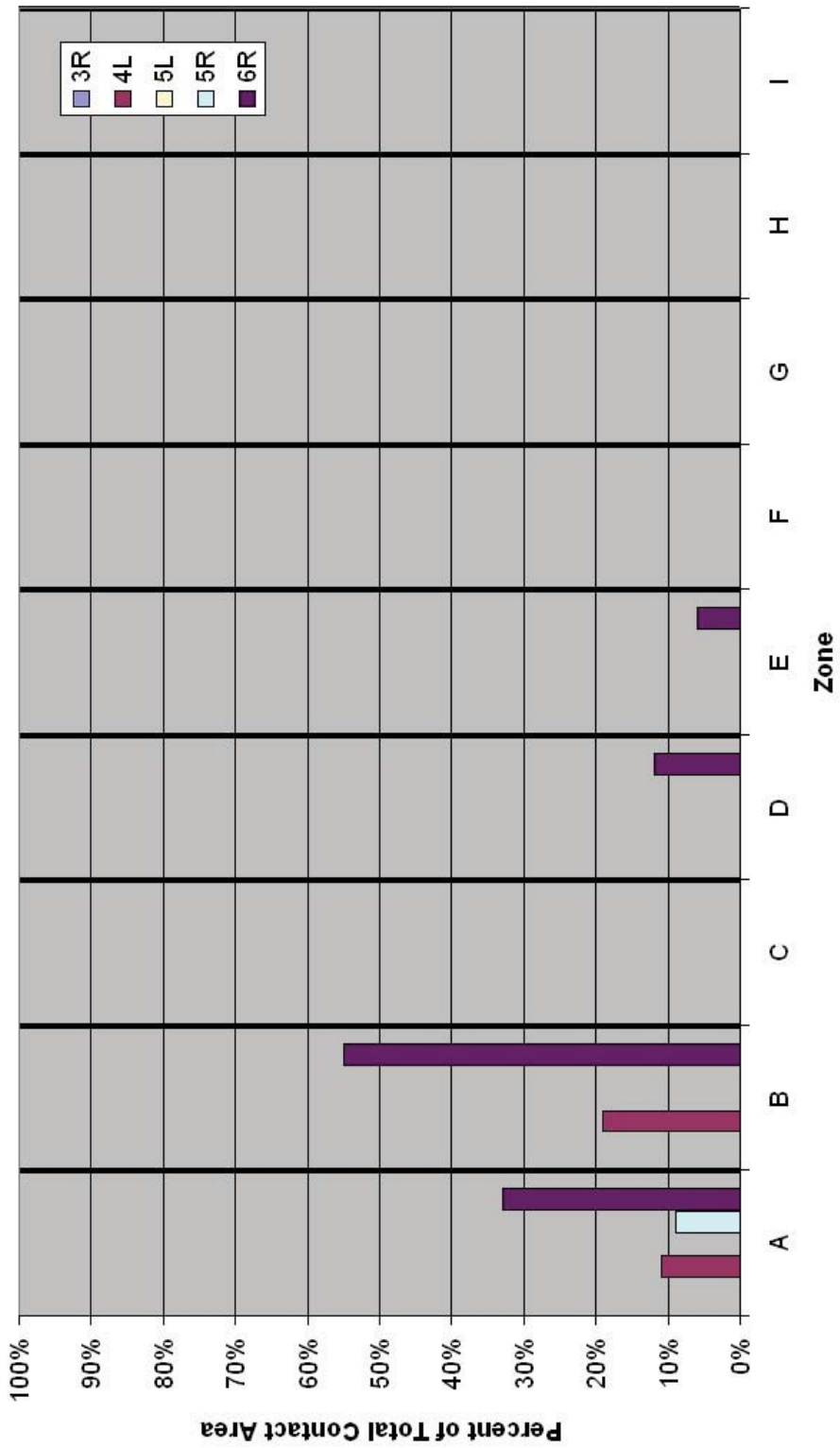

Figure 78. Subject-to-Subject Injured Contact Area and Location Comparison

		Zone								
		A	B	C	D	E	F	G	H	I
Subject	3R	0.00	0.00	0.00	0.00	0.00	0.00	0.00	0.00	0.00
	4L	0.38	0.62	0.00	0.00	0.00	0.00	0.00	0.00	0.00
	5L	0.00	0.00	0.00	0.00	0.00	0.00	0.00	0.00	0.00
	5R	1.00	0.00	0.00	0.00	0.00	0.00	0.00	0.00	0.00
	6R	0.33	0.51	0.00	0.11	0.05	0.00	0.00	0.00	0.00
	Avg	0.57	0.57	0.00	0.11	0.05	0.00	0.00	0.00	0.00
	Std. Dev.	0.37	0.08	0.00	--	--	--	--	--	--

Figure 79. Subject-to-Subject Injured Contact Area and Location Comparison

The contact area centroid location ranges from subject to subject in the anterior-medial Zones A and B (Figure 77 and Table 12). The contact area is a minimum of $13mm^2$, 5R, and a maximum of $109mm^2$, 6R, with an average of $56mm^2$ and a standard deviation of $49mm^2$, and a coefficient of variability of 0.88 (Table 12). The contact area shapes are irregular without common features.

Table 12. Subject-to-Subject Injured Contact Area and Centroid Location

Subject	**Zone**	**Area** (mm^2)
3R	No Contact	No Contact
4L	B	46
5L	No Contact	No Contact
5R	A	13
6R	B	109
Avg. ± Std. Dev.		56 ± 49

Subject-to-Subject Morphological Variations

Morphological variation of features, such as calcaneal bone dimensions, calcaneal articular facet configuration, sustentaculum tali inclination, sustentaculum tali dimensions, calcaneofibular ligament orientation, calcaneus inclination angle, and talar trochlear cartilage thickness distribution, of the six subjects are compared.

Calcaneal Bone Dimensions

The length, width, and height of the six model calcanei are measured using boney landmarks previously identified [1] (Figure 12). The coefficient of variance in the length, width, and height are 0.04, 0.08, and 0.05, respectively (Table 13).

Table 13. Calcaneal Bone Dimensions

Model	**Length, L,** mm	**Width, W,** mm	**Height, H,** mm
3R	87.3	40.4	43.7
4L	87.9	47.3	46.3
5L	81.3	43.6	42.9
5R	80.0	42.6	43.8
6R	84.6	37.9	43.2
7R	88.4	42.0	39.6
Avg ± Std. Dev.	84.9 ± 3.6	42.3 ± 3.2	43.3 ± 2.2

Calcaneal Articular Facet Configuration

Variations in the articular facets of the calcaneus are classified into three types: *A* (all facets are distinct and separate), *B* (the anterior and middle facets are confluent), and *C* (all facets are united into a single surface) [8]. Using this classification 3R, 5L, 5R, and 6R are of Type *A*; 4L and 7R are of Type *B*. Variations of calcaneal articulating facet configuration are inspected using the three dimensional magnetic resonance image reconstruction of the hindfoot (Figure 80). A magnetic resonance image view plane is oriented in the three dimensional reconstruction, passing through both the anterior and middle facets. The magnetic resonance image is then viewed corresponding to the plane's orientation.

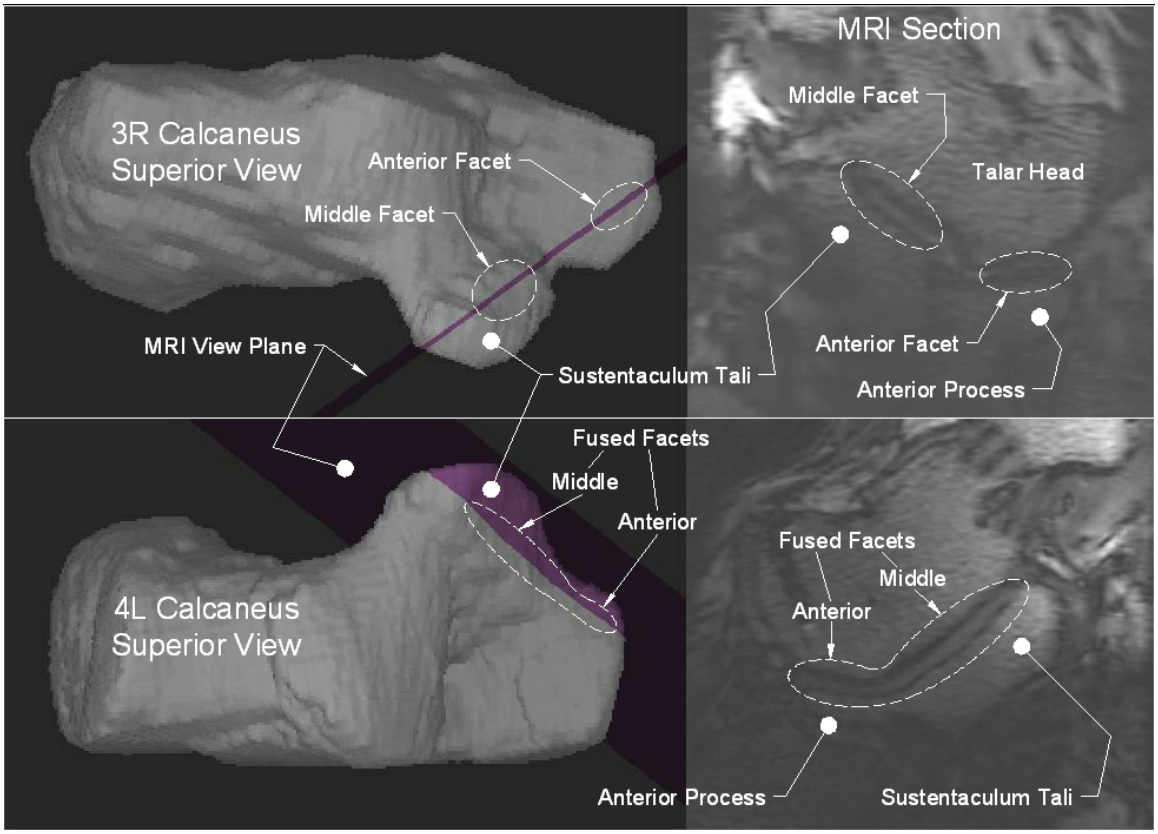

Figure 80. Calcaneal Articular Facet Configuration

Model 7R's broad posterior sustentacular boney extension onto the medial side of the calcaneal body gives support to a posterior articular facet extension (Figure 81). The posterior extension spans approximately $8mm$ onto the boney extension. However, this facet does not blend with the middle, nor is 7R classified as Type C.

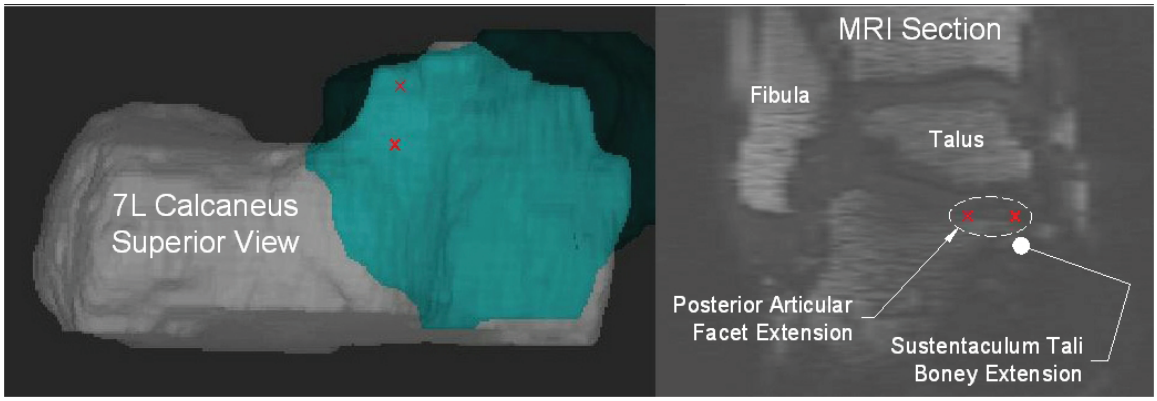

Figure 81. Model 7R Posterior Articular Facet Extension

Sustentaculum Tali Inclination

The inclination of the sustentaculum tali is measured by visually identifying bone landmarks on the sustentaculum tali and the inferior surface on a two dimensional projection of the medial calcaneal aspect (Figure 17). Line AO is drawn through the mid-thickness of the anterior and posterior borders of the sustentaculum tali. Line BO is drawn collinear to the inferior surface on the anterior and middle thirds of the calcaneal body, not including the lateral and medial tuberosity (Figure 11). Variations in inclination of the sustentaculum tali among the six subjects range from 40° to 50° with an average of 46.3° and a standard deviation of ± 3.9° (Figure 82). The coefficient of variance is 0.08.

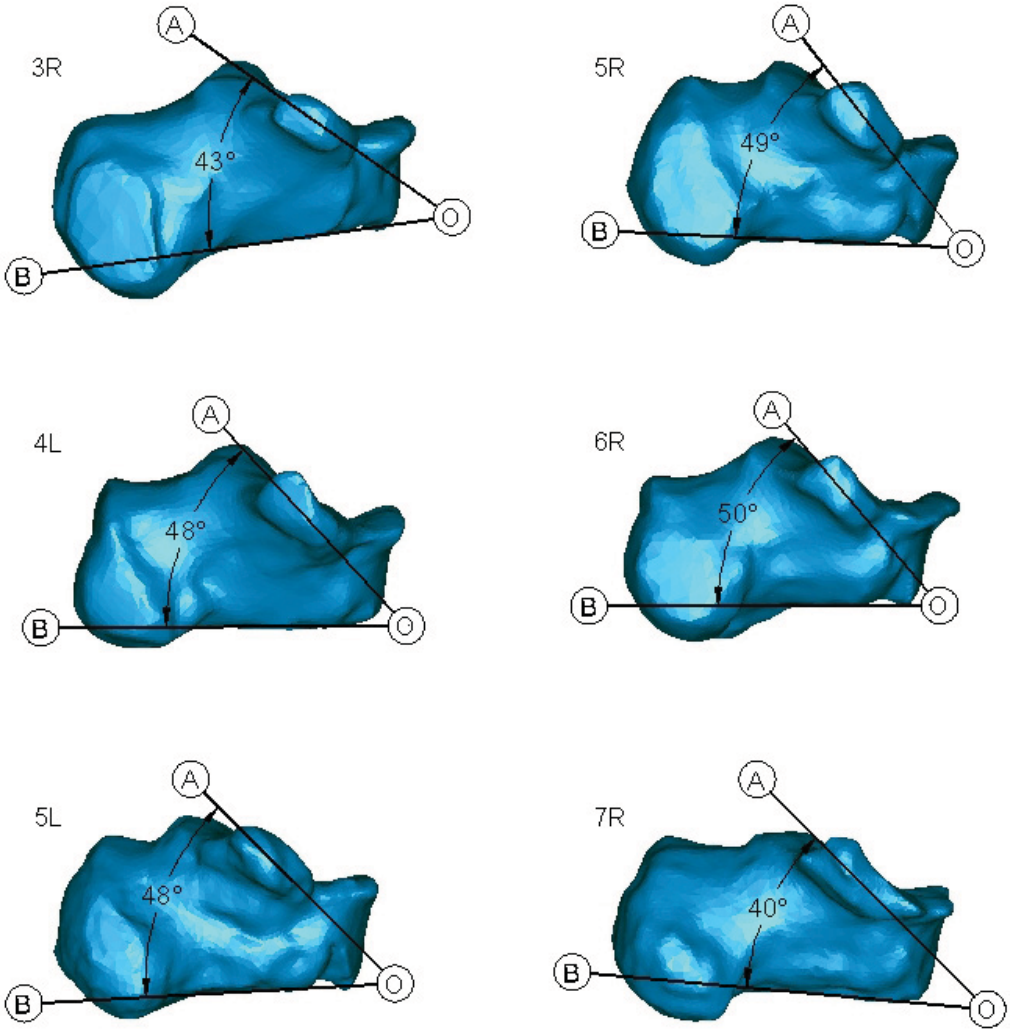

Figure 82. Inclination Angle of Sustentaculum Tali

Sustentaculum Tali Dimensions and Classification

The sustentaculum tali width is measured by visually identifying the medial border of the calcaneus and measuring perpendicular to it, the farthest distance on the sustentaculum on a two dimensional projection of the superior aspect (Figure 83). The medial border is identified, on the anterior side, by a notch located where the sustentaculum tali ends onto the medial border at the middle and anterior articular facets and, on the posterior side, where the sustentaculum tali attaches itself at the posterior articulating facet. The

average width of the sustentaculum is 16.2*mm* with a standard deviation of ±1.5*mm*. The coefficient of variance is 0.09.

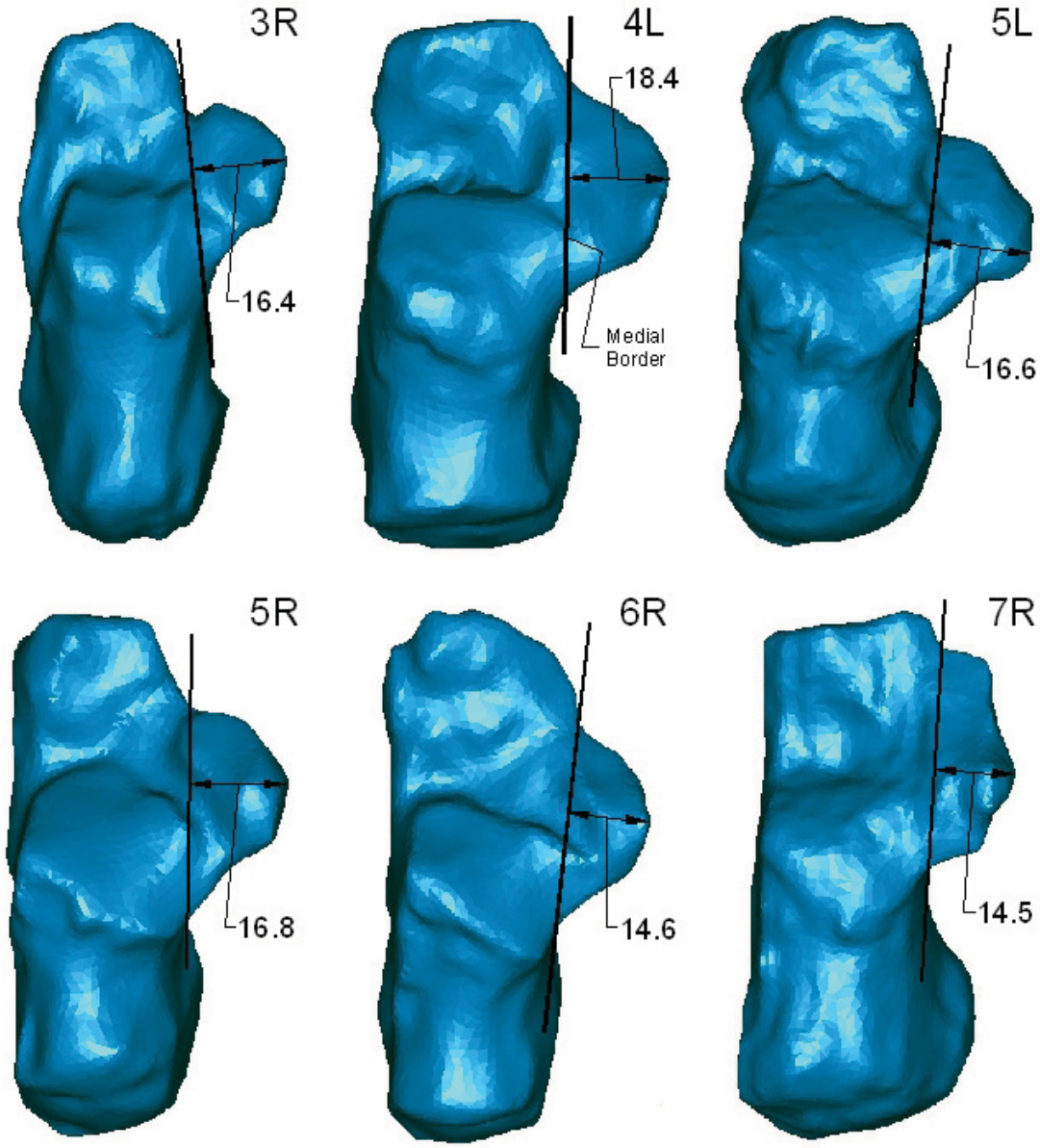

Figure 83. Sustentaculum Tali Width
Dimensions in mm.

Calcanei 3R, 5L, 5R, and 6R have a distinct notch present where the sustentaculum tali ends onto the medial border at the middle and anterior articular facets and may be classified as a short sustentaculum (Table 14). The sustentaculum tali of 4L and 7R are continuous with the medial border and may be classified as long. A long sustentaculum tali is associated with anterior and middle articular facet fusion.

Table 14. Sustentaculum Tali Classifications

Subject	Sustentaculum Tali Width / Total Width Ratio	Competent / Incompetent Classification	Long / Short Classification
3R	0.41	Competent	Short
4L	0.39	Competent	Long
5L	0.38	Competent	Short
5R	0.39	Competent	Short
6R	0.39	Competent	Short
7R	0.35	Competent	Long

The sustentaculum tali width to calcaneus width ratio may be used to classify competency in regards to supportive function of the talar head. From literature, the ratio is on average, 0.33 with a minimum of 0.23 and a maximum of 0.47 [1]. A sustentaculum tali falling into the lower range may be classified as incompetent. Taking the reported average as the distinction between competent and incompetent, all subjects have ratios above the average, thus classified as competent (Table 14).

Calcaneofibular Ligament Orientation

The calcaneofibular ligament orientation is vertical when it is parallel to the long axis of the tibia and horizontal when near perpendicular (Figure 22). The calcaneofibular

ligament orientation of the six subjects range from 6°, 7R, to 46°, 5L, and an average of 34.5° and standard deviation of ±14.7° (Figure 84) and a coefficient of variance of 0.43. Additionally, the calcaneofibular ligament length ranges from 10.1*mm*, 7R, to 27.0*mm*, 6R, and an average of 20.1*mm* and standard deviation of ±6.5*mm* and coefficient of variance of 0.33 (Figure 84).

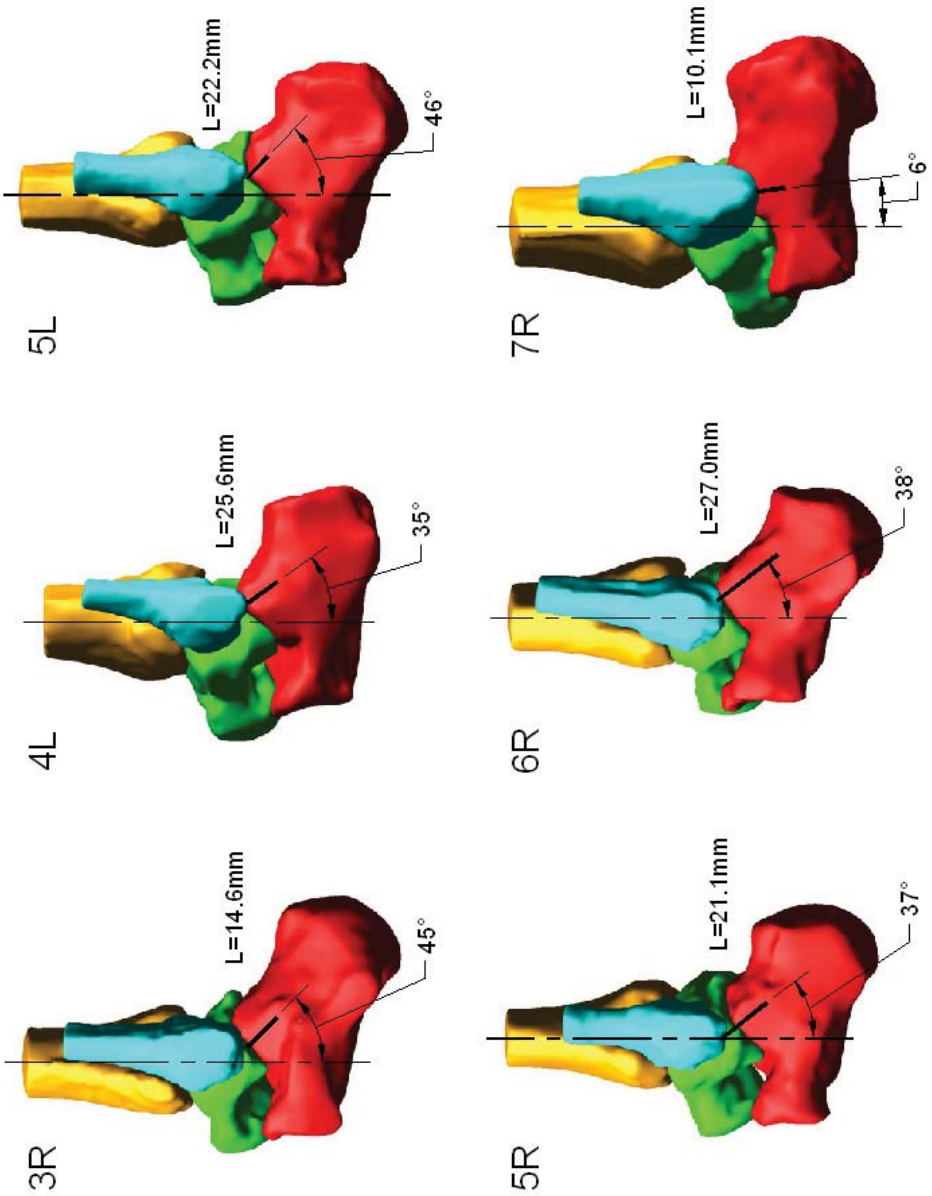

Figure 84. Calcaneofibular Ligament Orientation

Talar Trochlear Cartilage Thickness Distribution

The talar trochlear cartilage thickness is measured from the bone surface of the talus to the cartilage surface. The average cartilage thickness is the average of nine locations. Cartilage thickness is measured using the three dimensional magnetic resonance image reconstruction of the hindfoot and the re-slicing technique (Appendix A) for locating ligament insertion sites. A sagittal plane is located at the medial, central, and lateral locations. In each location, measurements are taken at the anterior, middle, and posterior locations. For graphical orientation, the cartilage thickness is projected onto the talar trochlear surface and described within the contact area zones (Figure 85).

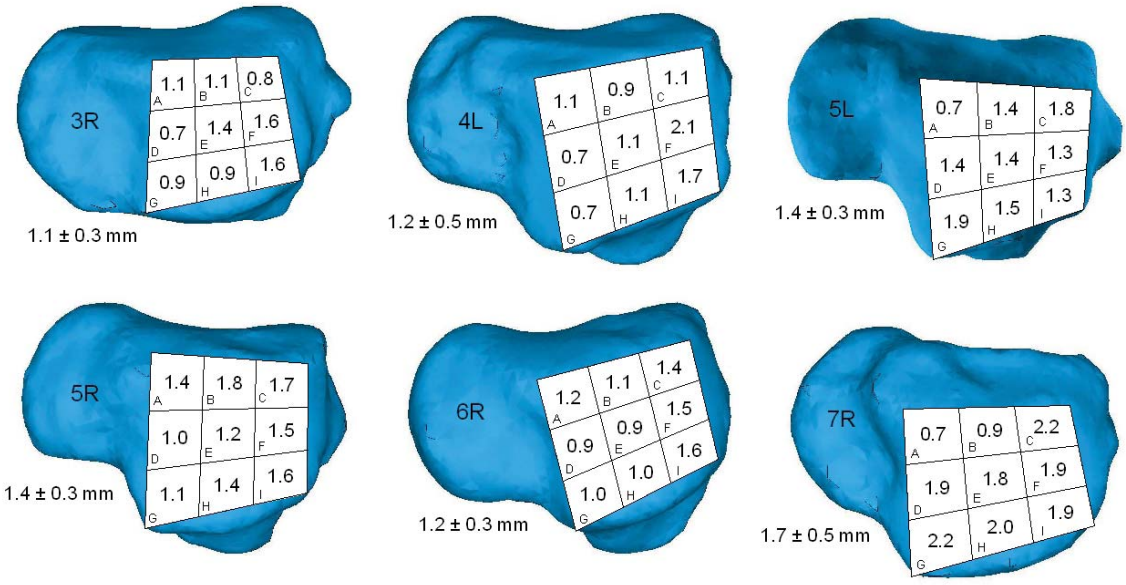

Figure 85. Talar Trochlear Cartilage Thickness Distribution

Functional Morphology

Local morphological features, such as the sustentaculum tali geometry and calcaneofibular ligament orientation, are altered and their effect on inversion range of motion of the ankle joint complex is observed.

Sustentaculum Tali Geometry

The functional morphology of the sustentaculum tali during inversion motion is evaluated by altering its geometry, therefore, altering its supportive functionality to the anterior and middle portions of the talar head during inversion loading. The calcaneus of Model 7R was chosen due to its large fused middle and anterior articulating facet providing a firm supporting structure for the middle and anterior articulating facets of the talus (Figure 86). Model 7R has the lowest inversion range of motion in the intact ligament configuration of all subjects. This sustentaculum tali is classified as long and its anterior and middle articular facets are fused (Table 14). Additionally, the posterior articular facet supports a medial-side extension (Figure 81).

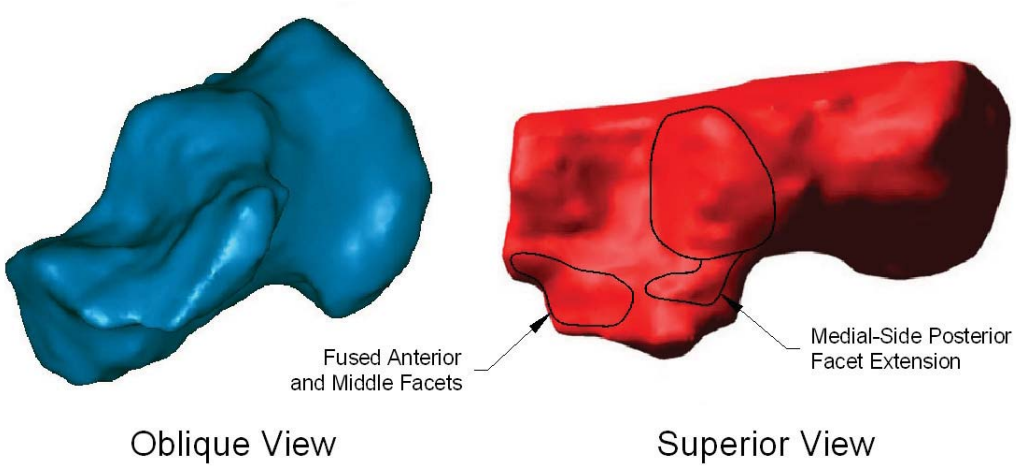

Figure 86. Unaltered Sustentaculum Tali

Alteration #1 removed boney material up to approximately 12*mm* of the fused anterior and middle facet supporting structure (Figure 87 and Figure 88). Alteration #2 and Alteration #3 progressively lowered the posterior end of the middle facet and the medial-side posterior facet extension from approximately 6*mm* to 9*mm*. Alteration #4 completely obliterated the sustentaculum tali and the medial-side posterior articular facet extension.

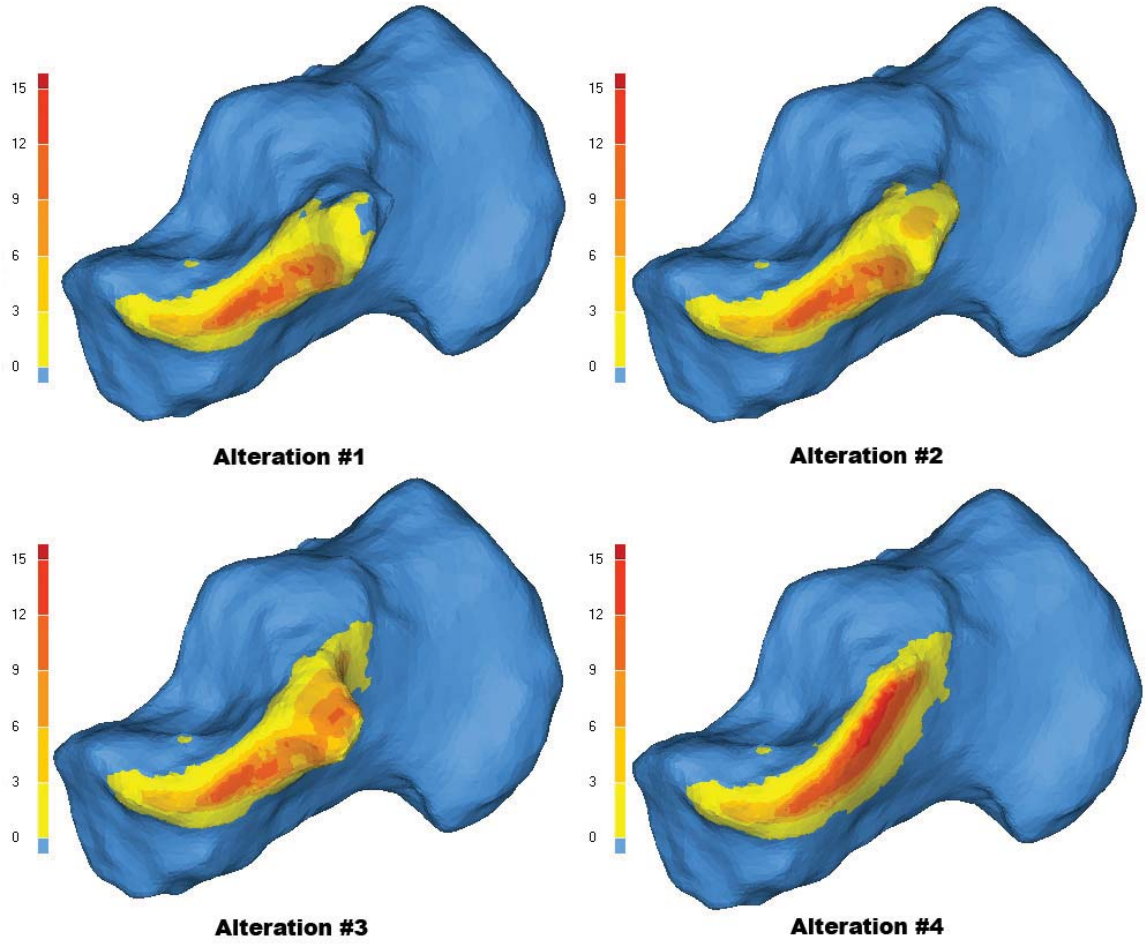

Figure 87. Sustentaculum Tali Alterations - Deviations from Unaltered Geometry
Altered geometry shown with projected contour of surface deviations from the unaltered geometry. Dimensions in mm.

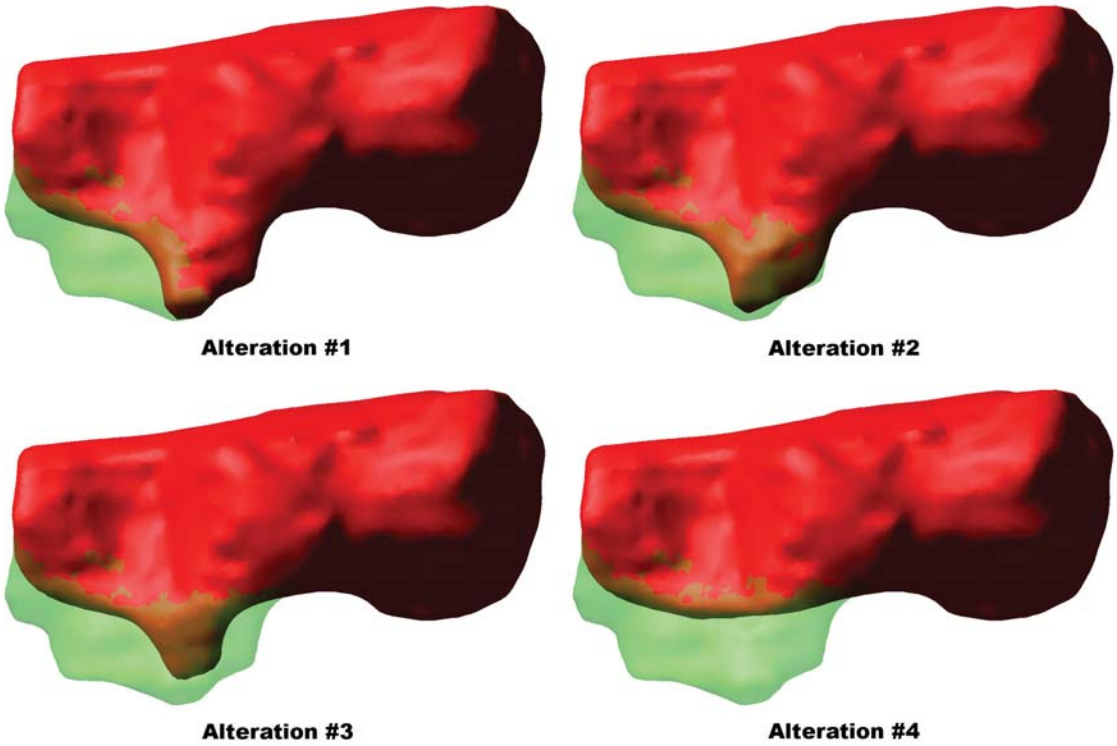

Figure 88. Sustentaculum Tali Alterations - Superior View
Unaltered calcaneus outlined in translucent green, altered calcaneus red. Altered bone shown below unaltered outline indicates a lower elevation.

Alterations #1 through #4 of the sustentaculum tali successively alter the supportive function of the middle articular facet on the talus (Figure 89). Attention is drawn to the variation in congruency of the sustentaculum tali of the calcaneus to the canalis tarsi of the talus.

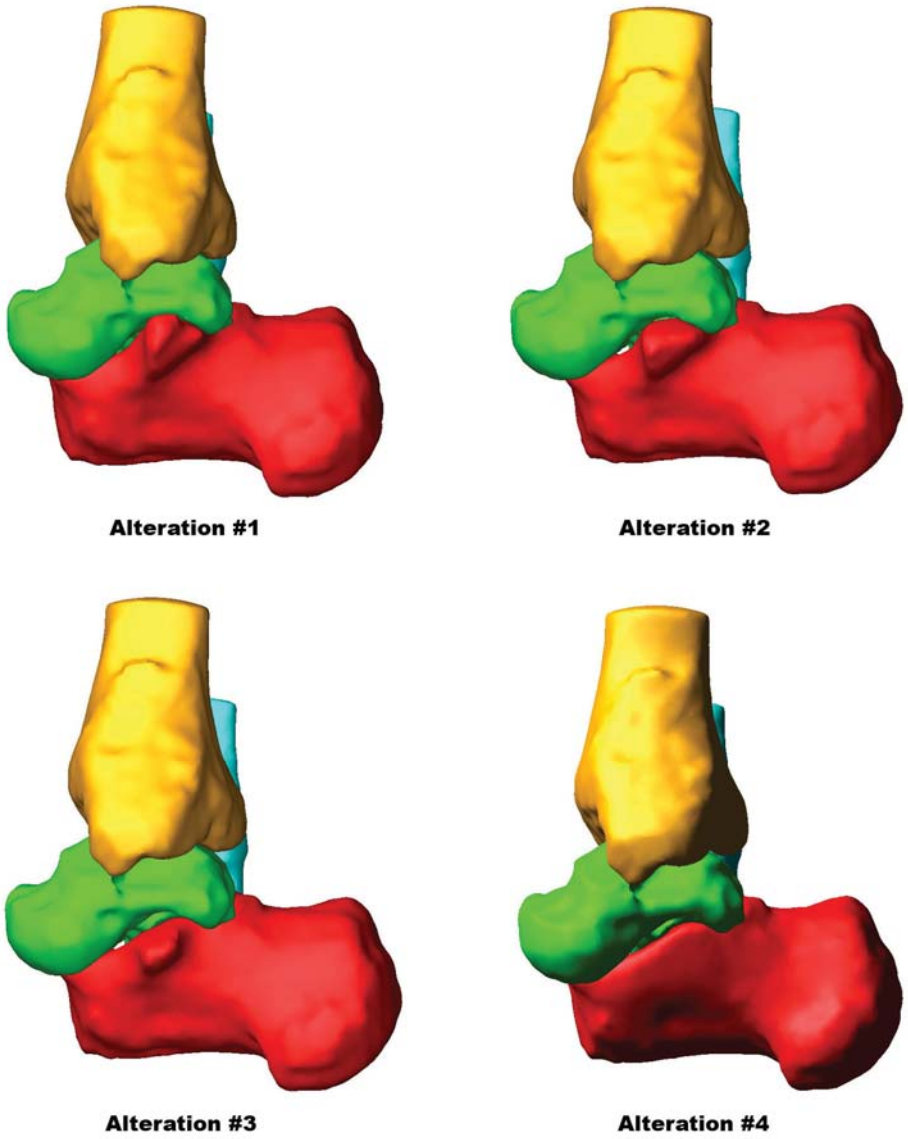

Figure 89. Sustentaculum Tali Alterations - Hindfoot Medial View

The rigid body interpenetrated contact areas between the calcaneus and talus for the unaltered configuration loaded to the maximum externally applied inversion moment are located on the anterior-middle fused facet, a separate, distinct area on the middle facet, and a narrowly connected area spanning the posterior facet and the posterior facet extension (Figure 90).

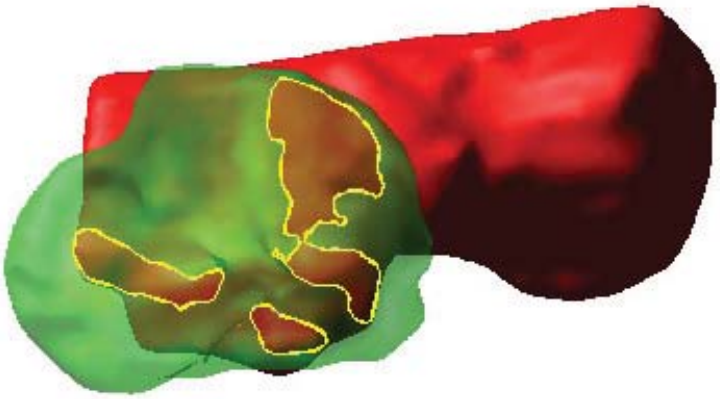

Figure 90. Unaltered Sustentaculum Tali - Contact Area Through Translucent Talus
Superior view. Calcaneus: red, talus: translucent green, contact area: yellow outline

Alteration #1: Removed the boney platform shaped structure supporting the fused anterior and middle articular facets (Figure 88). This has the effect of removing the anterior articular facet support of the talus. The talus remains supported deep in the canalis tarsi on the posterior end of the middle articulating facet and on the medial side of the posterior articulating facet extension (Figure 89).

Alteration #2: Removed support of the posterior end of the middle articulating facet of the talus by lowering the elevation of the middle articulating facet (Figure 87 and Figure 88). This is shown as the red surface below the translucent green surface. The loss of support deep in the canalis tarsi is visible. An unobstructed line of sight through the canalis tarsi and sinus tarsi is now present (Figure 89). The talus is supported on the medial-side posterior articular facet extension.

Alteration #3: Removed the medial-side posterior articulating facet extension by lowering its articulating surface elevation (Figure 87 and Figure 88).

Alteration #4: Completely obliterated the sustentaculum tali (Figure 87). The posterior articular facet is now the primary supporting facet.

Alteration #1 increased the inversion range of motion from unaltered, 6.2°, to 6.7° (Figure 91). Alteration #2 increased the inversion range of motion to 11.3°. Alteration #3 increased the inversion range of motion to 14.1°. Alteration #4 had no more effect than Alteration #3.

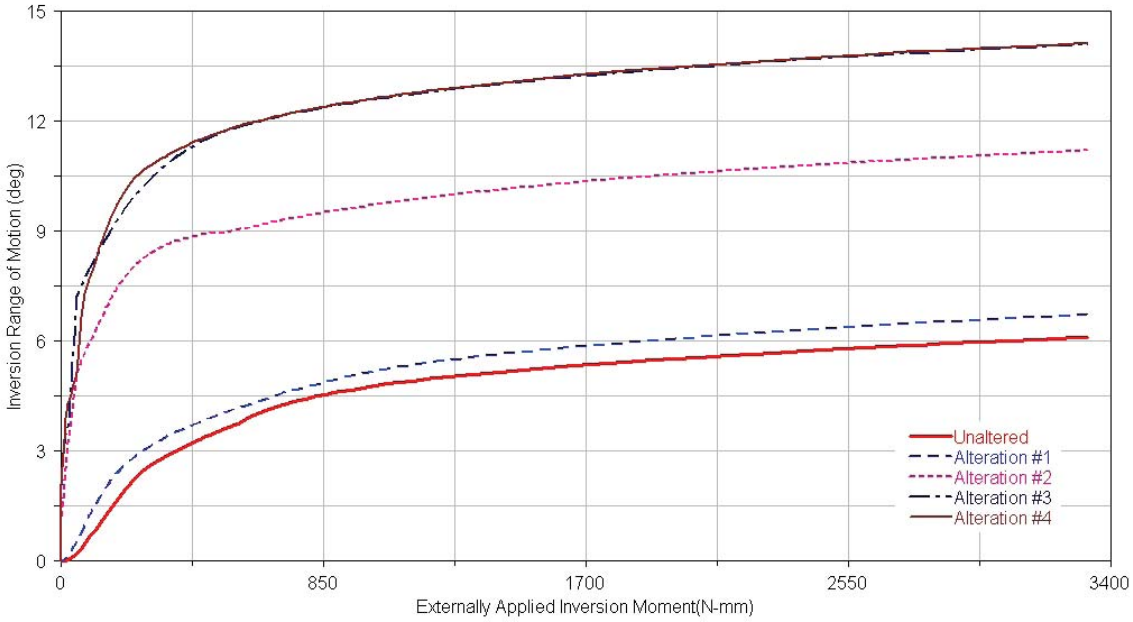

Figure 91. Altered Sustentaculum Tali Inversion Range of Motion

Comparing the unaltered contact areas (Figure 90) to the contact areas of Alteration #1 (Figure 92), the anterior articulating facet no longer supports the head of the talus. Alteration #2 lowered the surface of the sustentaculum tali and permitted it to move deeper into the canalis tarsi (Figure 89), allowing the calcaneus to rotate about the contact area on the medial-side posterior articulating facet extension. Alteration #3 shifts the contacting areas to the posterior articular facet and the sustentaculum tali no longer supports the talus. Alteration #4 had no more effect than Alteration #3.

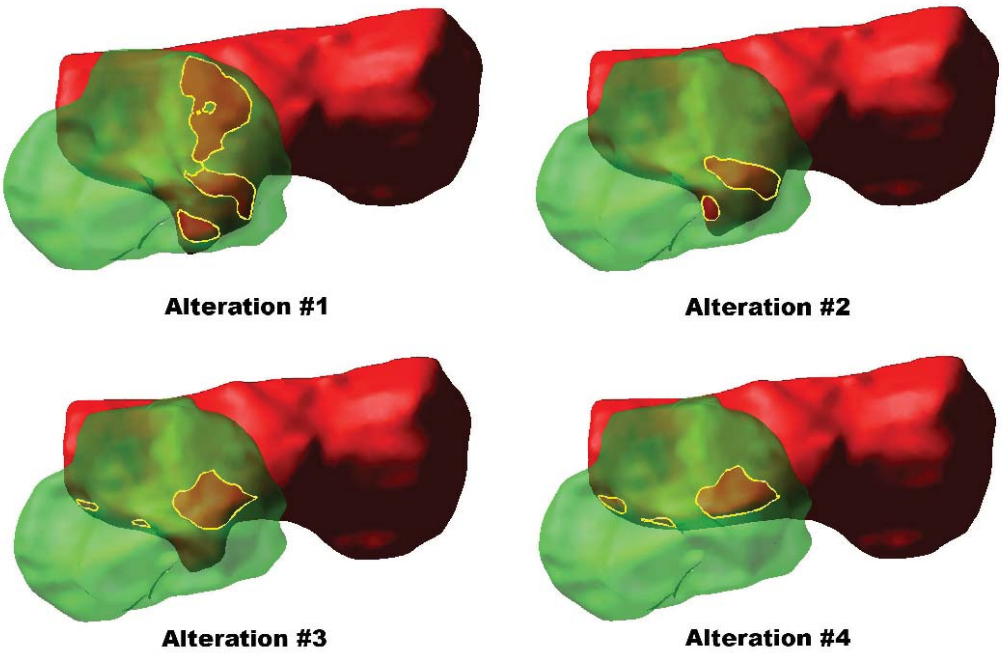

Figure 92. Sustentaculum Tali Alterations - Contact Area

Calcaneofibular Ligament Orientation

The functional morphology of the calcaneofibular ligament orientation during inversion loading is altered and the effect it has on inversion range of motion is evaluated (Figure 93). Model 5L (Figure 47 and Figure 84) is selected for this evaluation due to its broad lateral-posterior border making for physiological calcaneofibular ligament insertion locations. Other subjects either had a large calcaneal pitch angle (Figure 13) removing possible horizontal insertions, or the superior surface of the posterior third of the calcaneal body declined rapidly behind the posterior articulating facet (Figure 11).

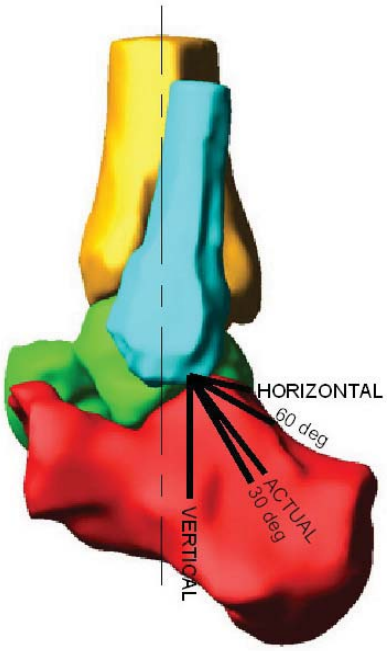

Figure 93. Alteration of Calcaneofibular Ligament Orientation

The orientation of the calcaneofibular ligament of the selected subject is near mid-range, 46°, providing a reference orientation sensitive to changes in orientation on either side. The broad posterior-lateral calcaneal aspect provides ample ligament insertion locations while maintaining constant ligament length.

The inversion range of motion increases progressively from a vertical to horizontal ligament orientation (Figure 94). The inversion range of motion decreases 30% from 17.4° in the actual orientation to 12.2° in the vertical orientation; and increases 14% from the actual orientation to 19.9° in the horizontal orientation. The inversion range of motion decreases 7% from the actual orientation to 16.1° in the 30 degree position and increases 12% from the actual orientation to 19.5° in the 60 degree orientation. The range of inversion motion from the vertical orientation to the horizontal orientation is 7.7°.

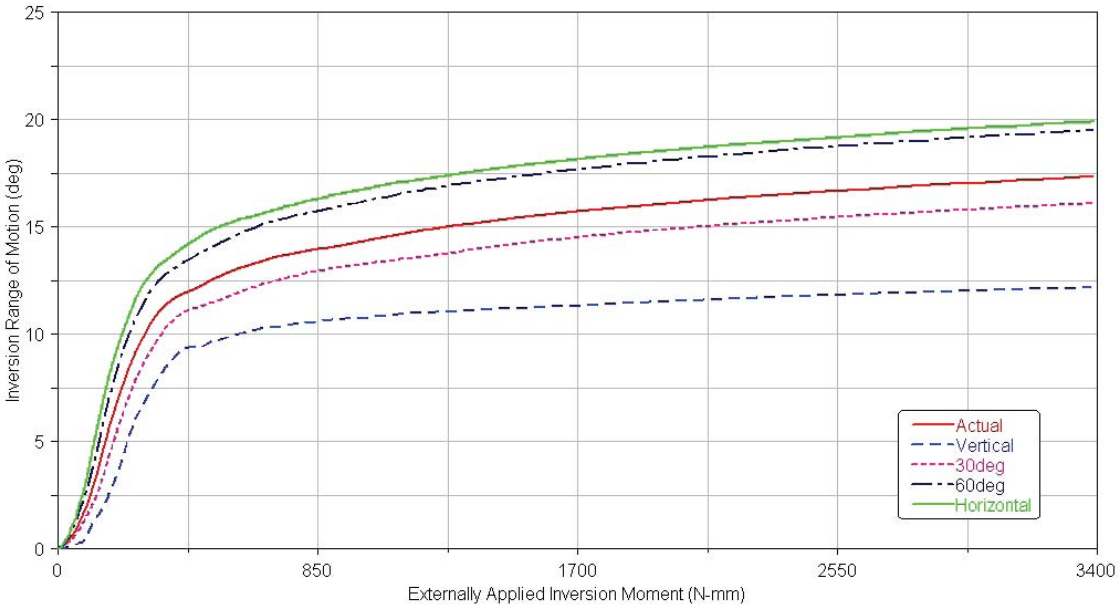

Figure 94. Ligament Orientation Effect on Inversion Range of Motion

The calcaneofibular ligament force increases from $80N$ in the actual orientation to $106N$ in the vertical orientation and decreases to $72N$ in the horizontal orientation.

Chapter 5: Discussion

This chapter discusses the results of the model development, model evaluation, and effect of morphology on passive mechanical properties. Model development discusses the subject specific modeling procedure's ability to capture a wide range of mechanical phenomenon. The model evaluation discusses the ability of the model to predict experimental evaluation results. The effect of morphology discusses the comparisons of the subject-to-subject passive mechanical properties and morphological variations among the subjects and the functional morphology of the sustentaculum tali and calcaneofibular ligament during inversion loadings.

Model Development

Subject specific morphology of the bones, articular surfaces, and ligaments is captured by the model development. The three dimensional computerized representations of the bones are generated from subject specific magnetic resonance image data. Ligament insertion locations are identified from the three dimensional reconstruction of the magnetic resonance image data. Thus, subject specific morphological variations are incorporated into the numerical models.

Rigid Body Dynamic Model

The three dimensional subject specific rigid body dynamic models of the human hindfoot developed for six subjects have the ability to simulate a variety of externally applied

static and cyclic loadings and boundary conditions mimicking experimental setup. It captures load-displacement characteristics, hysteresis, ligament recruitment, and load transmission through articular contact (Figure 47).

Load-displacement characteristics exhibit initial high flexibility followed by an increase in stiffness (Figure 48 and Figure 49). Hysteresis is present in the primary range of motion across the ankle joint complex during cyclic loading of plantarflexion / dorsiflexion, inversion / eversion, and internal / external rotation [29, 70, 71]. Viscoelastic ligament behavior manifests itself initially as highly flexible, followed by an exponentially increasing stiffness [51] (Figure 50). Contact force increases exponentially with increasing penetration depth (Equation 7) [54] (Figure 51).

Finite Element Model

The finite element model is used to describe the contact area and its location on the talar trochlear surface by removing the rigid body penetration of the dynamic solution. The calcaneus and talus are located and oriented as determined from the rigid body simulation. All external and internal forces on the hindfoot are balanced by dynamic equilibrium. Therefore, the bones of the hindfoot can be fixed against translations and rotations. This allows for a static nonlinear, initial penetration, contact solution.

Changes to the modulus of elasticity of the linear elastic constitutive equation had little effect on the contact area. A variation of 10^4 in modulus of elasticity varied the contact area by 16%. Contact area may be more dependent on morphology than material

properties. Morphological features, namely the anterior-posterior and medial-lateral talar trochlear curvatures, may be responsible for the pronounced anterior-posterior shortening of the contact area and slight shortening medial-lateral (Figure 56).

Residual contact penetration in the finite element solution is less than $0.01mm$. The residual penetration is necessary for the contact algorithm. However, $0.01mm$ of residual penetration is approximately 0.4% of the minimum average thickness of the talar trochlear cartilage layer.

The polygon discretization for the finite element model is less refined than the rigid body dynamic model to reduce computational effort. However, reducing the number of surface elements by half altered the morphology of the surface in various local regions by $0.04mm$, approximately 4% of the average cartilage thickness (Figure 55).

Model Evaluation

The six patient specific hindfoot models are evaluated on a one-to-one model-to-experiment basis and an average model-to-experiment basis for their ability to capture passive mechanical properties. The one-to-one model-to-experiment basis consists of comparing the inversion range of motion across the ankle joint complex and talar trochlear contact area and its location against the experimental data for that particular subject for the intact and injured (sectioned) ligament configurations. The average model-to-experiment basis consists of comparing the average primary and coupled range of motion in plantarflexion / dorsiflexion, inversion / eversion, and internal / external rotation predicted by the six models to the average of fifteen cadaveric specimens in the intact ligament configuration. The six sets of experimental data used in the one-to-one model-to-experiment evaluation are not included in the specimens of the average model-to-experiment basis.

The experimental reconstruction of the magnetic resonance images into a three dimensional assembly of the bones of the hindfoot is performed without additional processing of the bones. Therefore, the maximum deviation of the step-like layered structure from a naturally smooth articulating surface is within one voxel size ($0.35mm$ x $0.35mm$ x $0.35mm$). The average cartilage pair thickness of the tibiotalar joint is $2.6mm$ with a minimum of $2.3mm$, 4L and 6R, and a maximum of $3.0mm$, 7R. Maximum deviations at the tibial and talar articular surfaces could be up to $0.70mm$. This is 30% of the thinnest average tibiotalar cartilage thickness. This may effect the calculation of contact area and its location.

One-to-One Model-to-Experiment Comparison

The one-to-one model-to-experiment evaluation compares the inversion range of motion and contact area and location in the intact and injured ligament configurations of different specimens of this study to evaluate modeling procedure's ability to recreate the highly variable mechanics of the human hindfoot. This is done by creating six patient specific sets of model and experimental data.

Intact Ligament Configuration

The inversion range of motion comparison between the intact ligament configuration model and the experiment results for 3R, 5L, 6R, and 7R are within a 25% difference (Table 9). Of these, 7R is within a 3% difference and 3R was within a 8% difference. Models 4L and 5L are 40% and 76%, respectively, different from experiment. The average model and experimental results are 10.9° ± 3.6° and 11.8° ± 5.8°, respectively.

All subjects show contact on the talar trochlear on the medial side, mostly concentrated on the anterior portion, Zones A and B (Figure 57 through Figure 62). This is consistent with experimental findings under inversion loadings even under a 490 N axial compressive load [72].

The average percent difference between model and experiment of contact area in each zone for all subjects is 40%. Differences in percent contact area coverage between model and experiment may be due to assumptions. The model prediction neglects the cartilage geometry. However the shape of the bone surface under the articular cartilage surface is

similar with gradually changing differences due to variations in cartilage thickness. The bone surfaces, now represented as a smaller articulating surface, are translated together closing the inter-cortical gap, bringing together the less congruent surfaces.

Injured Ligament Configuration

The inversion range of motion comparison between the injured ligament configuration model and the experiment results for 4L, 5L, and 6R are within a 27% difference (Table 10). Models 3R and 5R both predict approximately a 60% difference from experimental results. The average model inversion range of motion over predicts the average experimental range of motion by 39%, $33.7 \pm 5.6°$ and $24.2 \pm 3.9°$, respectively. Each model over predicts the inversion range of motion, ranging from $5.4°$ to $15.8°$.

The over prediction may partially be explained by the exclusion of cartilage geometry. The cartilage on the constraining surfaces of the ankle mortise (on the lateral and medial malleoli) are, on average, measured as $0.95 \pm 0.17 mm$ and $0.97 \pm 0.16 mm$ (Table 1) [19], respectively. This creates an additional gap of over $2 mm$ on each side of the talus that may permit additional rotations of the talus inside the mortise. The average width of the talus is $37 mm$ (Figure 6), therefore, the introduction of an additional $4 mm$ of inter-cortical space may be significant for such a small bone.

The anterior talofibular ligament and the calcaneofibular ligament are sectioned in the injury study. These are the primary inversion resisting ligaments [1]. For example, subject 3R increases its inversion range of motion fourfold. The posterior talofibular

ligament is now the primary inversion resisting ligamentous structure at the tibiotalar joint. This ligament is strained to 17% at a load of $147N$ (Figure 95). This ligament has a reported strain of 17% at its ultimate load of $418N$ [16]. It appears that the parameters of the quasi-linear viscoelastic representation of the ligaments are too flexible. At the subtalar joint, the interosseous and cervical ligaments assumed ligament properties may also contribute to the discrepancy between model and experimental results, as these ligaments also are recruited more so in the injured configuration to resist the externally applied inversion moment.

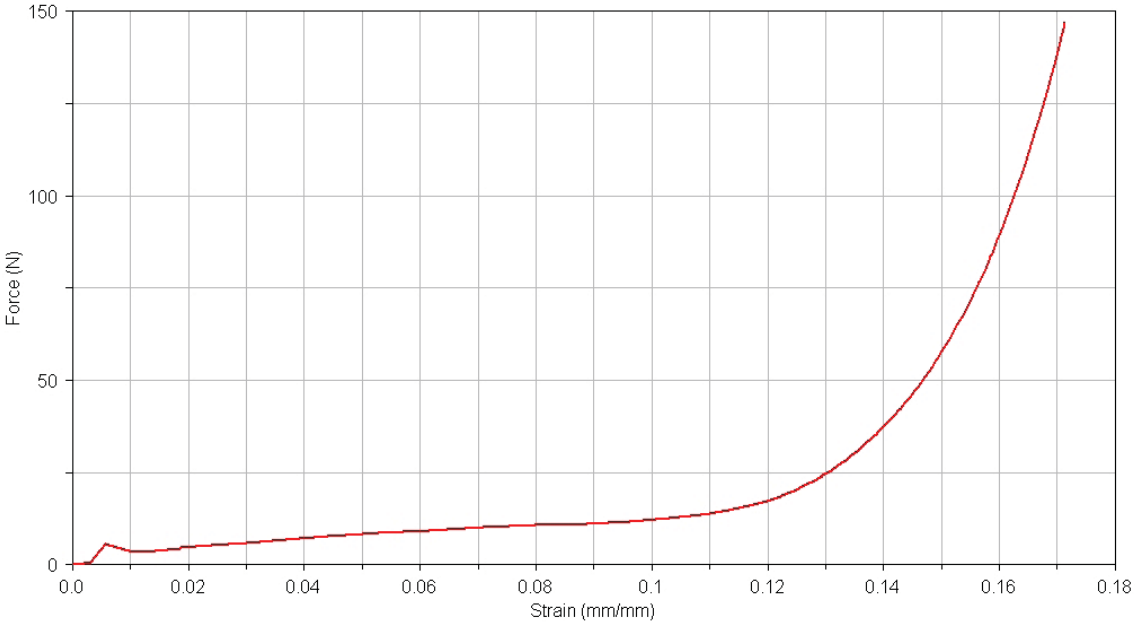

Figure 95. Posterior Talofibular Ligament Load-Strain

The surrounding tendons and other soft tissues aiding in the support of the ankle while loaded in inversion are neglected in the dynamic model. With the major support ligaments sectioned, it is reasonable to suspect the surrounding tendons and soft tissues would tend to aid in the resistance to inversion moment.

Model and experiment of subject 3R did not predict contact (Figure 63). Model 5L did not predict contact, but its experimental data detected a moderate sized contact area (Figure 65). However, model 5L is within 27% of experimental inversion range of motion (Table 10). This may indicate that the consistent model over prediction may be more dependent on the ligament material representation than the additional inter-cortical gap. The model predicted the joint would completely open up losing contact, while the experimental data is detecting contact. Models 4L and 5R (Figure 64 and Figure 66) predicted less contact area than the experimental data. This is the expected result based on the consistent model over prediction of inversion range of motion, as this has the effect of opening up the joint. However, the contact areas were in the same general location. Model 6R (Figure 67) predicted more contact area than the experimental data.

Average Model-to-Experiment Comparison

The average model-to-experiment comparison shows the rigid body dynamic model's ability to capture a wide range of passive mechanical properties under a variety of loadings. Average model predictions of range of motion are found to be within values reported previously [25, 28, 29] (Table 3 through Table 5). In addition, the variations of primary and coupled range of motion observed between the models were similar to those observed experimentally [24, 26, 27, 29, 73]. The models also capture the experimentally observed non-linear mechanical behavior of human joints [29, 70, 71] including hysteresis during loading-unloading cycles.

Effects of Morphology

The effects of morphology on passive mechanical properties show variations when compared on a subject-to-subject basis. The morphological variations of the bones, ligaments, and cartilage thickness show variations between subjects. The functional morphology of the sustentaculum tali geometry and calcaneofibular ligament orientation show a relationship to passive mechanics.

Subject-to-Subject Passive Mechanics Comparison

The ankle joint complex inversion range of motion and talar trochlear contact area and location comparison between the six subjects is discussed for the intact and injured ligament configurations.

Intact Ligament Configuration

The ankle joint complex inversion range of motion across the model population ranges from $6.2°$ to $16.3°$ with an average and standard deviation of $10.9 \pm 3.6°$ (Table 9) (Figure 72). The coefficient of variance is 0.33, indicating a subject to subject variation. From various experimental studies (Table 4), inversion range of motion varies from $6°$ to $30°$. The variations in the magnitude of the inversion range of motion fall within this range of experimental data.

The lowest inversion range of motion, $6.2°$, occurs in Model 7R. The broad fused anterior and middle articular facets and the posterior facet extension prevent the

sustentaculum tali from entering the canalis tarsi of the talus, thus limiting inversion rotation. The near vertical calcaneofibular ligament orientation may also be a contributing factor to the limited inversion range of motion for Model 7R.

Holding the boundary conditions, externally applied loads, ligament material properties, and cartilage material properties constant between all six models, the variations in morphology of the bones, articular surfaces, and ligaments are isolated. Therefore, the variation of the inversion range of motion between the six intact models is dependant on the individual's morphology.

The largest contact area, $417 mm^2$, 5R, spans all nine zones (Table 11) (Figure 73). The smallest contact area, $24 mm^2$, 4L, spans two zones. The contact areas of models 3R, 4L, 5L, and 6R, are concentrated on the anterior-medial side, Zones A, B, D, and E. The average contact area is $189 \pm 142 mm^2$. The coefficient of variation is 0.75, thus indicating variations between subjects. The contact area centroid location lies in Zone A for models 3R, 5L, and 6R, and in Zone E for models 5R and 7R, and in Zone B for model 4L. The spatial location of the contact area centroid varies, but there is a general clustering near the intersecting corner of Zones A, B, D, and E.

The percent contact area in each contact area zone compared between the six subjects show coefficients of variation ranging from 0.5 to 0.72 (Figure 75). Variations in contact area and its location between the six models is dependant on the individual's morphology.

Injured Ligament Configuration

The ankle joint complex inversion range of motion across the model population of this study ranges from $27.9°$ to $40.0°$ with an average and standard deviation of $33.7 \pm 5.6°$ (Table 10) (Figure 76). The coefficient of variance is 0.17, indicating some variance between subjects.

The contact area and location between the five subjects range from no contact in two Models, 3R and 5L, to contact in one to four zones, 4L, 5R, and 6R (Figure 77). The largest contact area, $109 mm^2$ (Table 12), 6R, spans Zones A, B, D, and E. The smallest contact area, $13 mm^2$, 5R, is contained in Zone A. The average contact area is $56 \pm 49 mm^2$. The coefficient of variation is 0.88, thus indicating variations between subjects. The contact area centroid location lies in Zone A for model 5R, and in Zone B for models 4L and 6R. The percent contact area in each contact area zone compared between the six subjects show coefficients of variation ranging from 0.14 to 0.65 (Figure 79).

Subject-to-Subject Morphological Variations

Variations of morphology such as dimensions of the bones and features, orientation and length of ligaments, and cartilage thickness distribution vary from subject to subject. These variations may be the cause of variations observed in passive mechanical properties.

Calcaneal Bone Dimensions

The length, width, and height of each calcanei exhibited no notable differences. The length of $84.9 \pm 3.6mm$ (Table 13) is 13% larger than the reported average of $75mm$, but within the bounding limits of $48mm$ and $98mm$ [1] (Figure 12). The average model width and height of $42.3 \pm 3.2mm$ and $43.3 \pm 2.2mm$, respectively, match the reported average of $40mm$ and $40mm$ [1]. These generalized outlining dimensions of the calcaneus are difficult to relate to variations in mechanics of the hindfoot, but they may be meaningful when studying the biomechanics of motion of the foot in regards to the plantar vault dimensions [22].

Calcaneal Articular Facet Configuration

Four of the six subjects have an anterior articulating facet separated from the middle articulating facet by a shallow, but distinct furrow. Classified as Type A (Figure 14), models 3R, 5L, 5R, and 6R, constitute 66% of the six subjects, in contrast to 32% previously reported [1] (Figure 15), while 7R and 4L are of Type B with the anterior and middle articular facets fused accounting for 33% of the subjects in contrast to 61% previously reported. However, the previously reported results include nearly 1900 specimens.

Sustentaculum Tali Inclination

Variations of the inclination of the sustentaculum tali range from 40° to 50° with an average and standard deviation of $46.3 \pm 3.9°$. The average matches the published value

of 46° (Figure 17). There appears to be no relationship between the sustentaculum tali inclination angle and the inversion range of motion for the intact and injured ligament configuration (Table 9 and Table 10).

Sustentaculum Tali Dimensions and Classification

Variations in the width of the sustentaculum tali range from 14.5*mm* to 18.4*mm* with an average and standard deviation of $16.2 \pm 1.5mm$ (Figure 83). The average width of the sustentaculum tali has been reported as 13*mm* (maximum 18*mm*, minimum 8*mm*) on a study of fifty calcanei [1]. The average of the six subjects of this study is toward the larger size of the reported average.

Calcanei 3R, 5L, 5R, and 6R have a short sustentaculum tali ending on the medial border at the middle and anterior articular facets (Figure 83 and Table 14). Calcanei 4L and 7R have a long sustentaculum tali continuous with the medial border. Models 4L and 7R predict the smallest inversion range of motion for the intact ligament configuration (Table 9). A long sustentaculum tali is usually associated with fusion of the anterior and middle articular facets [1]. This fusion and bracket like projection provides additional support to the talar head, preventing coupled plantarflexion, limiting inversion. The relationship between the sustentaculum tali length classification and the inversion range of motion ceases to exist for the injured ligament configuration. Models 4L and 5L, long and short respectively, predict nearly the same inversion range of motion (Table 10).

Calcaneofibular Ligament Orientation

The orientation of the calcaneofibular ligament in the six models ranges from 6° to 46° with an average and standard deviation of $34.5 \pm 14.7°$ (Figure 84). In a study of fifty five ankles, 75% had a calcaneofibular ligament orientation between 10° and 45° [17] (Figure 22). Five of the six subjects, 83%, fell within this range with the exception of 7R. 7R's calcaneofibular ligament orientation is 6°, corresponding to a near vertical ligament possibly contributed to the limited range of motion.

Talar Trochlear Cartilage Thickness Distribution

The average talar trochlear cartilage thickness ranges from 1.1*mm*, 3R, to 1.7*mm*, 7R (Figure 85). Models 4L, 5R, and 6R have thicker cartilage regions near the medial and lateral shoulders of the trochlear surface, consistent with other studies [19] (Table 1 and Figure 24). Models 5L and 7R cartilage distribution is progressively thinner lateral to medial. All specimens show a thicker posterior end than medial consistent with previously reported distributions (Table 1).

Functional Morphology

The morphology of the sustentaculum tali and calcaneofibular ligament orientation reveal a relationship to passive mechanical properties of the ankle joint complex.

Sustentaculum Tali Geometry

The ankle joint complex inversion range of motion is sensitive to the morphology of the sustentaculum tali. A series of morphological alterations to the sustentaculum tali varying its function show a progressive increase in inversion range of motion.

The functional morphology of the sustentaculum tali influences the inversion range of motion by more than doubling it from it's unaltered to obliterated states (Figure 91). Alteration #1 removed a significant portion of the sustentaculum tali that supports the talar head. Surprisingly, the inversion range of motion changed 7% and the talus appeared to be amply supported by the middle facet. Alteration #2 revealed a larger dependency on the inversion range of motion to the supportive function of the sustentaculum tali. This alteration changed the sustentaculum tali from a long to short. Lowering the middle articular facet elevation increased the inversion range of motion by permitting it to enter deeper into the canalis tarsi of the talus (Figure 5 and Figure 89). Alteration #3 removed all functional aspects of the sustentaculum tali. Alteration #4 confirms Alteration #3.

Calcaneofibular Ligament Orientation

The ankle joint complex inversion range of motion is sensitive to the calcaneofibular ligament orientation. Inversion range of motion increases with variation of the calcaneofibular ligament orientation from vertical to horizontal (Figure 93 and Figure 94).

The inversion range of motion was most limited with the calcaneofibular ligament in the vertical orientation, 12.2° (Figure 94). Coincidently, the ligament force is at its maximum, $106N$. In the horizontal orientation, the inversion range of motion is at its maximum, 19.9°. Coincidently, the ligament force is at its minimum, $72N$. From vertical to horizontal orientation, all simulations follow an increasing inversion range of motion with a decreasing ligament force. The inversion range of motion pattern is consistent with literature [1], a vertically oriented ligament is more restrictive because its tension is largest.

Chapter 6: Summary and Conclusions

Main Goal

Develop a subject specific image based numerical model of the human hindfoot capable of capturing complex three dimensional mechanics that may be used to investigate a correlation between subject-specific morphology and passive mechanical properties.

Model Development

Subject specific numerical models can isolate morphological variations and study their effect on passive mechanical response to external loadings. Subject specific models created from magnetic resonance image data incorporate unique morphological features of the bones, articulating surfaces, and ligament insertion and orientation. Morphological variations may be responsible for variations reported for mechanical behavior such as range of motion and contact. Numerical models can fix parameters such as ligament and cartilage material properties, externally applied loads, and boundary conditions. Studying the effect of morphological variations on resulting passive mechanical properties requires multiple subjects. A study performed using a single subject to develop a numerical model may overlook morphological variations between subjects. Three dimensional rigid body dynamic and finite element models incorporating unique morphological variations of six subjects are used to study the relationship between morphology and mechanics of the hindfoot.

Hindfoot kinetics are calculated using a subject specific numerical rigid body dynamic model [10, 74]. The model is capable of capturing a wide range of mechanical phenomenon such as range of motion, non-linear load-displacement characteristics, kinematic coupling, hysteresis, ligament load distribution, and spatial location and orientation throughout various simulated externally applied loads. The subject specific models are developed from stress magnetic resonance image data [6] of the hindfoot of six cadavers. The models are evaluated against stress magnetic resonance image data in inversion [74]. The evaluation is carried out for the intact and injured ligament configurations. This evaluation uses these models to study the relationship between morphology and passive mechanical properties and is the basis for the dynamic model development portion of this study.

A static finite element model of the hindfoot capable of describing contact area and its location based on position and orientation of the talus and calcaneus from the dynamic simulation is developed from three dimensional magnetic resonance image data. The three dimensional computerized bone representations are prepared for the finite element model. The original bone boundary of the dynamic model is reused to create the articulating surfaces for the finite element model. The articulating surface was offset an amount equal to the average cartilage thickness of the subject. The average cartilage thickness is based on nine measurements taken from the talar trochlear surface using the three dimensional reconstruction of the magnetic resonance image data. The offset layer represents the bone-cartilage interface. The articulating surface and the bone-cartilage interface surface are imported as superimposed three dimensional volumes into the finite

element preprocessor, then, they are subtracted to create a uniform three dimensional shell, representing the deformable cartilage layer, with its thickness equal to the average of the talar trochlear cartilage.

The three dimensional shell of each bone's deformable cartilage layer is meshed with tetrahedral elements and fixed boundary conditions are applied to the bone-cartilage interface surface. First order, or linear, tetrahedral elements are used to the mesh the deformable cartilage layer. One element through the cartilage thickness provides sufficient mesh refinement to capture the contact area. Fixed boundary conditions are applied to each node lying on the bone-cartilage interface. A fixed boundary condition is justified by the 100:1 bone to cartilage stiffness ratio.

The meshed deformable cartilage layer of each bone is assembled in the neutral position. Using position and orientation data from the dynamic model, the bones are repositioned into the time step corresponding to the simulated maximum inversion position. Positional data for three points attached to the inertial reference frame of the talus and calcaneus are obtained throughout the externally applied inversion load duration. The positional data of each bone provides a means of reassembling the finite element model of the hindfoot into any simulated position of the dynamic model.

The reassembled finite element model in the maximum inversion loaded position includes the inter-bone penetration as calculated by the rigid body dynamic model. The initially interpenetrated contact elements seek to remove the inter-body penetration by

deforming the elastic finite elements. Contact is detected by surface elements and calculated using the Augmented Lagrange Method.

Model Assumptions and Limitations

Assumptions and limitations are necessary for development of the subject specific numerical models.

Rigidly Constrained Fibula

The fibula and tibia were rigidly constrained in six degrees of freedom. The fibula is required to be fixed because the specimens were disarticulated below the knee. The fixity is required to maintain the itegrtiy of the distal tibiofibular complex. The basis for this assumption is that the malleolus of the fibula undergoes a slight distal displacement of $0.1mm$ to $0.5mm$ when the ankle was moved from full plantarflexion to full dorsiflexion, with variability among specimens [2]. Rotatory motions of the lateral malleolus were found to be less than $3°$ [37]. This assumption may have an over- and under-constraining effect on motion by removing flexibility of the distal tibiofibular complex. As the wedged posterior end of the trochlear surface enters the tibiofibular complex during plantarflexion, the fibula is known to tighten the joint [1]. Also, the wider anterior end of the trochlear surface is known to force open the tibiofibular joint in dorsiflexion [1].

Anterior Bone and Ligament Constraints

The dynamic and finite element models exclude the hindfoot's distal structures including the bones (cuboid and navicular) and soft tissues (ligaments), therefore, the motion of the talus and calcaneus may not be physiological [10]. The bones and ligament of the plantar vault (or the arches of the foot) primarily resist loads of weight bearing conditions (such as gait) [22]. Since the experiments and simulations are performed under non-weight bearing conditions, the constraint provided by such structures may not have a significant role in this study.

Exclusion of Cartilage Geometry

Cartilage geometry is not physically present in the dynamic and finite element models. The segmentation process delineated the bone structure from soft tissue structures which included the cartilage [10] (Appendix A). When the dynamic model was constructed, gaps were present between the bones where the volumes of articulating cartilage would normally be in contact. The gaps were required to be closed so that the bones would be in contact with each other while in the neutral position. This assumes the bone surfaces are the articular surfaces. This assumption translated the bones by the sum of the thickness of the articulating cartilage on each adjacent bone and rotated them from the scanned neutral position. The increased space between bones may cause small increases in joint rotations and translations.

Uniform Cartilage Thickness

The assumption of a uniform cartilage thickness will force the contact stiffness to be uniform across the articular surface. This may not be physiological because the contact stiffness may be a function of the thickness of the cartilage and therefore may spatially vary [19] (Table 1 and Figure 24).

Contact Stiffness

Cartilage has been described to behave as a biphasic transversely isotropic material [75-78]. The biphasic transversely isotropic material description is composed of viscous and solid phases.

Contact forces calculated in the dynamic model require a stiffness term, which must reflect the material properties of cartilage. The stiffness term is derived by the modulus of elasticity of cartilage, an average surface polygon area, and the average tibiotalar cartilage thickness [10] (Appendix A). The contact areas and cartilage material properties vary when moving the hindfoot [19, 72]; therefore, the stiffness term required would ideally vary as a function of this parameter [10]. Unfortunately, this feature is not included in the software. The cartilage stiffness varies exponentially according to internal algorithms in the dynamic simulation software. The exponentially varying stiffness is similar to previously reported viscoelastic and nonlinear behavior [79].

In the finite element model, the position and orientation of the talus and calcaneus are determined by the dynamic model. Therefore, the assumptions of the contact stiffness

term and cartilage behavior are carried into the finite element model. In the finite element model, the cartilage is assumed to behave as a linear elastic material. Sensitivity studies varying the elastic modulus of cartilage show a low sensitivity to contact area over a large range (Figure 56). Therefore, more complex constitutive equations may not be warranted in the finite element model.

Ligament Mechanical Properties

The material properties of the collateral ligament can deviate substantially from the average values [16], therefore generalized load-displacement properties for the ligaments [51] may be inadequate for developing patient-specific predictions of joint function [10]. For example, the anterior talofibular ligament and calcaneofibular ligament elastic modulus may vary as $255.5 \pm 181.3 MPa$ and $512.0 \pm 333.5 MPa$, respectively.

Subtalar Ligaments

The mechanical properties of the interosseous talocalcaneal ligament and cervical ligament are undocumented. Their mechanical properties are estimated by anterior talofibular ligament properties since these structures have similar physical characteristics [1].

Inertial Forces

The average dry weight of the bones of the hindfoot are input into the dynamic model and are all less than $0.25 kg$ [80]. This mass produces inertial forces on the talus of

approximately $5N$. This is significantly smaller than other forces in the system such as ligament forces, contact forces, and externally applied loads. This is due to the slow dynamic nature of this study.

Model Evaluation

Six subject specific numerical models of the hindfoot are developed to investigate the relationship between morphology and passive mechanical properties. Experimental data for each subject is the basis for evaluating the subject specific numerical models ability to predict inversion range of motion and talar trochlear contact area on a one-to-one basis. The one-to-one comparison is performed for the intact and injured lateral collateral ligament configurations. Experimental data for fifteen independent subjects is the basis for evaluating the plantarflexion / dorsiflexion, inversion / eversion, and internal / external rotation range of motion on an average basis.

One-to-One Model-to-Experiment Comparison

The one-to-one comparison is performed for the intact and injured lateral collateral ligament configurations.

Intact Ligament Configuration

The average percent difference between model and experiment of inversion range of motion for the six subjects is 29%. The models range from 6.2° to 16.3°, 260%, and experiment ranges from 5.8° to 21.8°, 375%. The average model to experiment percent

difference is small compared to the ranges. The reported population range varies from 6° to 35°, nearly 600%.

The experiment included subject variations of ligament and cartilage material properties. The material properties in all models are identical. If the difference in model to experiment range of motion is more dependent on material properties, not morphology, then, the differences between model and experiment would be large. Eventhough material properties vary widely among the population, the small difference between model and experiment reveal a stronger dependency on morphology.

The average percent difference between model and experiment of contact area and location distributed on the talar trochlear surface in all zones for all subjects is 40%.

Injured Ligament Configuration

The average percent difference between model and experiment of inversion range of motion for the five subjects is 40%. The models range from 27.9° to 40.0°, 143%, and experiment ranges from 21.1° to 30.8°, 146%.

There is a consistent over prediction of inversion range of motion for all subjects. Contact area and its location are under predicted. This may indicate that the numerical models are now more reliant on estimated ligament material properties from literature. Also, ligament strains exceed that found in literature. Therefore, the assumed ligament material properties may be overshadowing the effects of morphology.

Average Model-to-Experiment Comparison

The average percent difference between model and experiment for primary and coupled range of motion in plantarflexion / dorsiflexion, inversion / eversion, and internal / external rotation are with 18%. The reported ranges for these motions are 250% in plantarflexion, 300% in dorsiflexion, 600% in inversion, 400% in eversion, 160% in internal rotation, and 170% in external rotation. The average model to experiment percent difference is small compared to the reported ranges.

Experimental Assumptions and Limitations

The experimental evaluation used as the basis for evaluating the models is subject to assumptions and limitations.

Ankle Flexibility Tester

The Ankle Flexibility Tester [70] is used to obtain the inversion range of motion experimental data for six subjects in the intact and injured configurations. Due to the single rod fixation of the calcaneus to the foot plate of the Ankle Flexibility Tester, the calcaneus rotates slightly about the rod. These rotations are observed during anterior drawer testing [10]. Rotations are not reported for the inversion case [6, 10], so it is assumed that if present, they are negligible.

Unknown Subject Ankle Loading History

The cadaver subjects are reviewed by a doctor and found to be non-pathological. However, the loading history of the subjects is unavailable, therefore it is unknown if the subjects sustained injuries that might influence mechanics.

Effects of Morphology

Subject specific morphological variations of the bones, articulating surfaces, and ligaments show a relationship to passive mechanical properties. These morphological variations may explain variations in observed in joint mechanics.

Subject-to-Subject Passive Mechanics Comparison

The subject-to-subject comparison shows a dependency on passive mechanical response to the morphology of the bones, articulating surfaces, and ligaments. The morphology/mechanics relationship is parametrically studied using numerical models. In all models, subject specific morphology varies while material properties, loads, and boundary conditions are constant, therefore, isolating the effect of morphology. The subject-to-subject comparison is made for the intact and injured ligament configurations.

Intact Ligament Configuration

The inversion range of motion across the ankle joint complex and talar trochlear contact area and location of the intact human hindfoot loaded externally in inversion exhibit a dependency on the individual's morphology. The modeling framework holds all

parameters fixed such as: load, boundary conditions, ligament material properties, and cartilage material properties except those subject specific features such as: bone morphology, ligament insertion location, and cartilage thickness. Among the six subjects, the inversion range of motion varies by a factor of 2.6 with a coefficient of variance of 0.33. The contact area, contact area centroid location, and percent total contact area in each zone varies between subjects. Contact area varies by a factor of 17 with a coefficient of variance of 0.75. The contact area centroid varies in location but is confined to the anterior-medial, central-medial, and central zones. The largest percent of total contact area for each subject is distributed between the anterior-medial, central-medial, anterior-central, and central zones.

Injured Ligament Configuration

The inversion range of motion across the ankle joint complex and talar trochlear contact area and location of the human hindfoot loaded externally in inversion following lateral ligament injury exhibit a dependency on the individual's morphology. Among the five subjects, the inversion range of motion varies by a factor of 1.4 with a coefficient of variance of 0.17. The contact area, contact area centroid location, and percent total contact area in each zone varies between subjects. Contact area varies by a factor of 8 with a coefficient of variance of 0.88. The contact area centroid varies in location but is confined to the anterior-medial and central-medial zones. The largest percent of total contact area for each subject is distributed between the anterior-medial and central-medial zones.

Patterns of model over prediction of inversion may indicate the model is now reliant on ligament material properties assumed from literature. In some models, the tibiotalar joint excessively opens either predicting loss of contact or a smaller contact area determined by experiment. Ligament material properties are held constant between all subjects. Therefore, the effects of morphology on passive mechanics may be overshadowed by assumptions.

Subject-to-Subject Morphological Variations

Morphological features such as calcaneal bone dimensions, calcaneal articular facet configurations, sustentaculum tali inclination, and calcaneofibular ligament orientation are shown to vary among the six subjects of this study.

Calcaneal Bone Dimensions

The length, width, and height of the six calcanei exhibit little variation. The calcaneal bone dimensions show the least variation of the morphological features and fall with values reported in literature [1].

Calcaneal Articular Facet Configuration

The calcaneal articular facet configuration may be a strong factor in the determination of inversion range of motion. The sustentaculum tali of subjects 4L and 7R are continuous with anterior third of the calcaneal body and have fused anterior and middle articular facets. These subjects exhibit the lowest inversion range of motion. The continuous

sustentaculum supporting the fused facets may be restrictive to inversion motion. The calcaneal articular facet configuration is associated with the sustentaculum tali classification discussed below.

Sustentaculum Tali Inclination

The sustentaculum tali inclination varies 10° between the six subjects. However, there does not appear to be a relationship between inversion range of motion and this parameter.

Sustentaculum Tali Dimensions and Classification

The width of the sustentaculum tali varies slightly between the six subjects. There appears to be no correlation with this parameter to inversion range of motion. However, there appears to be a relationship between inversion range of motion and the short/long sustentaculum tali classification. A long sustentaculum tali may limit the inversion range of motion. The sustentaculum tali of subjects 4L and 7R are classified as long, and consequently measure the smallest inversion range of motion. A long sustentaculum tali may be associated with a posterior extension of the middle articular facets on the talar neck. This fusion on the talus seemingly flattens the canalis tarsi (Figure 10). A short sustentaculum tali, with separate anterior and middle articular facets, may be associated with a distinct tarsal canal. The short sustentaculum tali may fit deeper into the tarsal canal permitting additional inversion rotation. These patterns of functional morphology

of the sustentaculum tali are supported by studying the effects of alterations to the sustentaculum tali, changing its classification from long to short.

Calcaneofibular Ligament Orientation

The calcaneofibular ligament orientation varies between subjects. The ligament orientation for five of the subjects falls within the common range of 10° to 45° and one subject falls in the vertical range. With the exception of Model 6R, there is an increasing inversion range of motion with increasing ligament orientation from the vertical position. This follows patterns of ligament function in literature [1] and is supported by the functional morphological study of the calcaneofibular ligament orientation.

Talar Trochlear Cartilage Thickness Distribution

The talar trochlear cartilage thickness varies across the articulating surface. The cartilage thickness is assumed to be the average of nine measurements. These measurements are consistent with previous studies [19, 20].

Functional Morphology

The modification to local features such as the sustentaculum tali geometry and the calcaneofibular ligament orientation show a morphological relationship to inversion range of motion.

Sustentaculum Tali Geometry

Alterations to the geometry of the sustentaculum tali exhibit a strong functional morphological relationship to inversion range of motion. The sustentaculum tali of model 7R is classified as long, with the anterior and middle articulating facets fused. The boney extension of the sustentaculum tali onto the anterior third of the calcaneal body is thought to provide additional support to the talar head when it plantarflexes as coupled motion to an externally applied inversion moment, thus potentially limiting the inversion range of motion. However, complete removal of the anterior boney extension had little effect on inversion range of motion. This is due to the conforming nature of the remaining sustentaculum tali located in the canalis tarsi. The alteration changing the supportive function of the sustentaculum tali and the associated middle articular facet had the largest effect on inversion range of motion by more than doubling it. This alteration changes the classification of the sustentaculum tali from long to short. The sustentaculum tali may enter deeper into the tarsal canal permitting more inversion rotation.

The sustentaculum tali's effect on inversion range of motion and the relationship with the classification of short or long may show a stronger relationship to the supportive function of the neck, not the head. The functional morphology study of the sustentaculum tali shows a low sensitivity of the removal of the boney extension. This may be explained by the tightly conforming fit to the canalis tarsi of the talus (Figure 47). Model 4L also has a conforming sustentaculum tali, classified it as long, and measures the second lowest inversion range of motion.

Calcaneofibular Ligament Orientation

Alterations to the orientation of the calcaneofibular ligament exhibit a strong morphological relationship to inversion range of motion. Inversion range of motion is most restricted when the ligament is vertically oriented and least restricted with a horizontal orientation. The pattern of increasing inversion rotation with ligament orientations varying from vertical to horizontal is consistent functional descriptions from literature [1]. From vertical to horizontal, a 63% increase in inversion range of motion is observed. Contrary to literature, the model ligament experiences tension loads in all orientations due to inversion moments. Ligament forces are thought to be near constant for a common calcaneal insertion site and zero, or laxed, for horizontal orientations [1]. This may be explained by repositioning the calcaneal insertion to non-physiological locations due to the constant ligament length.

Clinical Relevance

Morphology may be the reason for variations in the outcome of non-operative and surgical treatments of ankle disorders. Variations in treatment outcome may include patient satisfaction, pain, limited range of motion, instability, and osteoarthritis. Treatments range from casting and rest to invasive procedures such as: ligament reconstruction, ankle or subtalar arthrodesis, and total ankle replacement. These treatments may lead to altered joint mechanics.

When non-operative treatments of lateral ligament ankle injuries fail, reconstructive procedures may be performed. Two main classes of these procedures exist: anatomical

reconstruction and tenodesis, for each of which several procedures have been developed. The outcome of these procedures varies in regards to the patients subjective satisfaction, limited range of motion, pain, swelling, and osteoarthritis.

Anterior talar translation tests of 25 Evans tenodesis patients in a twenty-year follow-up showed some instability of the surgically treated ankle when compared to the contralateral ankle [81]. Seven of the subjects showed varying signs of osteoarthritis [81].

A long-term follow-up of anatomical reconstruction versus tenodesis for the treatment of chronic lateral instability of the ankle joint shows the anatomical reconstruction gives more favorable results than the tenodesis [82]. Of the anatomical reconstruction group, 9 patients underwent periostal flap plasty according to Reichelt and Weyrauch and 16 underwent the Broström procedure. Of the tenodesis group, 12 patients underwent a Watson-Jones procedure, and 17 patients underwent a modified Castaing procedure. Six had limited range of motion, 21 had pain on palpation, 25 showed signs of instability based on anterior drawer tests, and 28 showed signs of articular cartilage degeneration as seen on lateral radiographs [82].

If osteoarthritis has progressed beyond tolerance, or the initial ankle damage is too severe, other surgical procedures may be employed, such as arthrodesis or total ankle replacement. The majority of long-term follow-up of patients who underwent ankle arthrodesis have reported moderate to severe osteoarthritis in the subtalar joint and some

developed osteoarthritis in adjacent joints such as the talonavicular, calcaneocuboid, etc. [83, 84]. A study of the outcome of subtalar arthrodesis also shows the majority of patients develop osteoarthritis of the ankle joint [85].

Preliminary Clinical Significance

Osteoarthritis in the ankle joint appears to, in the majority of cases, follow a traumatic episode. Inversion injury of the lateral ligaments is the most frequent traumatic episode. Standardized surgical treatments may temporarily relieve patient discomfort but do however, have long-term osteoarthritic effects. The many parameters of an individual's morphology show large variations from subject to subject. Furthermore, the mechanics of individuals' ankles vary widely across the population. It is believed that these parameters affect the outcome of a patient's response to standardized surgical treatments. The overwhelming evidence that these standardized surgical treatments yield unfavorable results leads to the notion of patient-specific surgical treatments to ankle disorders. Furthermore, the cause and effect relationship between lateral ankle ligament inversion injuries and post-traumatic osteoarthritis may give insight to the origins of osteoarthritis from a mechanical viewpoint.

List of References

1. Sarrafian, S.K., *Anatomy of the foot and ankle : descriptive, topographic, functional*. 2nd ed. 1993, Philadelphia: Lippincott. xvii, 616 p.

2. Stiehl, J.B. and V.T. Inman, *Inman's joints of the ankle*. 2nd ed. 1991, Baltimore: Williams & Wilkins. xvi, 155 p.

3. Dwight, T., *Variations of the bones of the hands and feet: A clinical atlas*. 1907, Philadelphia & London,: J. B. Lippincott company. x, 25 p., 1 l.

4. Singh, I., *Squatting facets on the talus and tibia in Indians.* J Anat, 1959. **93**: p. 540-50.

5. Wood, W.Q., *The Tibia of the Australian Aborigine.* J Anat, 1920. **54**(Pt 2-3): p. 232-57.

6. Ringleb, S.I., S. Siegler, and Drexel University. College of Engineering., *A three-dimensional stress MRI technique to quantify the mechanical properties of the ankle and subtalar joint -- : application to the diagnosis of ligament injuries*. 2003, Drexel University.

7. Udupa, J.K., et al. *3DVIEWNIX: An Open Transportable, Multidimensional, Multiparametric Imaging Software System*. in *Proceedings of SPIE*. 1994.

8. Bunning, P.S. and C.H. Barnett, *A Comparison of Adult and Foetal Talocalcaneal Articulations.* J Anat, 1965. **99**: p. 71-6.

9. Laidlaw, P.P., *The Varieties of the Os Calcis.* J Anat Physiol, 1904. **38**(Pt 2): p. 133-43.

10. Imhauser, C.W., S. Siegler, and Drexel University., *Development and evaluation of a 3-dimensional, image-based, patient-specific, dynamic model of the hindfoot (The)*. 2004, Drexel University.

11. Boruta, P.M., et al., *Acute lateral ankle ligament injuries: a literature review.* Foot Ankle, 1990. **11**(2): p. 107-13.

12. (NIAMS), N.I.o.A.a.M.a.S.D., *Questions & Answers about Sprains and Strains.* 2004.

13. CureResearch.com. *Statistics about Ankle Sprain*. 2008; Available from: http://www.cureresearch.com/a/ankle_sprain/stats.htm.

14. Valderrabano, V., et al., *Ligamentous posttraumatic ankle osteoarthritis.* Am J Sports Med, 2006. **34**(4): p. 612-20.

15. Buckwalter, J.A., C. Saltzman, and T. Brown, *The impact of osteoarthritis: implications for research.* Clin Orthop Relat Res, 2004(427 Suppl): p. S6-15.

16. Siegler, S., J. Block, and C.D. Schneck, *The mechanical characteristics of the collateral ligaments of the human ankle joint.* Foot Ankle, 1988. **8**(5): p. 234-42.

17. Ruth, C.J., *The surgical treatment of injuries of the fibular collateral ligaments of the ankle.* J Bone Joint Surg Am, 1961. **43**(229).

18. Shepherd, D.E. and B.B. Seedhom, *Thickness of human articular cartilage in joints of the lower limb.* Ann Rheum Dis, 1999. **58**(1): p. 27-34.

19. Athanasiou, K.A., G.G. Niederauer, and R.C. Schenck, Jr., *Biomechanical topography of human ankle cartilage.* Ann Biomed Eng, 1995. **23**(5): p. 697-704.

20. Millington, S.A., et al., *Quantitative and topographical evaluation of ankle articular cartilage using high resolution MRI.* J Orthop Res, 2007. **25**(2): p. 143-51.

21. O'Farrell, T.A. and B.G. Costello, *Osteochondritis dissecans of the talus. The late results of surgical treatment.* J Bone Joint Surg Br, 1982. **64**(4): p. 494-7.

22. Kapandji, I.A., *The physiology of the joints: annotated diagrams of the mechanics of the human joints*. 2nd ed. 1970, London,: E. & S. Livingstone. 3 v.

23. Nordin, M. and V.H. Frankel, *Basic biomechanics of the musculoskeletal system*. 2nd ed. 1989, Philadelphia: Lea & Febiger. xxiii, 323 p.

24. Siegler, S., J. Chen, and C.D. Schneck, *The three-dimensional kinematics and flexibility characteristics of the human ankle and subtalar joints--Part I: Kinematics.* J Biomech Eng, 1988. **110**(4): p. 364-73.

25. Allinger, T.L. and J.R. Engsberg, *A method to determine the range of motion of the ankle joint complex, in vivo.* J Biomech, 1993. **26**(1): p. 69-76.

26. Lundberg, A., et al., *Kinematics of the ankle/foot complex--Part 2: Pronation and supination.* Foot Ankle, 1989. **9**(5): p. 248-53.

27. Siegler, S., et al., *Mechanics of the ankle and subtalar joints revealed through a 3D quasi-static stress MRI technique.* J Biomech, 2005. **38**(3): p. 567-78.

28. Cass, J.R., B.F. Morrey, and E.Y. Chao, *Three-dimensional kinematics of ankle instability following serial sectioning of lateral collateral ligaments.* Foot Ankle, 1984. **5**(3): p. 142-9.

29. Kjaersgaard-Andersen, P., et al., *Instability of the hindfoot after lesion of the lateral ankle ligaments: investigations of the anterior drawer and adduction maneuvers in autopsy specimens.* Clin Orthop Relat Res, 1991(266): p. 170-9.

30. Driscoll, H.L., J.C. Christensen, and A.F. Tencer, *Contact characteristics of the ankle joint. Part 1. The normal joint.* J Am Podiatr Med Assoc, 1994. **84**(10): p. 491-8.

31. Corazza, F., et al., *Articular contact at the tibiotalar joint in passive flexion.* J Biomech, 2005. **38**(6): p. 1205-12.

32. Anderson, D.D., et al., *Physical validation of a patient-specific contact finite element model of the ankle.* J Biomech, 2007. **40**(8): p. 1662-9.

33. Wang, C.L., et al., *Contact areas and pressure distributions in the subtalar joint.* J Biomech, 1995. **28**(3): p. 269-79.

34. Ward, K.A. and R.W. Soames, *Contact patterns at the tarsal joints.* Clin Biomech (Bristol, Avon), 1997. **12**(7-8): p. 496-507.

35. Barbaix, E., P. Van Roy, and J.P. Clarys, *Variations of anatomical elements contributing to subtalar joint stability: intrinsic risk factors for post-traumatic lateral instability of the ankle?* Ergonomics, 2000. **43**(10): p. 1718-25.

36. Gupta, S.C., C.D. Gupta, and A.K. Arora, *Pattern of talar articular facets in Indian calcanei.* J Anat, 1977. **124**(Pt 3): p. 651-5.

37. Barnett, C.H. and J.R. Napier, *The axis of rotation at the ankle joint in man; its influence upon the form of the talus and the mobility of the fibula.* J Anat, 1952. **86**(1): p. 1-9.

38. Hicks, J.H., *The mechanics of the foot. I. The joints.* J Anat, 1953. **87**(4): p. 345-57.

39. Manter, J.T., *Movements of the subtalar and transverse tarsal joints.* Anat Rec, 1941. **80**: p. 397-410.

40. Stormont, D.M., et al., *Stability of the loaded ankle. Relation between articular restraint and primary and secondary static restraints.* Am J Sports Med, 1985. **13**(5): p. 295-300.

41. Luo, Z.P., et al., *Physiological elongation of ligamentous complex surrounding the hindfoot joints: in vitro biomechanical study.* Foot Ankle Int, 1997. **18**(5): p. 277-83.

42. Leardini, A., et al., *A geometric model of the human ankle joint.* J Biomech, 1999. **32**(6): p. 585-91.

43. Scott, S.H. and D.A. Winter, *Biomechanical model of the human foot: kinematics and kinetics during the stance phase of walking.* J Biomech, 1993. **26**(9): p. 1091-1104.

44. Bandak, F.A., R. Tannous, and T. Toridis, *On the Development of and Osseo-Ligamentous Finite Element Model of the Human Ankle Joint.* International Journal of Solids and Structures, 2001. **38**: p. 1681-1697.

45. Camacho, D.L., et al., *A three-dimensional, anatomically detailed foot model: a foundation for a finite element simulation and means of quantifying foot-bone position.* J Rehabil Res Dev, 2002. **39**(3): p. 401-10.

46. Ledoux, W.R., R.P. Ching, and E.S. Rohr, *The development and validation of a computational foot and ankle model.* 22nd Annual EMBS International Conference, 2000.

47. Cheung, J.T., et al., *Three-dimensional finite element analysis of the foot during standing--a material sensitivity study.* J Biomech, 2005. **38**(5): p. 1045-54.

48. Grevera, G.J., *Bone Surface Identification Software (an in-house developed program)*, Medical Image Processing Group, University of Pennsylvania.

49. *Geomagic Studio*, Geomagic, Inc.

50. Treppo, S., et al., *Comparison of biomechanical and biochemical properties of cartilage from human knee and ankle pairs.* J Orthop Res, 2000. **18**(5): p. 739-48.

51. Funk, J.R., et al., *Linear and quasi-linear viscoelastic characterization of ankle ligaments.* J Biomech Eng, 2000. **122**(1): p. 15-22.

52. *Adams/View*. 2006, MSC Software Corporation.

53. Negrut, D. and B. Harris, *ADAMS Theory in a Nutshell*. 2001: Department of Mechanical Engineering, University of Michigan, Ann Arbor.

54. MSC.Software, *ADAMS/Solver Manual*. 2006, MSC.Software Corporation. p. 66-70.

55. MSC.Software, *ADAMS/Solver Manual*. 2006, MSC.Software Corporation. p. 590-598.

56. Gear, C.W., *Simultaneous Numerical Solution of Differential-Algebraic Equations.* IEEE Trans Circ Theory, 1971. **18**: p. 89-95.

57. Gottschalk, S., M.C. Lin, and D. Manocha. *OBB Tree: A Hierarchial Structure for Rapid Interference Detection*. in *The 23rd Annual International Conference on Computer Graphics and Interactive Techniques*. 1996.

58. Langton, C.M., et al., *Prediction of mechanical properties of the human calcaneus by broadband ultrasonic attenuation.* Bone, 1996. **18**(6): p. 495-503.

59. *ANSYS Release 11.0, Service Pack 1*. 2007.

60. Bathe, K.-J., *Finite element procedures*. 1996, Englewood Cliffs, N.J.: Prentice Hall. xiv, 1037 p.

61. *Basic Structural Nonlinearities, Training Manual*: ANSYS, Inc.

62. Johannsen, A., *Radiological diagnosis of lateral ligament lesion of the ankle. A comparison between talar tilt and anterior drawer sign.* Acta Orthop Scand, 1978. **49**(3): p. 295-301.

63. Kinzel, G.L., A.S. Hall, Jr., and B.M. Hillberry, *Measurement of the total motion between two body segments. I. Analytical development.* J Biomech, 1972. **5**(1): p. 93-105.

64. Udupa, J.K., et al., *Analysis of in vivo 3-D internal kinematics of the joints of the foot.* IEEE Trans Biomed Eng, 1998. **45**(11): p. 1387-96.

65. *Geomagic Qualify*, Geomagic, Inc.

66. Chen, J., S. Siegler, and C.D. Schneck, *The three-dimensional kinematics and flexibility characteristics of the human ankle and subtalar joint--Part II: Flexibility characteristics.* J Biomech Eng, 1988. **110**(4): p. 374-85.

67. Wu, G., et al., *ISB recommendation on definitions of joint coordinate system of various joints for the reporting of human joint motion--part I: ankle, hip, and spine. International Society of Biomechanics.* J Biomech, 2002. **35**(4): p. 543-8.

68. Spoor, C.W. and F.E. Veldpaus, *Rigid body motion calculated from spatial co-ordinates of markers.* J Biomech, 1980. **13**(4): p. 391-3.

69. Greenwood, D.T., *Principles of dynamics*. 2nd ed. 1988, Englewood Cliffs, N.J.: Prentice-Hall. viii, 552 p.

70. Siegler, S., et al., *A six-degrees-of-freedom instrumented linkage for measuring the flexibility characteristics of the ankle joint complex.* J Biomech, 1996. **29**(7): p. 943-7.

71. Tohyama, H., et al., *Biomechanical analysis of the ankle anterior drawer test for anterior talofibular ligament injuries.* J Orthop Res, 1995. **13**(4): p. 609-14.

72. Calhoun, J.H., et al., *A comprehensive study of pressure distribution in the ankle joint with inversion and eversion.* Foot Ankle Int, 1994. **15**(3): p. 125-33.

73. Hintermann, B. and B.M. Nigg, *[Pronation from the viewpoint of the transfer of movement between the calcaneus and the tibia].* Schweiz Z Sportmed, 1993. **41**(4): p. 151-6.

74. Imhauser, C.W., Toy, J.R., et al., *Subject-specific models of the hindfoot reveal a relationship between morphology and passive mechanical properties.* J Biomech, 2008. **41**(6): p. 1341-9.

75. Donzelli, P.S., et al., *Contact analysis of biphasic transversely isotropic cartilage layers and correlations with tissue failure.* J Biomech, 1999. **32**(10): p. 1037-47.

76. Mow, V.C., et al., *Biphasic creep and stress relaxation of articular cartilage in compression? Theory and experiments.* J Biomech Eng, 1980. **102**(1): p. 73-84.

77. Dunbar, W.L., Jr., et al., *An evaluation of three-dimensional diarthrodial joint contact using penetration data and the finite element method.* J Biomech Eng, 2001. **123**(4): p. 333-40.

78. Un, K. and R.L. Spilker, *A penetration-based finite element method for hyperelastic 3D biphasic tissues in contact: Part 1--Derivation of contact boundary conditions.* J Biomech Eng, 2006. **128**(1): p. 124-30.

79. Park, S., C.T. Hung, and G.A. Ateshian, *Mechanical response of bovine articular cartilage under dynamic unconfined compression loading at physiological stress levels.* Osteoarthritis Cartilage, 2004. **12**(1): p. 65-73.

80. Beillas, P., et al. *Foot and Ankle Finite Element Modeling Using CT-Scan Data*. in *43rd Stapp Car Crash Conference*. 1999. San Diego, California.

81. Korkala, O., et al., *Twenty-year results of the Evans operation for lateral instability of the ankle.* Clin Orthop Relat Res, 2002(405): p. 195-8.

82. Krips, R., et al., *Long-term outcome of anatomical reconstruction versus tenodesis for the treatment of chronic anterolateral instability of the ankle joint: a multicenter study.* Foot Ankle Int, 2001. **22**(5): p. 415-21.

83. Coester, L.M., et al., *Long-term results following ankle arthrodesis for post-traumatic arthritis.* J Bone Joint Surg Am, 2001. **83-A**(2): p. 219-28.

84. Morrey, B.F. and G.P. Wiedeman, Jr., *Complications and long-term results of ankle arthrodeses following trauma.* J Bone Joint Surg Am, 1980. **62**(5): p. 777-84.

85. de Heus, J.A., et al., *The influence of subtalar and triple arthrodesis on the tibiotalar joint. A long-term follow-up study.* J Bone Joint Surg Br, 1997. **79**(4): p. 644-7.

86. Falcao, A.X., et al., *User-Steered Image Segmentation Paradigms: Live Wire and Live Lane.* Graphical Models and Image Processing, 1998. **60**: p. 233-260.

87. Saha, P.K., et al., *Iso-shaping rigid bodies for estimating their motion from image sequences.* IEEE Trans Med Imaging, 2004. **23**(1): p. 63-72.

88. Stindel, E., et al., *A characterization of the geometric architecture of the peritalar joint complex via MRI: an aid to the classification of foot type.* IEEE Trans Med Imaging, 1999. **18**(9): p. 753-63.

89. Stindel, E., et al., *3D MR image analysis of the morphology of the rear foot: application to classification of bones.* Comput Med Imaging Graph, 1999. **23**(2): p. 75-83.

90. Fung, Y.C., *Biomechanics : mechanical properties of living tissues*. 2nd ed. 1993, New York: Springer-Verlag. xviii, 568 p.

91. Izambert, O., et al., *Dynamic stiffness and damping of human intervertebral disc using axial oscillatory displacement under a free mass system.* Eur Spine J, 2003. **12**(6): p. 562-6.

92. Ascher, U.M. and L.R. Petzold, *Computer methods for ordinary differential equations and differential-algebraic equations*. 1998, Philadelphia: Society for Industrial and Applied Mathematics. xvii, 314 p.

93. Chenney, S., *Computer Gaming Technology*. 2001: University of Wisconsin.

Appendix A

Model Development

The magnetic resonance image processing, computerized bone representation generation, and rigid body dynamic model development steps are based on existing work [10]. These steps are summarized herein.

Image Processing

3DVIEWNIX is an image processing and visualization software system. It is used to create three dimensional renderings of the bones and identify the ligament insertion points.

Step 1: Segmentation

The segmentation process involves isolation of the bone boundary from the adjacent soft tissue for each two-dimensional magnetic resonance image slice. It is performed using a user interactive process referred to as "live-wire" [86] (Figure 96).

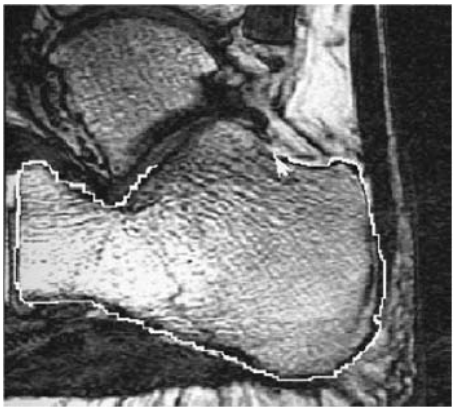

Figure 96. Segmented Magnetic Resonance Image Slice

Step 2: Iso-Shaping

Two of the bones comprising the hindfoot, the tibia and fibula, are long bones, which appear only partially within the field of view used for magnetic resonance image scanning. Iso-shaping truncates, or trims, longs bones in a uniform manner which allows for proper registration.

Step 3: Surface Construction

Surfaces are created and displayed after the binary images produced in the previous step are interpolated and filtered with a smoothing Gaussian Filter [87]. A three dimensional Gaussian filter with a standard deviation of 2 is used to smooth the bone surfaces. The filter is a convolution operator that acts to blur the image. The degree of smoothing is determined by the standard deviation of the Gaussian [7, 86]. The purpose of filtering is the estimation of the surface normals that are, as much as possible, free from digital artifacts.

Step 4: Estimation of Morphological and Architectural Parameters

Morphological and architectural parameters are estimated from the surface's output in Step 3 for each bone in each configuration by using well-established methods [[64], [7, 88, 89]]. The morphological parameters computed for each bone include the location of the geometric centroid of the bone's surface in the scanner coordinate system, the volume enclosed by the surface of the bone, the direction of each of the three principle axes of the bone, and the length to the intersection of each principle axis with the surface of the bone.

Computerized Bone Representations

Cartesian coordinates describing the outer surface of each hindfoot bone, in the form of point cloud data, are used to identify spatial coordinates to triangulate the surface and create polygon representations of the bones surfaces.

Bone Surface Identification Software

Cartesian coordinates describing the outer surface of each hindfoot bone are obtained from the segmented two dimensional magnet resonance slice data (*.bim files) [48]. The software includes several algorithms for identifying the surface coordinates to triangulate the boundary of the bone.

Polygon Representation

The Geomagic Studio [49] software can convert and manipulate the surface coordinate data obtained as output form the bone surface identification software to standardized solid computerized model formats (i.e. *.iges, *.step, *.stl). The bone geometries were processed using following steps: 1) global noise reduction, 2) point wrapping, 3) local surface smoothing, and 4) point decimation.

In the global noise reduction step, statistical methods reduce geometric abnormalities about the entire bone surface. The data output from the bone surface identification software is arranged so that the bones have a staircase structure (Figure 97-Before). The noise reduction step smoothes the staircase structure (Figure 97-After). The point wrapping process converts the point cloud data to polygons describing the bone surface.

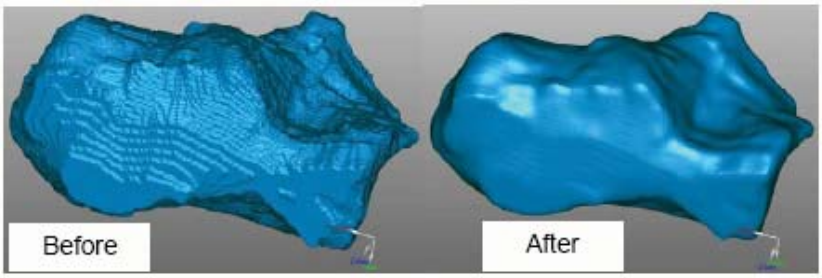

Figure 97. Wrapped Bone Surface Representation Before/After Noise Reduction

Following the wrap phase, the model is converted to a closed volume in the polygon phase. This phase has several surface editing features that allow any non-anatomical geometric artifacts (as determined by the user) to be removed such as spikes on the bone surface. The *defeature* command removes small spikes on the bone surfaces. This command refits selected regions with a new triangulated surface. For areas with greater surface irregularity, such as the tubercle of insertion of the deltoid ligament (Figure 98a), it is not possible to use this function. First, the appropriate area is highlighted (Figure 98b). The highlighted area is then deleted, which leaves holes in the surface representation of the bone as highlighted in green (Figure 98c). The *fill holes* tool is used to refit this area with a new polygon surface (Figure 98d).

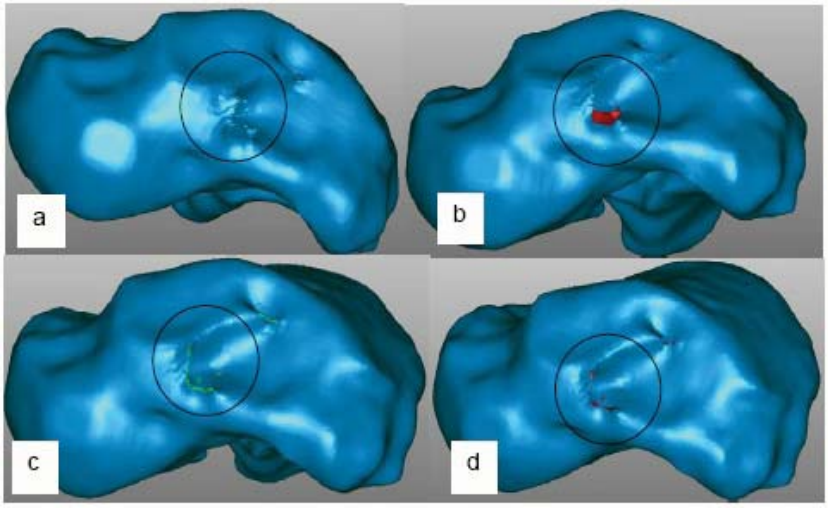

Figure 98. Local Bone Surface Smoothing

This operation constructs a polygon structure to fill the hole, and both the hole and the surrounding region are remeshed so the polygonal layout is organized and continuous. The spikes tended to occur at locations where the bone geometry is not well defined such as ligament insertion points. This typically happens in locations where the surface of the bone is near parallel to the magnetic resonance imaging plane. They did not occur in regions with smooth geometries such as articulating surfaces. Finally, the *decimate polygons* tool is used to reduce the number of triangles representing the bone surface. This tool is run in *shape preservation* mode, which ensured that the object's overall shape is preserved. Simulation times are directly related to the number of points describing bone surfaces, therefore it is important to use the lowest amount possible while maintaining bone geometry. Each bone is described with approximately 250,000 polygons (Figure 99a), which is then decimated to approximately 9,000 polygons (Figure 99b).

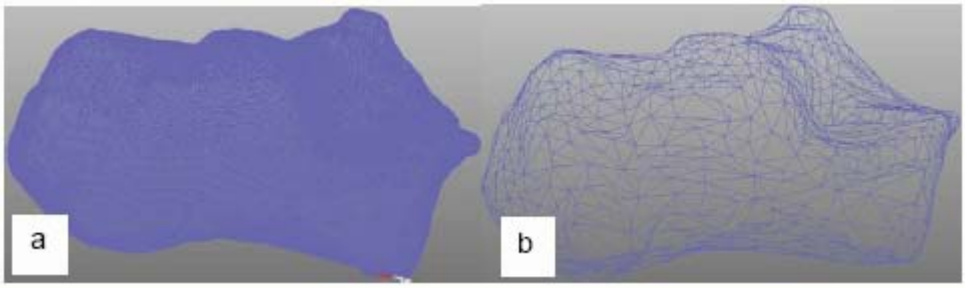

Figure 99. Triangulated Bone Surface Decimation
Before (a) and After (b)

Rigid Body Dynamic Model

The three dimensional computer representation of the tibia, fibula, talus, and calcaneus were imported into the rigid body dynamic simulation software, Adams [52], using the

stereolithograph format. The bones maintained their positions relative to the magnetic resonance image scanner reference frame.

Ligament Insertion Location

Identification of the insertion sites of ligaments is performed using a re-slicing algorithm. Ligament insertions are identified by applying 3DVIEWNIX's *Manipulate* and *Measure* features to each subject's reconstructed and assembled hindfoot bones. Ligaments are identified by first intersecting the assembled hindfoot structure with a plane that is oriented in a manner best suited for identifying the course of the ligament (Figure 100a). The *Measure* tool is used to obtain the location of the ligament insertion points in terms of the magnetic resonance scanner frame (Figure 100b). The insertions coordinates are transformed from the scanner frame to the inertial frame of the bones in the model (Figure 100c).

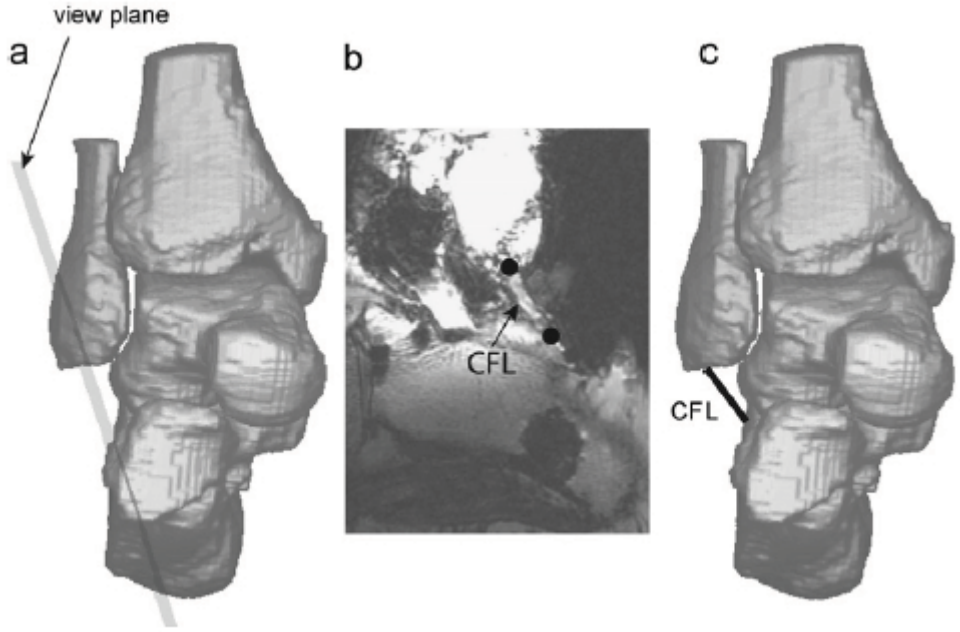

Figure 100. Ligament Insertion Identification

A few translational and rotational operations are typically required for the user to align the view plane with the course of each ligament. The collateral ligament diameter [16] (between 3.5 mm and 7.6 mm) is greater than the largest magnetic resonance image voxels' spatial dimension (2.1 mm), ensuring identification of these structures using the re-slicing algorithm.

Ligament Mechanics

Each ligament is modeled as a tension-only element with non-linear load (T) – strain (ε) relationship (Equation 6).

$$T(\varepsilon) = (A\left(e^{B\varepsilon} - 1\right) + 0.1 * VR(M1, M2)) * step(DM(M1, M2), L_o, 0, L_0 + 0.1, 1) \quad \textbf{Equation 6}$$

This expression is derived using quasi-linear viscoelastic theory [90]. The constants, A and B, are obtained in previous studies [51] by fitting the equation to experimental load-displacement tests for individual collateral ligaments bone-ligament-bone preparations. The VR term monitors the magnitude of the first time derivative of the displacement vector between the ligament insertion points, M1 and M2. The *step* function, internal to the rigid body dynamic simulation software [52], is used to provide a continuous transition from the on and off states in the form of a cubic polynomial to avoid numerical discontinuities. No structures are assigned time dependant relaxation properties. All loading times are at most three seconds and minimal relaxation occurs (< 10% decrease) over this time period [51]; therefore this component is not included in the model of the ligament force properties. The mechanical properties of the subtalar ligaments are

unknown. Therefore, they are assigned the same material properties as the posterior tibiotalar ligament since they have similar gross morphological appearance [1] and similar cross-sectional areas [16].

Cartilage Mechanics

The force developed between contacting articular surfaces is defined as a non-linear function of penetration depth, x, and the penetration velocity, $\dot{x}$ (Equation 7).

$$Force = k\left(x\right)^{e} + step(x, 0, 0, d_{\max}, c)\dot{x} \qquad \textbf{Equation 7}$$

The penetration depth is scaled by a stiffness term, k, which is based on the experimental compressive modulus of cartilage at the distal tibia and talar dome ($E = 0.374MPa$) [50]. The modulus is scaled by the local average area, A, of the polygons comprising each bone surface mesh at the articulating surfaces, and thickness, t, of the articular cartilage at each joint (Equation 8).

$$k = E\frac{A}{t} \qquad \textbf{Equation 8}$$

The penetration depth is also scaled by an exponent term, e, which models the nonlinear compressive properties of cartilage [79]. The choice of the exponent, e, is based on cartilage's non-linear behavior under axial loading [79]. Physiologically, the cartilage can not exceed a compressive axial strain of 100%. Therefore, an exponent is chosen so

bone penetration would not be greater than the average cartilage thickness at the hindfoot articulations (Figure 101).

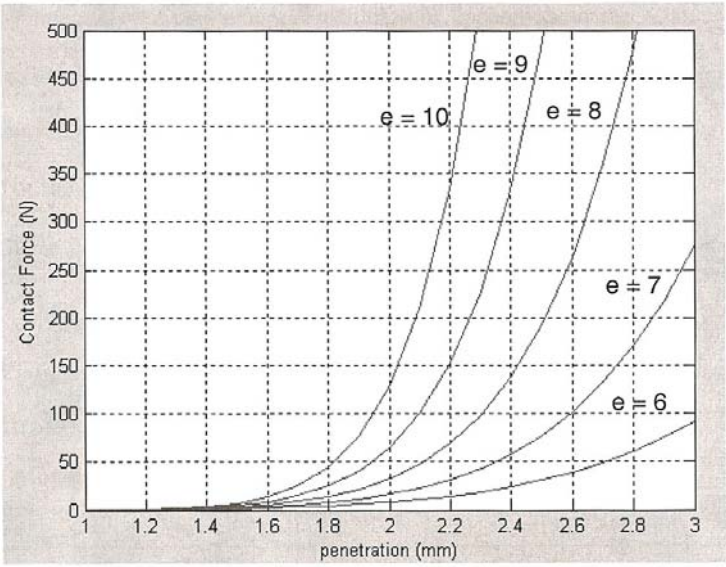

Figure 101. Contact Force as a Function of Penetration Depth

The exponent, $e = 9$, is chosen based on these data because the contact force rose asymptotically, allowing no greater than 88% compressive strain ($2.6mm$ penetration).

The damping ratio, c, increased to its maximum value as a *step* function of the penetration, x. When the penetration reaches the value of $d_{\max}$, the damping reaches its assigned value, c, The *step* function controls instantaneous changes in the damping force, avoiding numerical instability. The damping coefficient's value is chosen to be $c = 2Nmm/s$ to match previously reported data [91]. The articular surfaces are assumed to be frictionless [90].

Simulation Algorithm

The rigid body dynamic simulation software is a three dimensional rigid body dynamic analysis software package. It uses a predictor-corrector numerical algorithm to solve the dynamic equations based on the motion time history and current motion trajectory. This formulation is suitable in circumstances that involve rapid increases in force due to contact, or rapid changes in bone position in response to low applied forces due to the geometric non-linearity of the articulating bone surfaces. The dynamic analysis involves developing [53] and then integrating [54-56] the non-linear ordinary differential equations of motion [55, 92] (Equation 9) with prescribed boundary conditions (Equation 10).

$$M\ddot{q} + \phi_q^T \lambda - A^T F\left(q, \dot{q}\right) = 0 \qquad \textbf{Equation 9}$$

$$\phi\left(q, t\right) = 0 \qquad \textbf{Equation 10}$$

M is the mass matrix of the system. q is the set of coordinates representing displacements. ϕ is the set of configuration and applied motion constraints. F is the set of applied forces and gyroscopic terms of the inertia forces. A^T is the matrix that projects the applied forces in the direction of q. ϕ_q is the gradient of the constraints at any given state. The equations of motion are a second order ordinary differential equation and the boundary condition is an algebraic equation. The solution algorithm converts the equations of motion and the boundary condition to first order differential algebraic

equations and then uses previously developed integrators, including the GSTIFF, I3, and S12 formulations, to solve the system of equations [55, 56].

In order to determine contact between rigid bodies, the rigid body dynamic simulation software uses the RAPID™ Interference Detection Algorithm [57]. This algorithm computes efficient and exact interference detection between complex polygons undergoing rigid body motion [57]. This algorithm accomplishes two main tasks. First, it divides the polygons describing the geometric surfaces into sets of oriented bounding boxes [57, 93]. Second, it tests pairs for overlap using the separating axis theorem [57, 93].

Appendix B

Positioning Bones of the Finite Element Model

The rigid body dynamic model records output for the positions of three known centroidally oriented body-fixed sets of coordinates attached to the talus and calcaneus as a function of time. The three points are used to position and orient the talus and calcaneus. Text formatted computer files of the talar and calcaneal positional data are output from the rigid body dynamic simulation software. These files become input to a user-written script file to import the time-position history of three points on each the bone into internally defined arrays. This gave the user access to contact results at any position during the dynamic simulation. Of interest in this study is the description of the contact area and location at the maximum applied inversion moment. Therefore, the last time step number of the dynamic simulation is used in another user-written script to reposition and reorient the talus and calcaneus to the final time step.

The finite element model is initially in the neutral position, as is the rigid body dynamic model prior to simulation. The inertial reference frames of each bone in the dynamic model and the finite element model are positioned and oriented relative to a common global reference frame, namely that of the magnetic resonance image scanner.

A user defined local coordinate system reference frame attached to the centroid of the talus and calcaneus are defined. The x-, y-, and z-coordinates of the centroid of the talus and calcaneus are tracked over the duration of the dynamic simulation. This is one of

three points required to locate and orient a body in three dimensional space. The other two points are each defined along the x-axis, and the y-axis at an arbitrary distance of $10mm$, one point defining the x-axis of a three dimensional coordinate system, and the other defining the xy-plane of a three dimensional coordinate system.

Input File for Importing Position Data

```
rowqty=72

*dim,TalOrigin,,rowqty,3
*vread,TalOrigin(1,1),tal_pos_origin,out,,JIK,3,rowqty
(3F12.5)

*dim,TalXaxis,,rowqty,3
*vread,TalXaxis(1,1),tal_pos_xaxis,out,,JIK,3,rowqty
(3F12.5)

*dim,TalXYplane,,rowqty,3
*vread,TalXYplane(1,1),tal_pos_yaxis,out,,JIK,3,rowqty
(3F12.5)

*dim,CalOrigin,,rowqty,3
*vread,CalOrigin(1,1),cal_pos_origin,out,,JIK,3,rowqty
(3F12.5)

*dim,CalXaxis,,rowqty,3
*vread,CalXaxis(1,1),cal_pos_xaxis,out,,JIK,3,rowqty
(3F12.5)

*dim,CalXYplane,,rowqty,3
*vread,CalXYplane(1,1),cal_pos_yaxis,out,,JIK,3,rowqty
(3F12.5)
```

Input File for Positioning Bones

```
i=72

csys,13
k,70001,CalOrigin(i,1),CalOrigin(i,2),CalOrigin(i,3)
k,70002,CalXaxis(i,1),CalXaxis(i,2),CalXaxis(i,3)
k,70003,CalXYplane(i,1),CalXYplane(i,2),CalXYplane(i,3)
cskp,15,0,70001,70002,70003
csys,13
vtran,15,CAL,,,,0,1

csys,14
k,71001,TalOrigin(i,1),TalOrigin(i,2),TalOrigin(i,3)
k,71002,TalXaxis(i,1),TalXaxis(i,2),TalXaxis(i,3)
k,71003,TalXYplane(i,1),TalXYplane(i,2),TalXYplane(i,3)
cskp,16,0,71001,71002,71003
csys,14
vtran,16,TAL,,,,0,1
```

Vita

Jason Robert Toy, P.E.

Education

Ph.D. Mechanical Engineering, 2009, Drexel University, Philadelphia, PA, Advisor: Sorin Siegler, Ph.D.
M.S. Mechanical Engineering, 1999, Stevens Institute of Technology, Hoboken, NJ, cum laude
B.S. Mechanical Engineering, 1995, Trenton State College, Ewing, NJ, cum laude

Honors and Awards

Trenton State College: student scholar athlete
Stevens Institute of Technology: stress analysis design certificate

Publications

Subject Specific Models of the Hindfoot Reveal a Relationship between Morphology and Passive Mechanical Properties, Imhauser, Siegler, Udupa, and Toy, J Biomechanics, 2008, 41(6): p. 1341-9.

Research Experience

Developed a subject specific dynamic and finite element model of the hindfoot to study the relationship between morphology and passive mechanical properties.

Teaching Experience

Guest lecturer at The College of New Jersey on using ANSYS, a general purpose finite element code, to solve strength of materials and vibration problems.

Professional Qualifications

Registered Professional Engineer: NJ, PA, DE, NY, NC, VA, MD, CT, LA, FL, & D.C.
Certified Welding Inspector: American Welding Society - Society Membership: ASME, AISC, ASCE, ACI

Professional Experience

National Pipe Hanger Corporation, Mount Holly, NJ, Mechanical Engineer for a pipe hanger and support manufacturer. Responsible for performing computer aided pipe stress analyses for commercial, industrial, and power plant facilities under operating and environmental conditions. Responsible for new product design validation using finite element and experimental testing methods.

Holtec International, Marlton, NJ, Senior Engineer for an engineering firm specializing in the design of spent nuclear fuel containment structures. Performed finite element, rigid body dynamic, and strength of material analyses of spent nuclear fuel containment structures and various power plant ancillary equipment under operating and upset conditions including seismic and tornado events.

Tech-Tran Corporation, Rancocas, NJ, Design Engineering Manager for a custom magnetics manufacturer responsible for design of transformer and inductor supporting structures for various power plant, naval, transportation, and mining industries.

Paulus, Sokolowski, & Sartor, Warren, NJ, Mechanical Engineer for engineering/architectural firm specializing pharmaceutical process piping design.

Trigen, Trenton District Energy Company, Trenton, NJ, Engineering Assistant for a district heating and cooling cogeneration plant.